

Markus GLITZNER

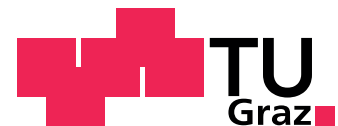
MR Methods for the Detection of New Contrast Agents Based on Fluorine Compounds

Fast CSI, analysis of image artifacts and pulse imperfections

Master's thesis

PHILIPS

Minimally Invasive Healthcare
High Tech Campus 11
5656AE Eindhoven, The Netherlands



Institute of Medical Engineering
Kronesgasse 5
8010 Graz, Austria
Head: Prof. Rudolf Stollberger, PhD

Supervisors:

Rolf Lamerichs, PhD

Prof. Rudolf Stollberger, PhD

Graz, July 2013

Statutory Declaration

I declare that I have authored this thesis independently, that I have not used other than the declared sources/resources, and that I have explicitly marked all material which has been quoted either literally or by content from the used sources.

Graz, _____

Date

Signature

Eidesstattliche Erklärung¹

Ich erkläre an Eides statt, dass ich die vorliegende Arbeit selbstständig verfasst, andere als die angegebenen Quellen/Hilfsmittel nicht benutzt, und die den benutzten Quellen wörtlich und inhaltlich entnommenen Stellen als solche kenntlich gemacht habe.

Graz, am _____

Datum

Unterschrift

¹Beschluss der Curricula-Kommission für Bachelor-, Master- und Diplomstudien vom 10.11.2008; Genehmigung des Senates am 1.12.2008

Acknowledgements

The existence of the following work is the product of the contributions of multiple persons which are hereby gratefully mentioned.

Prof. Stollberger from my home university *Graz University of Technology* paved the way to *Philips Research* and made the project possible in the first place.

At *Philips Research*, *Muhammed Yilidirim* delivered more than valuable mind models, which were crucial demystifying certain techniques of NMR in the initial time of the project. Credit is also due to *Rik Moonen*, graduate student at *Eindhoven University of Technology* for the possibility to perform joint *in-vivo* experiments.

In the highly dynamic evolution of the project, *Dr. Rolf Lamerichs* provided me with outstanding supervision and support, teaching me the relevance of the preclinical topic, taking me to symposiums and lectures and letting me spend myriads of hours at the MRI machine in order to develop ideas and sense for the methods.

Contents

1	Introduction	1
2	Theory	3
2.1	MR Physics	3
2.1.1	An NMR synopsis	3
2.1.2	The dynamic model	5
2.1.3	Macroscopic view	5
2.1.4	Perturbation of magnetization	7
2.1.5	Frames of reference	8
2.2	Elementary pulses	10
2.2.1	Description of the transverse magnetic field B_1	10
2.2.2	Theoretical pulsing experiments	11
2.2.3	Off-resonance behavior of excitation pulses	12
2.2.4	Excitation profiles	13
2.2.5	Hard-pulse approximation	18
2.3	Spin ensemble phenomena	19
2.3.1	Longitudinal relaxation	19
2.3.2	Transverse relaxation	20
2.3.3	Chemical phenomena	22
2.4	Elementary sequences	24
2.4.1	Single-pulse acquisition	24
2.4.2	Spin Echo acquisition	25
2.4.3	Higher-order echoes	28
2.4.4	Extended phase graphs	30
2.5	MRI spatial encoding	32
3	Methods	35
3.1	Magnetization propagation	35
3.1.1	Magnetization evolution	36

3.1.2	Block-pulse response	37
3.1.3	Sequential magnetization propagation	38
3.2	CSI sequences	38
3.2.1	Classical Chemical Shift Imaging	40
3.2.2	Fluorine ultrafast Turbo Spectroscopic Imaging	41
3.2.3	SSFP-CSI	44
3.3	LCSSFP-CSI	47
3.4	PFCs	48
3.5	PFCs samples	49
3.6	k -sampling patterns	49
3.7	MRI setup	50
3.7.1	Hardware	50
3.7.2	Software	50
3.8	Chemical Shift Imaging (CSI) evaluation	54
3.8.1	Signal-to-Noise ratio (SNR) quantification	54
3.8.2	Reconstruction	55
3.8.3	k -space sampling	55
3.8.4	spectral uniformity measures	56
3.8.5	Parameter dependency evaluation	56
3.9	<i>in-vivo</i> acquisition and animal preparation	56
3.10	Proprietary scripts and data	57
4	Results	58
4.1	High resolution spectroscopy on multi-resonant PFOB and PFO	58
4.2	Parameter dependency of echo sequences	59
4.3	F-uTSI	59
4.3.1	Spatial modulations in off-resonance pulsing	59
4.3.2	k -space modulations in off-resonance	60
4.3.3	k -space modulations without encoding gradients	61
4.3.4	Simulated Carr-Purcell-Meiboom-Gill (CPMG) response	62
4.3.5	Echo skipping on uni-resonant Perfluoro-Crown Ether (PFCE)	63
4.3.6	Echo skipping on multi-resonant Perfluorooctyl Bromide (PFOB)	65
4.3.7	Cartesian sampling on multi-resonant PFOB	66
4.4	Simulated SSFP response	67
4.4.1	Small-band results	67
4.4.2	Broadband response	67

4.5	LCSSFP-CSI	69
4.5.1	Simulated responses for phase-incremented pulses	69
4.5.2	Linearly combined simulations responses	70
4.5.3	k -space response on multi-resonant PFOB	71
4.5.4	spectral response on multi-resonant PFOB	72
4.5.5	Linear combination of SSFP responses	73
4.6	Benchmarking F-uTSI and LCSSFP	74
4.6.1	Detectability of a PFOB dilution series	74
4.6.2	Signal-to-Noise ratio over time (SNR_t)	75
4.6.3	Spectral uniformity	76
4.6.4	Broadband response	76
4.7	<i>in-vivo</i> experiments	78
4.7.1	Individual SSFP responses	78
4.7.2	LCSSFP and F-uTSI responses	79
5	Discussion	81
	Bibliography	85

MR Methods for the Detection of New Contrast Agents Based on Fluorine Compounds

The Master's thesis aim was to analyze, improve and implement current and novel sequences for fast spectroscopic imaging on ^{19}F agents. These agents exhibit large chemical shift dispersions. In this regime, using clinically relevant powers, assumptions about RF-pulsing loose validity. An analytical framework is derived and used to describe arising problems and artifact formation in an existing fast multi-echo sequence. Furthermore, more stable steady-state pulse sequences using multiple pulse phase-increments were characterized and implemented. Measurements were carried out using a $3T$ clinical setup on both phantoms and *in-vivo* to validate theoretical predictions. The multi spin-echo approach was shown to have problematic spectral and spatial features, while the implemented steady-state approach shows solid performance.

key words: fast spectroscopic imaging, multi-echo, off-resonance pulsing, steady-state pulsing, Bloch simulations

MR-Methoden zur Detektion Neuartiger Fluorbasierender Kontrastmittel

Folgende Masterarbeit handelt von der Analyse, Verbesserung und Entwicklung bestehender und neuartiger MR-Pulssequenzen zur schnellen spektroskopischen Bildgebung von ^{19}F -Kontrastmitteln. Aufgrund der breiten chemischen Verschiebung dieser Mittel kommt es zur Aushebelung fundamentaler Annahmen bezüglich RF-Pulsen, insbesondere bei der Verwendung klinisch relevanter Leistungen. Ein analytisches Gerüst zur Berechnung der realen Wirkung solcher leistungslimitierter Pulse wurde erarbeitet, um Komplikationen und Artefaktentstehung in einer bestehenden Spinecho-Sequenz zu beschreiben. Weiters wurden stabilere Steady-State-Sequenzen hinsichtlich spektraler Eigenschaften charakterisiert und implementiert. Anschließend wurden Messungen auf einem klinischen $3T$ -System durchgeführt, um theoretische Erkenntnisse sowohl im Phantom, als auch *in-vivo* zu bestätigen. Die Multispinecho-Strategie zeigte dabei problematische Eigenschaften, sowohl örtlicher als auch spektraler Natur, wohingegen sich die Steady-State-Sequenz als äußerst stabil herausstellte.

Stichwörter: schnelle spektroskopische Bildgebung, multi-echo, off-resonance Anregung, Steady-State Pulssequenz, Bloch-Simulationen

Acronyms

AM Amplitude Modulation	PET Positron Emission Tomography
ADC Analog-to-Digital Converter	PFC Perfluorocarbon
CPMG Carr-Purcell-Meiboom-Gill	PFCE Perfluoro-Crown Ether
CSI Chemical Shift Imaging	PFO Perfluorooctane
DAS Data Acquisition System	PFOB Perfluorooctyl Bromide
DFT Discrete Fourier Transformation	PM Phase Modulation
ES Echo Spacing	ppm Parts Per Million
F-uTSI Fluorine ultrafast Turbo Spectroscopic Imaging	PSF Point Spread Function
FID Free Induction Decay	RF Radio Frequency
FM Frequency Modulation	SE Spin Echo
FOV Field of View	SAR Specific Absorption Rate
FWHM Full Width at Half-Maximum	SLR Shinnar-LeRoux
HF High-frequency	SNR Signal-to-Noise ratio
LCSSFP Linear Combination Steady State Free Precession	SNR_t Signal-to-Noise ratio over time
ME Multi Echo	SPECT Single Photon Emission Computed Tomography
MR Magnetic Resonance	STEAM Stimulated Echo Acquisition Mode
MRI Magnetic Resonance Imaging	SSFP Steady State Free Precession
MRS Magnetic Resonance Spectroscopy	SVS Single Voxel Spectroscopy
MRSI Magnetic Resonance Spectroscopic Imaging	TMS Tetramethylsilane
NMR Nuclear Magnetic Resonance	TSI Turbo Spectroscopic Imaging
NSA Number of Signals Averaged	TSE Turbo Spin Echo

1 Introduction

Molecular imaging has been experiencing rising interest. The ability to spatially resolve physiologic and pathologic processes opens new paths for both diagnostics and therapeutics.

Established techniques allow to selectively mark targeted sites, e.g. using immunoselective mechanisms to mark cancerous tissue. These marking substances are usually referred to as targeted contrast agents equipped with a payload inducing an additional feature for a certain imaging method. As an example, *fluorescence imaging* uses the intrinsic optical properties, i.e. luminescence, of a material for obtaining a spatially resolved signal. These signals are a representation of the functional or physiologic distribution of the targeted agent. Additionally, Magnetic Resonance Imaging (MRI), Single Photon Emission Computed Tomography (SPECT) and Positron Emission Tomography (PET) are amongst these imaging modalities. In classic clinical MRI the contrast mechanisms are described by properties of proton distributions in a body and their inherent relaxation properties. Markers for common MRI are available: their working principle is based on additional contrast induction, e.g. by high payload *gadolinium* agents that induce local variations in relaxation.

The high natural abundance of water-bound protons cause their dominant signal in imaging *in-vivo*. Clinical value can also be extracted from other proton-containing substances, using the property of shifted frequency responses depending on the chemical environment of the protons. This technique, Magnetic Resonance Spectroscopy (MRS) is established for determination and examination of cancerous tissue via metabolites or fat quantification in the liver. For example, the quantification of acetylcholine is a significant indicator in prostate cancer or brain tumors.

Having very similar properties compared to protons, the fluorine isotope ^{19}F has been identified for clinical MRI. Its *spin-1/2* property along with a large *gyromagnetic ratio* γ , slightly less than that of ^1H , makes ^{19}F -MRI a feasible alternative. Compared to proton (^1H) MRI, however, straightforward ^{19}F MRI is hampered by particular features

of the ^{19}F molecules. In most ^{19}F -compounds, the bandwidth of the spectral ^{19}F -Nuclear Magnetic Resonance (NMR) response is generally very broad and diverse.

However, these spectral properties provide a unique *spectral signature* for distinct ^{19}F compounds. This allows *multicolor imaging*, each color representing the integrated spectral response of a distinct ^{19}F -specimen in Magnetic Resonance Spectroscopic Imaging (MRSI). Moreover, the ^{19}F signal is unique and therefore, pre-contrast acquisitions are not required, facilitating the logistics of such examinations, as compared to T_1 or T_2 based agents. Furthermore, this ensures an intrinsically high specificity of the ^{19}F agents. However, another implication to the large spectral width of ^{19}F -compounds, especially in high-field MRI systems, is that the excitation bandwidths of the applied RF pulses are often significantly less than the bandwidth of the spectral response.

This work points out phenomena arising with the application of a fluorine MRSI sequence, namely *Fluorine ultrafast Turbo Spectroscopic Imaging (F-uTSI)*. Previous experiments employing F-uTSI revealed a strong parameter dependency of the sequence and subsequent artifacts. Furthermore, the signal amplitude exhibits a strong spectral variation using Perfluorocarbons (PFCs) with multiple resonances. These effects are mentioned hereinafter.

The influence of imperfect broadband pulsing is treated by means of an analytic framework dealing with imperfect pulsing scenarios and the arising effect on the spectral imaging. The impact of such pulses are shown using special solutions of the *Bloch* equations, simulating the spectral response of repeated pulse application using magnetization propagation matrices. Simulations and acquired data are correlated with each other in order to obtain insight into the evolution of magnetization in a highly chemical shift dispersive regime towards steady states. Results were obtained for both F-uTSI and an alternative Steady State Free Precession (SSFP) approach, utilizing phase incremented pulses in order to stabilize the spectral response. Both F-uTSI and the SSFP sequence were analyzed in terms of imaging artifacts and spectral properties in the Chemical Shift Imaging (CSI) images.

2 Theory

2.1 MR Physics

In the current section, a short overview of Magnetic Resonance (MR) physics is given. The physical interaction behind MRI and its descriptions are extensive. The interested reader is referred to [1] for a complete description of the underlying NMR physics and to [2] on how to exploit NMR for imaging purposes.

In this chapter the principle of the MR signal will be described and translated to the macroscopic descriptor of the magnetization by the *Bloch* equations.

2.1.1 An NMR synopsis

The understanding of the physical principle of MRI started to evolve in the the early 1920s by means of the results of the famous *Stern-Gerlach* experiment stating the existence of an intrinsic property, i.e. the spin, of a particle. Later on *Bloch* and *Purcell* published on the behavior of the resonance behavior of particles exhibiting certain spin properties. They were rewarded the nobel prize for the discovery of NMR. [2]

For each particle, a set of quantum numbers is defined, characterizing its behavior in a magnetic field. Phenomenologically, a nucleus has a magnetic moment described by

$$\vec{\mu} = \gamma \vec{J}, \tag{2.1}$$

relating it to its angular momentum \vec{J} with γ defining the *gyromagnetic ratio*. The *gyromagnetic ratio* is characteristic for a distinct particle (e.g. a proton, an electron or a nucleus) and found by experiment.

Nucleus	γ	rel. sensitivity	natural abundance	abundance in human
	MHz/T	% of 1H	%	M
1H	42.58	100	99.98	88
^{13}C	10.07	1.59	1.11	$\cdot 2$
^{19}F	40.05	83	100	$4 \cdot 10^{-6}$
^{31}P	17.25	6.65	100	$75 \cdot 10^{-3}$

Table 2.1: List of physiologically abundant *spin-1/2*-nuclei, adapted from [2].

The essence of the formulation is that a rotating (or *spinning*) particle exhibits, by quantum mechanical description, a property inducing interaction with a magnetic field. The interaction is described by the magnetic quantum numbers m_j , defining the *magnitude* of the angular momentum and its possible *states* in an experiment as

$$J = m_j \hbar \quad (2.2)$$

For protons, along with several other nuclei such (see Table 2.1), quantum number j is determined as being $j = \frac{1}{2}$, leading to the magnetic quantum numbers of $m_j = \pm \frac{1}{2}$ according to

$$m_j = -j, -j + 1, \dots, j - 1, j \quad (2.3)$$

Thus their denotation as *spin-1/2 particles*.

The last paragraph implies that along with the two *modes* or *states* of spinning (i.e. $+1/2$ and $-1/2$, or *spin-up* and *spin-down*), Equation (2.1) yields two solutions for the arising magnetic moment. Particles with a *magnetic moment* $\vec{\mu}$ exposed to a magnetic flux \vec{B} (with B_z being its only component) have the energy

$$E = -\vec{\mu} \cdot \vec{B} = -\gamma m_j \hbar B_z. \quad (2.4)$$

With this statement about the energy and quantization of m_j , it is clear, that the difference in energy of the two possible spin states is given by

$$\Delta E = \hbar \gamma B_z = \hbar \omega_0 \quad (2.5)$$

Intuitively, exciting a particle with its energy difference (e.g. by means of an Radio Frequency (RF)-induced energy) will cause the particle to flip its energy level between the spin states. However, regarding an ensemble of magnetic moments, thermal equilibrium will (statistically) force parts of the magnetic moments to return back to the energetically lower state, causing an emission of the difference energy, i.e. the characteristic *resonance* frequency. These processes are covered by *Boltzmann* statistics. The energy exchange with an RF irradiation of exactly ω_0 is called *resonance*. Thus Nuclear Magnetic Resonance (NMR).

2.1.2 The dynamic model

The crucial idea in describing the behavior of magnetic moments introduced in Section 2.1.1 is the interaction of magnetic moments with a magnetic field \vec{B} and the consequent separation in energy levels.

Having the description of the magnetic moment of a particle, it is possible to formulate the general, dynamic behavior of the moment. This is commonly known as the gyroscope equivalent of NMR and reads as follows

$$\frac{d\vec{\mu}}{dt} = \gamma\vec{\mu} \times \vec{B} \quad (2.6)$$

As visible, the previously defined gyromagnetic ratio γ , used to relate magnetic and dynamic quantities in Equation (2.1), appears again yielding a formulation between the interaction of the inherent spin-property with an externally applied magnetic field \vec{B} (Equation (2.6)) Using this description and prior knowledge about the properties of the investigated particles (i.e. γ), it is possible to predict the behavior of a particle to an applied magnetic field of *any* strength and frequency.

2.1.3 Macroscopic view

Macroscopically, the NMR experiment measures the magnetization \vec{M} comprised of various magnetic moments, each of which is itself described by Equation (2.6). Assuming a

static magnetic field B_0 along the z -direction of a (cartesian) coordinate system, forces the single magnetic moments to precess around the z -axis with an angular speed of

$$\omega_0 = \gamma B_0 \quad (2.7)$$

following Equation (2.6). This is one of the principal relations in NMR and can be shown by assuming any arbitrary magnetic moment $\vec{\mu} = (\mu_x, \mu_y, \mu_z)^T$ and the static magnetic field B_0 along z , i.e. $\vec{B} = (0, 0, B_0)^T$. Consequently, Equation (2.6) states solely variations $d\mu$ along the directions perpendicular to z . Solving the system of differential equations yields

$$\begin{Bmatrix} \mu_x \\ \mu_y \\ \mu_z \end{Bmatrix} = \begin{Bmatrix} \mu_x(0)\cos(\gamma B_0 t) + \mu_y(0)\sin(\gamma B_0 t) \\ \mu_y(0)\cos(\gamma B_0 t) - \mu_x(0)\sin(\gamma B_0 t) \\ \mu_z(0) \end{Bmatrix} \quad (2.8)$$

It is apparent, that this special solution of Equation (2.6) yields a clockwise rotation of the magnetic moments with the angular velocity given in Equation (2.7). Additionally, from an intuitive perspective it can be concluded, that applying a magnetic field on a magnetic moment as in Equation (2.6) only changes its transverse components, the components parallel to the field remain static. The magnetic moment *precesses* about the axis of the applied field.

Macroscopically, assuming equilibrium, the components of the magnetic moments which are transverse to the z -axis are uncorrelated, the non- z components cancel out because of the different phases of μ . The *excess magnetization* is M_0 aligning along z with its quantity determined by *Boltzmann* statistics. Equation (2.6) is still valid, however a new macroscopic perspective is introduced. The new, *magnetization-based* formulation reads

$$\frac{d\vec{M}}{dt} = \gamma \vec{M} \times \vec{B} \quad (2.9)$$

and is called the *Bloch equations*.

Despite applied NMR techniques tend to be quite extensive, the relationship provided in Equation (2.9) describes the behavior of any net magnetization in NMR, however, still ignoring higher effects such as *relaxation* and *spin coupling*.

2.1.4 Perturbation of magnetization

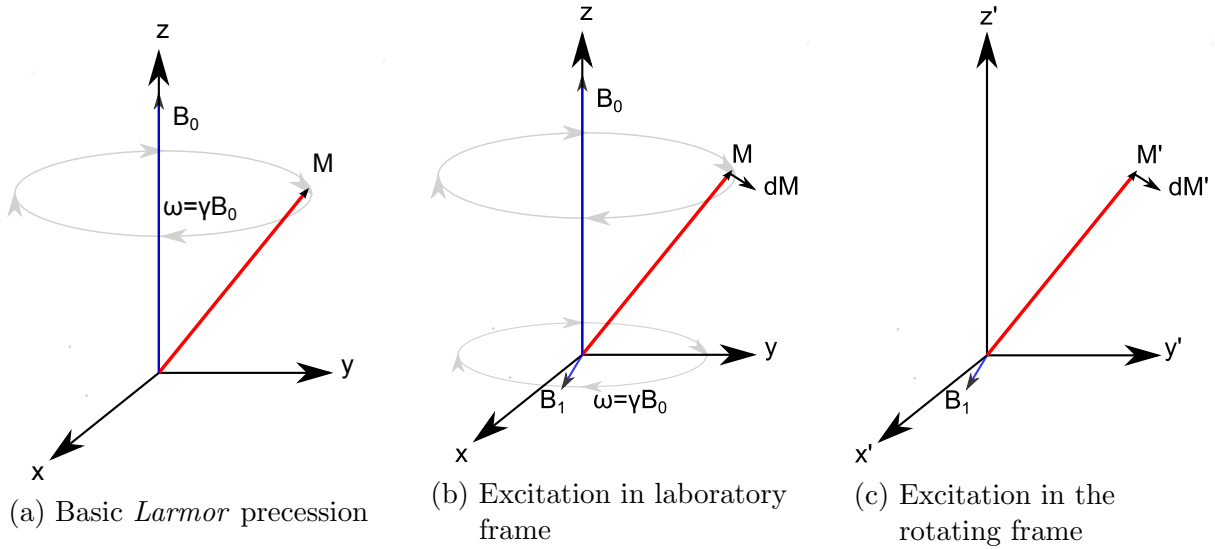


Figure 2.1: Elementary modes of precessions of magnetization around applied magnetic fields according to *Bloch's* equations

In Section 2.1.3 it was stated that any applied magnetic field forces the magnetic moments to change their components in a rotational manner, i.e. the magnetization \vec{M} rotates around any applied magnetic field \vec{B} . Macroscopically regarding the ensemble of magnetic moments, i.e. equilibrium magnetization aligned along the z -direction (M_0), earlier property is used to rotate the magnetization in a transverse direction by applying a transverse field component B_1 .

Imagining another *constant, transverse* field component to the situation (shown in Figure 2.1a) would just cause the magnetization to precess about this new summed magnetic field. However, following the trajectory of the magnetization (respectively the magnetic moment as its mathematical equivalent) in Figure 2.1b shows, that applying a magnetic field which precesses in the *same manner* as the magnetization, is able to rotate the components of the magnetization transverse (x, y) to its static field direction. The latter is a special case of the *Bloch* equations (Equation (2.9)) and describes the *most efficient* way of changing the direction of magnetization \vec{M} by applying a field which is persistently perpendicular to the selected direction of change as depicted in Figure 2.1b.

Generally, perturbations of magnetization in NMR are yielded using RF pulses, oscillating, as depicted before, with the *Larmor* frequency ω_0 of the examined specimen. The content of information through this kind of perturbation experiment is essential for either MRI, MRS and MRSI.

2.1.5 Frames of reference

In the previous section the different views of regarding the aligned magnetization and its reaction to a varying RF field was introduced. Regarding Figures 2.1a and 2.1b it might seem a hard task to intuitively determine the variation of \vec{M} caused by an arbitrarily applied RF field \vec{B}_1 . Due to *Larmor* precession, the magnetization vector is under steady motion, accompanied by the consensual rotation direction of the RF field influencing the components of the magnetization according to Equation (2.9), shown in Figure 2.1b. Regarding γ being in a *MHz*-range, the environment (or coordinate system) covering these *highly dynamic* processes are described in the *laboratory frame of precession*.

However, a more convenient perspective simplifying the ongoing processes is desirable. Regarding the prerequisites for an optimal excitation, i.e. precession of \vec{M} and \vec{B}_1 in the same manner (described in Section 2.1.4), leads to an apparent simplification: the rotation of the coordinate system *itself* with the precession frequency ω_0 , illustrated in Figure 2.1c: Basically, the *Bloch* equations are transformed in a *rotating frame of reference* by rotating the *laboratory frame of resonance* clockwise around the *z*-axis, i.e. in the same direction of both magnetization and RF field. The transformation operation

$$\left(\frac{d\vec{M}}{dt} \right)_{rot} = \left(\frac{d\vec{M}}{dt} \right)_{lab} - \vec{\Omega} \times \vec{M} \quad (2.10)$$

where Ω is the *vector of rotation* defined as

$$\Omega = \begin{Bmatrix} 0 \\ 0 \\ -\omega_{rot} \end{Bmatrix} \quad (2.11)$$

for a clockwise rotation in a right-hand-side sense around the negative *z*-axis with ω_{rot} . Thus and with Equation (2.10), the demodulated, rotating magnetization states

$$\frac{d\vec{M}'}{dt} = \gamma \vec{M}' \times \vec{B} + \vec{M}' \times \Omega \quad (2.12)$$

In case of the only magnetic field component acting along *z*, i.e. M_z , the variation of the transformed magnetization \vec{M}' is

$$\frac{d\vec{M}'}{dt} = \vec{M}' \times (\gamma\vec{B} + \Omega) = \vec{M}' \times \begin{Bmatrix} 0 \\ 0 \\ \gamma B_0 - \omega_{rot} \end{Bmatrix} \quad (2.13)$$

The simplicity coming along with Equation (2.13) is seen the easiest when the rotation of the coordinate system around z is performed with the *Larmor* frequency of the regarded magnetization, i.e. $\omega_{rot} = \omega_0 = \gamma B_0$. In this case, not a single variation of any component of \vec{M}' takes place - the magnetization vector \vec{M}' remains steady in the *rotating frame*. For this reason and when analyzing specimen with a certain *gyromagnetic ratio* γ exposed to a magnetic field B_0 , the angular speed of the rotating frame is set accordingly.

However, in MRS, magnetization does not necessarily precess at a single rotation frequency. Consequently a difference between the rotation frequency ω_{rot} and γB_0 arises, i.e.

$$\Delta\omega = \gamma B_0 - \omega_{rot} \quad (2.14)$$

In MRS, $\Delta\omega$ is usually referred to as *chemical shift* caused by nuclei precessing at different frequencies with respect to a certain frequency reference, the *center frequency*. Therefore, a solution arises for the rate of change in these *off-resonance* regimes described by

$$\frac{d\vec{M}'}{dt} = \vec{M}' \times (\gamma\vec{B} + \Omega) = \vec{M}' \times \begin{Bmatrix} 0 \\ 0 \\ \Delta\omega \end{Bmatrix} \quad (2.15)$$

The problem in Equation (2.15) has already been addressed in Equation (2.8) and has a similar solution

$$\begin{Bmatrix} M_x \\ M_y \\ M_z \end{Bmatrix} = \begin{Bmatrix} M_x(0)\cos(\Delta\omega t) + M_y(0)\sin(\Delta\omega t) \\ M_y(0)\cos(\Delta\omega t) - M_x(0)\sin(\Delta\omega t) \\ M_z(0) \end{Bmatrix} \quad (2.16)$$

yielding a clockwise precession with $\Delta\omega$. This time, however, with reference to the introduced rotation frequency of the rotating frame.

2.2 Elementary pulses in NMR

2.2.1 Description of the transverse magnetic field B_1

As described before, NMR techniques use transverse magnetic fields in order to force a magnetization from an equilibrium position along z (M_z) into the transverse plane (x, y). Additionally, the fundamental idea of adding change of rate towards the transverse plane was given in Section 2.1.3, stating that a magnetic field is most effective when rotating in the same manner around z as the magnetization itself.

Mathematically, this rotating field is described as

$$\vec{B}_1 = \begin{Bmatrix} B_{1,x} \\ B_{1,y} \end{Bmatrix} = \begin{Bmatrix} B_1 \cos(\omega_{RF}t + \phi_{RF}) \\ -B_1 \sin(\omega_{RF}t + \phi_{RF}) \end{Bmatrix} \quad (2.17)$$

with ϕ_{RF} being the phase of the B_1 vector with respect to the x -axis of the rotating frame. The B_1 field described by an oscillating vector is (as the magnetization in Section 2.1.5) best described in a rotating frame of reference. Accordingly, the vector B_1 is translated in a rotating frame, rotating with ω_{rot} , i.e.

$$\begin{aligned} \vec{B}_{1,rot} &= \begin{bmatrix} \cos(\omega_{rot}t) & -\sin(\omega_{rot}t) \\ \sin(\omega_{rot}t) & \cos(\omega_{rot}t) \end{bmatrix} \begin{Bmatrix} B_{1,x} \\ B_{1,y} \end{Bmatrix} \\ &= \begin{Bmatrix} B_1 \cos((\omega_{RF} - \omega_{rot})t + \phi_{RF}) \\ -B_1 \sin((\omega_{RF} - \omega_{rot})t + \phi_{RF}) \end{Bmatrix} \end{aligned} \quad (2.18)$$

Combining both the previously introduced rotated coordinate system and the accordingly transformed *circularly polarized* transverse field \vec{B}_1 results in a total description of *any* rotational processes translated to the *rotating frame of reference*

$$\begin{aligned} \frac{d\vec{M}'}{dt} &= \vec{M}' \times (\gamma \vec{B} + \Omega) \\ &= \vec{M}' \times \left(\gamma \begin{Bmatrix} B_1 \cos((\omega_{RF} - \omega_{rot})t + \phi_{RF}) \\ -B_1 \sin((\omega_{RF} - \omega_{rot})t + \phi_{RF}) \\ B_0 \end{Bmatrix} + \begin{Bmatrix} 0 \\ 0 \\ -\omega_{rot} \end{Bmatrix} \right) \end{aligned} \quad (2.19)$$

For convenience, in the course of this thesis, the angular speed of the rotating frame ω_{rot} and the frequency of the applied RF irradiation is arbitrarily set to be equal.

$$\begin{aligned}
\frac{d\vec{M}'}{dt} &= \vec{M}' \times (\gamma\vec{B} + \Omega) \\
&= \gamma\vec{M}' \times \begin{pmatrix} B_1 \cos(\phi_{RF}) \\ -B_1 \sin(\phi_{RF}) \\ B_0 - \frac{\omega_{rot}}{\gamma} \end{pmatrix} \\
&= \gamma\vec{M}' \times \vec{B}_{eff}
\end{aligned} \tag{2.20}$$

The system of differential equations (with constant coefficients) in Equation (2.20) can generally be used for finding solutions to pulse experiments. Most interestingly, when going *off-resonance*, the z component in the *effective magnetic field* \vec{B}_{eff} is increased. The effect of off-resonance excitation on the magnetization will be depicted in the next section.

2.2.2 Theoretical pulsing experiments

The easiest pulsing experiment is shown by taking Equation (2.20) for an *on-resonance* case, i.e.

$$\vec{B}_{eff} = \begin{pmatrix} B_1 \cos(\phi_{RF}) \\ -B_1 \sin(\phi_{RF}) \\ B_0 - \frac{\omega_{rot}}{\gamma} \end{pmatrix} \stackrel{\phi_{RF}=0}{=} \begin{pmatrix} B_1 \\ 0 \\ 0 \end{pmatrix} \tag{2.21}$$

The condition $\phi_{RF} = 0$ is set arbitrarily, stating that in the first moment of observation, the RF field \vec{B}_1 acts along the x axis. This problem results in a solution with already known structure, i.e.

$$\begin{pmatrix} M'_x(t) \\ M'_y(t) \\ M'_z(t) \end{pmatrix} = \begin{pmatrix} M'_{x,0} \\ M'_{y,0} \cos(\gamma B_1 t) + M'_{z,0} \sin(\gamma B_1 t) \\ M'_{z,0} \cos(\gamma B_1 t) - M'_{y,0} \sin(\gamma B_1 t) \end{pmatrix} \tag{2.22}$$

Equation (2.22) reads as follows: Assuming a magnetization being in perfect equilibrium along z , the magnetization vector $\vec{M} = (0, 0, M'_{z,0})^T$, a change in the magnetization components *perpendicular* to the applied transverse RF field is induced. The change in the components is most commonly described by an angle, the *flip angle* α , relating the angle between the magnetization magnitude in longitudinal z direction related to the magnitude in transverse plane

$$|M'_T(t)| = \sqrt{M'_x(t)^2 + M'_y(t)^2} \quad (2.23)$$

Taking the mentioned initial magnetization along z , derivation of the *on-resonance* flip angle α yields

$$\alpha(t) = \gamma \int_0^t B_1(t') dt' \quad (2.24)$$

While this case is the by far simplest, it states an important message, according to the *Bloch* equations in Equation (2.20), a change of magnetization happens solely in directions *perpendicular* to the applied RF field. While this is not of great importance here, it becomes critical in special pulsing cases, e.g. when pulsing *off-resonance*, which will be discussed in the next sections.

2.2.3 Off-resonance behavior of excitation pulses

In ^{19}F NMR, the pulsing gets severely influenced by the large chemical shift dispersion, and additionally, in clinical application, the limited B_1 further limits the validity for *hard pulsing*. Thus, the implications of *off-resonance* pulsing are to be considered in more detail and illustration.

Introducing a difference in frequencies of the resonance under observation (i.e., a resonance of a specific species) and the oscillation of the transverse field causes a new *effective* field B_{eff} which is no longer in the transverse plane (as for on-resonance irradiation) but flipped away from the z axis by an angle θ , respectively $\frac{\pi}{2} - \theta$ away from the transverse plane.

A new axis of rotation is thus introduced, the deviation angle θ being a function of the offset frequency and the *on-resonance* flip frequency as

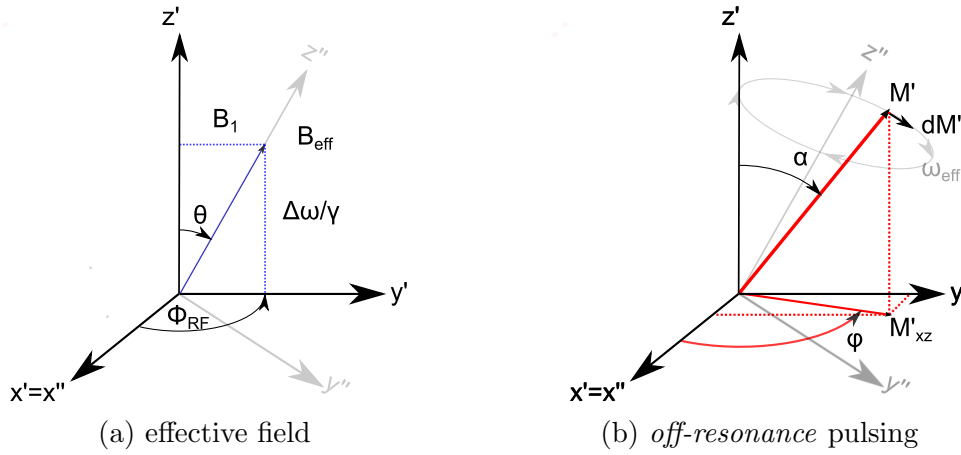


Figure 2.2: Off-resonance situation in the rotating frame. Pulses are applied on along the positive y' axis

$$\tan(\theta) = \frac{\gamma B_1}{\Delta\omega} \quad (2.25)$$

Assuming a pulse angle of $\phi_{RF} = 90^\circ$, the new situation including the effective field B_{eff} is depicted in Figure 2.2a. The effect of the new perturbation can be explained by a new *longitudinal* field-component $\Delta\omega/\gamma$ in addition to the irradiated *transverse* field, yielding the new, inclined rotation axis B_{eff} . Moreover, the speed with which the magnetization *orthogonal* to B_{eff} rotate is, again, proportional to the field's magnitude

$$\omega_{eff} = \gamma \left| \vec{B}_{eff} \right| = \gamma \sqrt{B_1^2 + (\Delta\omega/\gamma)^2} \quad (2.26)$$

With the new axis of rotation defined in Equation (2.25) and the effective angular speed around this axis in Equation (2.26) it is possible to calculate the effect of a pulse of frequency ω_{rot} and duration τ_p for *off-resonant* spectral responses.

2.2.4 Excitation profiles

The insight of pulse behavior in Section 2.2.3 can be used to determine the effect of an RF pulse of certain frequency on a spin ensemble in equilibrium. This scenario is crucial to all NMR measurements since all of them are based on the measurement of the (oscillating) magnetization in the transverse plane relative to the B_0 -(z -)directed reference orientation.

Given again the situation depicted in Figure 2.2, it is apparent that the *off-resonance* magnetizations experience the effective field's direction and are thus perturbed differently. From Equation (2.24), the *on-resonance* flip angle can be derived, assuming a constant amplitude of the transverse magnetic field, with the *pulse duration* τ_p

$$\alpha(\Delta\omega = 0) = \alpha_0 = \gamma B_1 \tau_p \quad (2.27)$$

This very general pulsing mode is called *block pulse*. However, regarding the new rotation axis in Figure 2.2 along the *effective field* and the accompanying rotation $\alpha'(\Delta\omega)$ of the magnetization experiencing B_1 during the same *pulse duration* yields (cf. Equation (2.26))

$$\begin{aligned} \alpha'(\Delta\omega) &= \gamma \left| B_{eff}^- \right| \tau_p = \gamma \sqrt{B_1^2 + (\Delta\omega/\gamma)^2} \tau_p = \gamma B_1 \tau_p \sqrt{1 + \left(\frac{\Delta\omega}{\gamma B_1} \right)^2} \\ &= \alpha_0 \sqrt{1 + \left(\frac{\Delta\omega}{\gamma B_1} \right)^2} \end{aligned} \quad (2.28)$$

in the new coordinate system along B_{eff} . By using rotation matrices (with axis indicated in the index) around the principal axes, the effect of the magnetic field on an arbitrary magnetization can be calculated for the rotating frame coordinate system as follows:

1. Projection of the initial magnetization $\mathbf{M}(0)$ in the new (double-dashed in Figure 2.2) coordinate system by the rotation operators

$$\mathbf{M}(0)' = \mathbf{R}_z(+\phi_{RF}) \mathbf{R}_x(+\theta) \mathbf{M}(0) \quad (2.29)$$

2. Rotation in the new coordinate system around z'' (clockwise) according to Equation (2.28)

$$\mathbf{M}(\tau_p)' = \mathbf{R}_{z''}(-\omega_{eff}\tau_p) \mathbf{M}(0)' \quad (2.30)$$

3. Backprojection in the rotating frame using the same rotation operators but inversely applied finally yields

$$\begin{aligned} \mathbf{R}_{tot}(\tau_p, \Delta\omega, B_1, \phi_{RF}) &= \mathbf{R}_{x'}(-\theta) \mathbf{R}_{z'}(-\phi_{RF}) \mathbf{R}_{z''}(-\omega_{eff}\tau_p) \\ &\quad \cdot \mathbf{R}_{z'}(\phi_{RF}) \mathbf{R}_{x'}(\theta) \end{aligned} \quad (2.31)$$

for the overall *four-parameter* operator.

While, basically, pulse situations can now be analytically determined regardless of the initial magnetization, for the *excitation case* solely equilibrium magnetization M_0 along the z -axis is considered, thus

$$\mathbf{M}(\tau_p, \Delta\omega, B_1, \phi_{RF}) = \mathbf{R}_{tot} \begin{Bmatrix} 0 \\ 0 \\ M_0 \end{Bmatrix} \quad (2.32)$$

Multiplying Equation (2.32) yields, despite the amount of rotation operators in Equation (2.31), a compact solution. For the case $\phi_{RF} = 0$, assuming RF-pulsing along the x -axis, the solutions for effective flip angle α and transverse phase φ become

$$\begin{aligned} \cos(\alpha) &= 1 - 2 \sin^2 \left(\frac{\tau_p \omega_{eff}}{2} \right) \sin(\theta) \\ \tan(\varphi) &= \frac{\cos(\theta) (1 - \cos(\tau_p \omega_{eff}))}{\sin(\tau_p \omega_{eff})} \end{aligned} \quad (2.33)$$

and with Equations (2.25), (2.27) and (2.28)

$$\begin{aligned} \cos(\alpha) &= 1 - 2 \frac{\sin^2 \left(\frac{\alpha_0}{2} \sqrt{1 + \left(\frac{\Delta\omega}{\gamma B_1} \right)^2} \right)}{1 + \left(\frac{\Delta\omega}{\gamma B_1} \right)^2} \\ \tan(\varphi) &= -\tan \left(\frac{\alpha_0}{2} \sqrt{1 + \left(\frac{\Delta\omega}{\gamma B_1} \right)^2} \right) \cos \left(\arctan \left(\frac{\gamma B_1}{\Delta\omega} \right) \right) \end{aligned} \quad (2.34)$$

The notation collecting the terms $\frac{\gamma B_1}{\Delta\omega}$ and α_0 is convenient (similarly in [3]), summing up the following:

Every *block-type*³ RF irradiation has a frequency ω_{RF} , duration τ_p , amplitude B_1 and phase ϕ_{RF} . The pulse excites a *single-resonant* species with characteristic frequency γB_0 ,

³there are more sophisticated, Amplitude Modulation (AM), Frequency Modulation (FM) and Phase Modulation (PM) RF-pulses which are not treated here

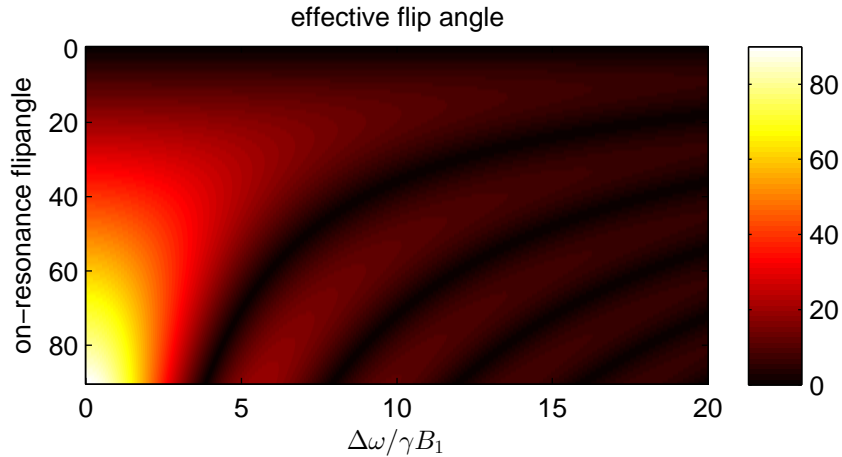


Figure 2.3: *Off-resonance* excitation profile depending on the spectral location of the resonance with reference to the RF pulse

ideally matching ω_{RF} . However, there are scenarios of the pulse being mismatched to a single resonance, the single resonance is broadened on purpose in order to yield spatial selectivity (such as in slice-selective MRI using gradients [4]) *or* the species simply exhibits multiple resonances (seen later in Section 2.3.3) so that a general match is not achievable any more. Figures 2.3 and 2.4 show the implication of going *off-resonance*.

Figure 2.3 depicts the excitation profile of block-pulses with an intended *on-resonance* flip angle in the range $\alpha_0 \in [0^\circ; 90^\circ]$. It is very apparent, that at large (excitation) flip angles, e.g. $\alpha_0 = 90^\circ$, the broadband behavior is strongly variable. While the effective flip angle in the vicinity of the RF-frequency is the intended one, the effective off-resonance flip angle varies greatly. For a scenario $\Delta\omega/\gamma B_1 \leq 20$, 4 comparatively compact side-maxima build up. However, with decreasing on-resonance flip angles the effective excitation start spread over the regarded range - values $\alpha_0 \leq 10$ do not express side lobes any more.

Figure 2.4 presents the *off-resonance* behavior of selected flip angles α_0 , i.e. slices from Figure 2.3: The profiles show again the strong influence of the relative *off-resonance* frequency $\Delta\omega/\gamma B_1$. It becomes apparent that, generally, using stronger transverse field amplitudes B_1 , *block-pulses* can be used to shift the offset-frequency domain towards the main lobe. According to Equation (2.27), this leads to a decrease in pulse time. Intuitively using an infinitely large field B_1 , applied in a *Dirac-distribution*-manner yields optimal flip-angles α' for all off-resonance contributions. This can also be shown by taking the limit in Equation (2.34)

$$\cos(\alpha') = \lim_{B_1 \rightarrow \infty} \cos(\alpha) = \cos(\alpha_0) \quad (2.35)$$

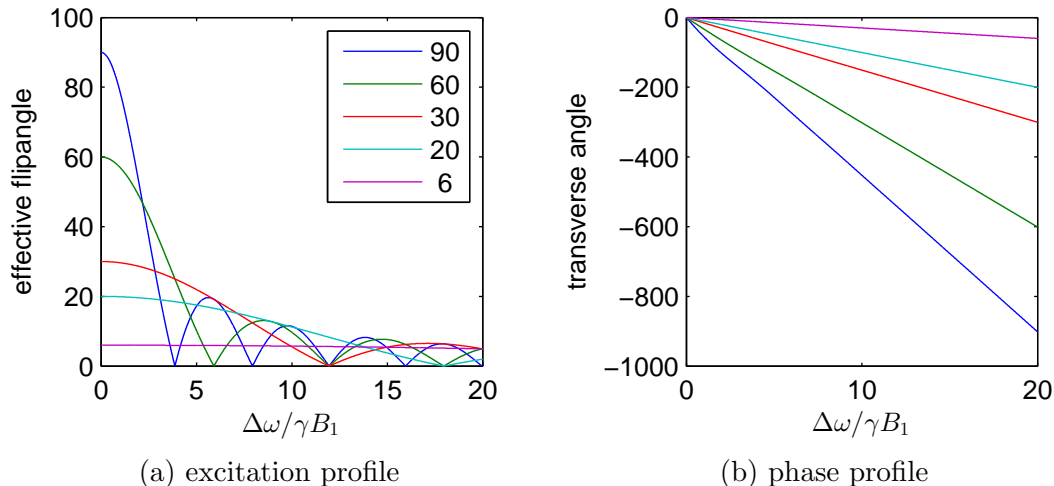


Figure 2.4: Off-resonance excitation patterns, extracted from Figure 2.3, described by Equation (2.34).

In practical implementations, however, the amplitude response due to a block pulse of α_0 , are shown in Figure 2.4a. Clearly, each pulse of certain flip angle α_0 and amplitude B_1 offers a certain *bandwidth of excitation*, which, generally speaking, becomes higher with lower flip-angles. Regarding the response for, e.g. $\alpha_0 = 6^\circ$, a relatively wide, homogeneous excitation band can be observed over large offset-frequency ranges.

Wider excitation bandwidths can additionally be obtained by shortening the pulse duration τ_p . The consequent increase of B_1 compresses the desired off-resonance bandwidth to smaller quantities $\Delta\omega/\gamma B_1$.

The ratio $\Delta\omega/\gamma B_1$ is a B_0 -independent descriptor. Given for instance an on-resonance flip angle $\alpha_0 = \pi/2$ and an available, clinically typical, transverse field amplitude $B_1 = 20\mu T$ applied on a proton ensemble yields a pulse duration of (cf. Equation (2.27) and Table 2.1)

$$\tau_p = \frac{\alpha_0}{\gamma B_1} = \frac{\pi/2}{2\pi \cdot 42.58 \frac{\text{MHz}}{T} \cdot 20\mu T} = 0.2936\text{ms} \quad (2.36)$$

for protons. The analytic expression of the cosine effective flip angle in Equation (2.34) can be used to define the excitation minima over frequency, the first taking place at a spot

$$\frac{\Delta\Omega}{\gamma B_1} = \sqrt{15} \quad (2.37)$$

Using the example from above, this yields the *first minimum* of the spectral pulse response at an offset frequency of

$$\Delta\Omega = \sqrt{15} \cdot \gamma B_1 = 3102.3\text{Hz} \quad (2.38)$$

From Equation (2.38) the influence of the transverse field amplitude B_1 is again very obvious: Although depicted for a $\pi/2$ -excitation, it is valid throughout any excitation angle. As discussed previously, higher B_1 shifts the spectral position of the first cut-off towards higher frequencies, yielding a wider excitation band.

2.2.5 Hard-pulse approximation

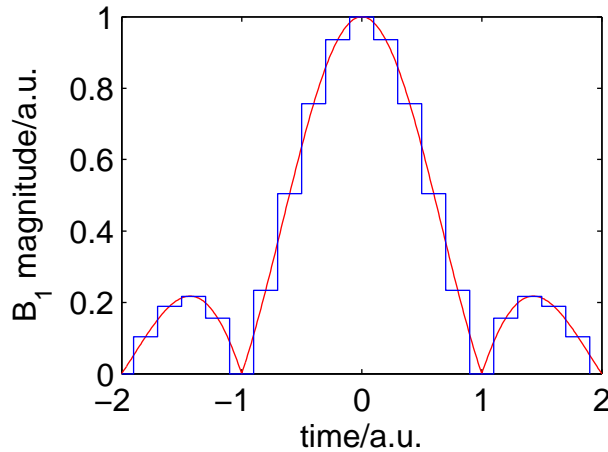


Figure 2.5: Hard-pulse approximation (blue) of a *sinc*-pulse shape (red). For each discretization step, flipping, precession and relaxation is applied separately

Calculating the effect of RF pulsing can be accomplished by numeric integration of the *Bloch* equations for arbitrarily shaped B_1 -fields. However, for the case of comparatively short *Block* pulses, a single transition matrix can be used.

A method for studying the behaviour of arbitrarily shaped pulses without performing the computationally intense integration is the division of the pulse time in discrete steps, as shown in Figure 2.5: Alternatively applying elementary pulses, followed by the precession-operator for the very period of time, yields a very accurate approximation of the numerical integration. With this method, also relaxation effects can be employed by applying relaxation operators for the discretization step following precession. In pulse design, the

hard-pulse approach is the fundamental basis for using the Shinnar-LeRoux (SLR) algorithm[5].

2.3 Spin-ensemble phenomena

Summing an ensemble of magnetic moments and yielding the new observable *magnetization* (cf. Section 2.1.3), results in handy simplifications. Compared to the observation of the behavior of each magnetic moment or *spin* individually, an overall model for the physically detectable quantity *magnetization* can be stated. The *Bloch* equations in Equation (2.9) is the simplest of these integrating formulations. However, there are factors which are yet to be modelled. These are *relaxation*, *chemical shift* and *J-coupling* and will be addressed in this section. Although, these phenomena act on the *spin* level they can be abstracted to the *magnetization* level.

2.3.1 Longitudinal relaxation

As described in Section 2.1.1, the distribution of low- and high-energy spins is covered by *Boltzmann* statistics. Using RF irradiation, the equilibrium condition amongst the spin ensemble is being disturbed. However, as the system thrives to the B_0 -imposed, directed equilibrium $M_z=M_0$, the according z -component in the *Bloch* equations are to be modified accordingly. By taking the already defined simple dynamic magnetization model in Equation (2.9), and adding a relaxation term

$$\frac{d\vec{M}}{dt} = \gamma\vec{M} \times \vec{B} - \begin{pmatrix} 0 \\ 0 \\ (M_z - M_0)/T_1 \end{pmatrix} \quad (2.39)$$

yields the *Bloch* equations comprising *longitudinal* or *spin-lattice relaxation*. As stated in [2] it is very important to recall that the equilibrium magnetization is generated by the main field B_0 .

The *longitudinal relaxation time constant* T_1 and its inverse, the *longitudinal relaxation constant* R_1 , can be measured in multi-pulse NMR-experiments which will be discussed later. Additionally, in MRI, T_1 is a major factor for the generation of contrast, since

different materials exhibit different longitudinal relaxation behavior. This can be exploited in contrast-tailoring.

Furthermore, T_1 is very dependent on the electronic and molecular environment and molecular mobility, along with B_0 and temperature. The multifactorial emergence of *spin-lattice* relaxation is covered in standard text books about NMR spectroscopy such as [6].

2.3.2 Transverse relaxation

While the variation of longitudinal signal over time is intuitive by regarding a natural system striving for equilibrium, another process affecting the transverse signal variation is treated hereafter.

Generally, magnetization can be flipped in the transverse plane by RF irradiation of certain characteristics (cf. Section 2.2). The transverse components after the pulse is again an ensemble of magnetic moments integrated to one quantity, the *transverse magnetization*. The motion of each individual magnetic moment is covered by Equation (2.6) and thus dependent on the magnetic field B and its gyromagnetic ratio γ . However, individual magnetic moments tend to mutually exchange their energy state, causing a loss of coherence amongst the spin ensemble.[7]

The classical description of transverse relaxation can thus be thought of a *loss of coherence* between the single magnetic moments, causing a decreasing sum of transverse magnetization over time, i.e. *dephasing*, which, as in the *longitudinal* case, can be described as a *transverse relaxivity time constant* T_2 or its inverse R_2 , called *transverse relaxation constant*. Integrated into the dynamic model yields a further modification of the *Bloch* equations

$$\frac{d\vec{M}}{dt} = \gamma\vec{M} \times \vec{B} - \left\{ \begin{array}{c} M_x/T_2 \\ M_y/T_2 \\ (M_z - M_0)/T_1 \end{array} \right\} \quad (2.40)$$

With Equation (2.40) the dynamic behavior of magnetization comprising magnetic moments of uniform behavior is described. In addition to the dephasing by *spin-spin* interaction, as in [8], material properties vary in a sample exposed to an external magnetic

field. Accordingly, a variable magnetic susceptibility χ in a volume confining the magnetic moments builds up magnetization as

$$M = \chi H, \quad (2.41)$$

with H being the externally generated (e.g. by a coil or a magnet) magnetic field. As χ varies as a function defined by the magnetic moments in the volume element, the induced magnetic field B varies with

$$B = \mu_0 (H + M) = \mu_0 H (1 + \chi) \quad (2.42)$$

Consequently, the variable induced magnetic field B causes changes in the angular speed ω of the individual magnetic moments according to Equation (2.7). The magnetization arising under the influence of an applied magnetic field (and consequently the induced magnetic field B in Equation (2.42)) is covered by the *Langevin* function which, amongst others, depend on temperature, the applied magnetic field and the magnetic moment of a single spin, along with the spin density.[8]

This additional signal variation again causes a further dephasing effect due to differing precession frequencies amongst the spins. On top of that, the effect is further promoted by *field inhomogeneities*, due to complex geometries in e.g. *in-vivo* acquisitions or device-dependent field inhomogeneities.

It is common to denote transverse relaxation according to their causes as

$$\frac{1}{T_2^*} = \frac{1}{T_2} + \frac{1}{T_2'}, \quad (2.43)$$

describing the overall transverse relaxation T_2^* , caused by the dephasing due to *spin-spin* interaction (cf. [7]) T_2 and susceptibility and inhomogeneity induced dephasing described by T_2' (cf. [8]).

However, when regarding atoms bound in molecules, the model is still not yet a generalization. There are several effects induced by the chemical structure which are yet to be discussed.

2.3.3 Chemical phenomena

Most atoms are bound within a defined arrangement in a molecule. Generally, the molecules do not contain just one kind of atom but a variety, which are held together by various sorts of bonds.

Upon formation of molecules, the individual atoms are not any more able to be regarded separately but as a system with each other, exhibiting mutual interaction.

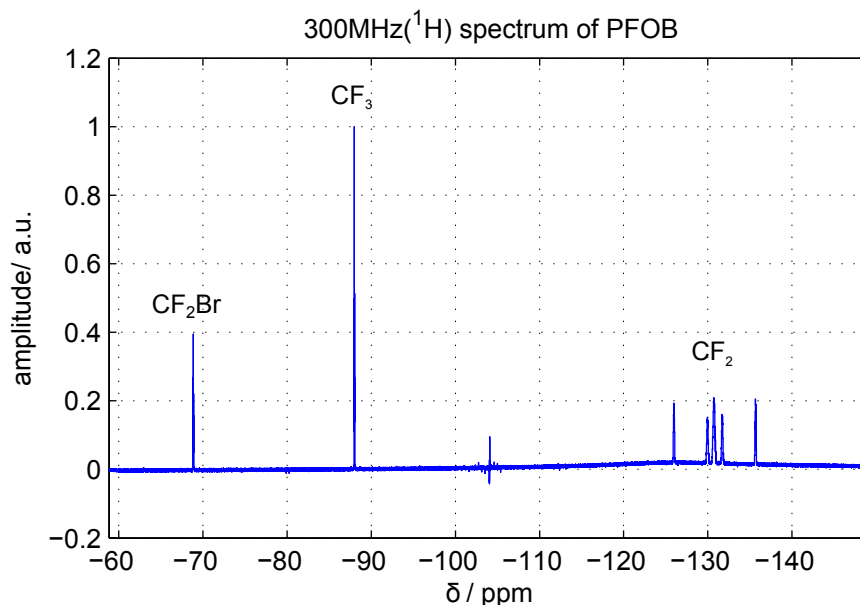


Figure 2.6: PFOB spectrum at $7T$

These interactions are manifold. Figure 2.6 shows a ^{19}F spectrum recorded on a $7T$ NMR spectrometer. The unit Parts Per Million (ppm) denotes the x-coordinate, a ratio which relates the difference between the frequency of a spectral response and a reference substance⁴ to the center frequency of the spectrometer as

$$\delta = \frac{f - f_{Ref}}{f_0} \quad (2.44)$$

The substance under investigation is PFOB, a Perfluorocarbon (PFC) which was originally used as an oxygen-carrier for blood substitutes and negative contrast agent for bowel MRI[9]. The PFOB spectrum in Figure 2.6 exhibits 3 major *resonance complexes*

⁴NMR spectroscopy of distinct nuclei use distinct reference substances. While in the case of 1H Tetramethylsilane (TMS) is in use, ^{19}F NMR uses trichlorofluoromethane

- CF_2Br at approx. -69ppm
- CF_3 at approx. -88ppm
- CF_2 from 6 groups at approx. -130ppm

These complexes also identify the main chemically similar structures in the PFOB molecule, spectrally separated by the *chemical shift* effect. The *chemical shift* can be explained by the differing *charge distribution* across the molecular structure. Caused by the electrons surrounding a certain nucleus itself, its vicinal nuclei or shared in bonds, the charge distribution is locally altered which leads to different amounts of electronic shielding of the externally applied magnetic field. The latter results in the difference in chemical shift.[10] Stating the separation in relative *ppm* instead of an absolute frequency makes the quantity independent of the applied field B_0 .

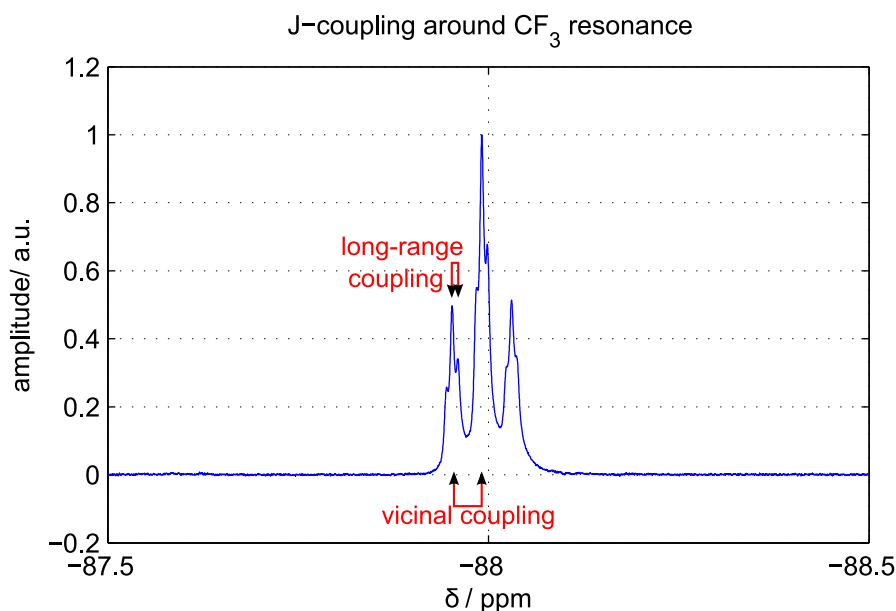


Figure 2.7: CF_3 spectral response with J-coupling at $7T$. The two distinguishable J-couplings are vicinal coupling with the adjacent and long-range coupling from more distanced CF_2 (through-space).

Regarding Figure 2.7 with a magnified section around the CF_3 shows another frequency dependency, although in another, *smaller* frequency scale. The spectral response appears to be split apart into one central line and two additional side-lobes symmetrically around the center. These resonances stem from the same molecular complex, however the fluorine atoms in the CF_3 group are influenced by means of the magnetic states of the fluorine atoms of the neighboring CF_2 -groups. The magnetic moments of individual spins are

mutually influenced by attached spins (thus the term *spin-spin interaction*), promoted by chemical bonds (vicinal coupling) or even through space (long-range coupling).[10, 11]

The analysis of J-coupling is a highly sophisticated field of physical chemistry and is, amongst other purposes, used for structural clarification of molecules. Unlike the chemical shift of nuclear species resonating at different frequencies due to their environment, *J-coupling* is not dependent on the applied magnetic field, but has an absolute value in *Hz* rather than *ppm*.

2.4 Elementary sequences in Nuclear Magnetic Resonance

NMR spectroscopy uses the static field B_0 and the oscillating field $B_1(t)$ in order to generate a tailored response of a material under investigation. The purpose of spectroscopy ranges from determining relaxation parameters (cf. Section 2.3), spectral and structural clarification or detection of specimen. Since sequences for MRI and MRSI are mostly derivatives of elementary NMR experiments, their basis is hereby treated.

2.4.1 Single-pulse acquisition

The most simple technique to obtain an NMR response of a sample is to perform an excitation pulse and observe the immediate response to that excitation pulse. Observation, in this context, means the registration of the induction caused by the projection of the magnetization onto the transverse plane. The registering element is a coil being sensitive in this very direction. Practically, the registration or *detection coil* is often the same as for generating the rotating magnetic field B_1 , i.e. the *transmission coil*.

In Figure 2.8a a simple pulse-collect experiment is shown: The transmission coil is generating an oscillating RF field in the sample, causing the magnetization to *flip* into the transverse plane (cf. Section 2.2.2). After the pulse time τ_p in which the pulse is applied, the coil is switched to *receive mode*. The magnetization vector partly or fully rotating in the transverse plane, causes an induction voltage U_{ind} in the coil which is registered as shown in Figure 2.8a. Naturally in spectroscopy, the response of a specimen under investigation consists of a magnitude of frequencies characterizing the material. These are either visible in the *temporal* domain, i.e. the Free Induction Decay (FID), but also

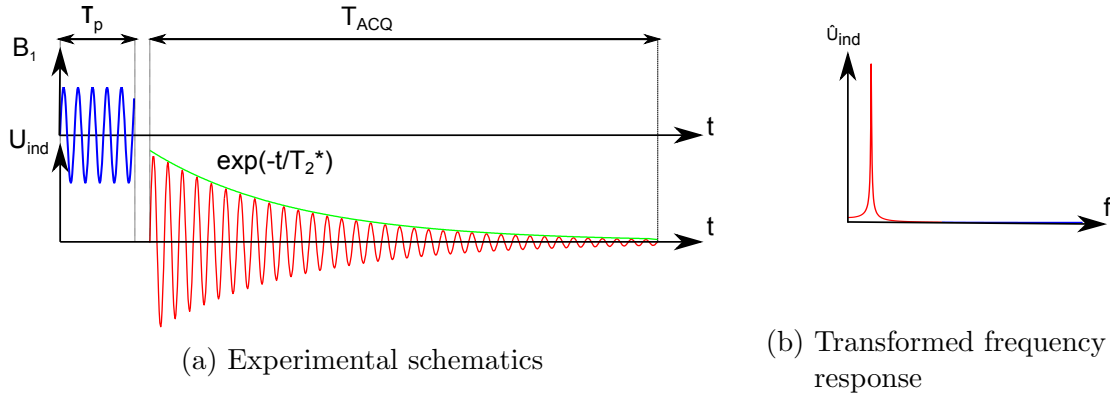


Figure 2.8: Response of a simple pulse-collect experiment.

in *spectral* domain as the spectrum of the specimen. In Figure 2.8b the spectral response of a *single-resonant* species is shown. It is characteristic that, despite the *single-resonant* kind of response, the spectral line is not an impulse function but appears broadened due to the modulated exponential T_2^* decay. Recalling Equation (2.43), T_2' is of high importance in spectroscopy, since it corrupts the spectrum by introducing *additional* spectral line broadening inversely proportional to T_2^{*5} : It is thus crucial to maximize T_2^* , especially in *multi-resonant species* in order to allow the separation of closely adjacent resonances. This is done by superposition of additional (smaller) static fields of multiple orders - i.e. *shimming gradients*, which compensate for local inhomogeneities of the B_0 field.

2.4.2 Spin Echo acquisition

Experiments in NMR usually rely on a multitude of pulses in a single experiment. With the application of multiple pulses it is possible to extract certain features out of the precessing magnetization, dependent on flip angle, pulse duration, inter-pulse duration, etc. A very intuitive multi-pulse experiment is the Spin Echo (SE) sequence.

Figure 2.9 depicts the effect of several pulses in succession. For the essay of the sequence it is crucial to assume to have a very high B_1 (cf. Equation (2.35)) in order to shift the pulsing in a *hard pulse* regime featuring three very important properties [3]:

- no precession during the pulse, due to the accordingly short τ_p (cf. Equation (2.27)), valid for any participating on- or off-resonance response,

⁵The relation between the exponential decay and the width in spectral domain is a simple *Fourier* identity yielding a *Lorentzian* distribution: $\mathfrak{F}\{e^{-|t|/T_2^*}\} = \frac{T_2^*}{1+(2\pi f T_2^*)^2}$

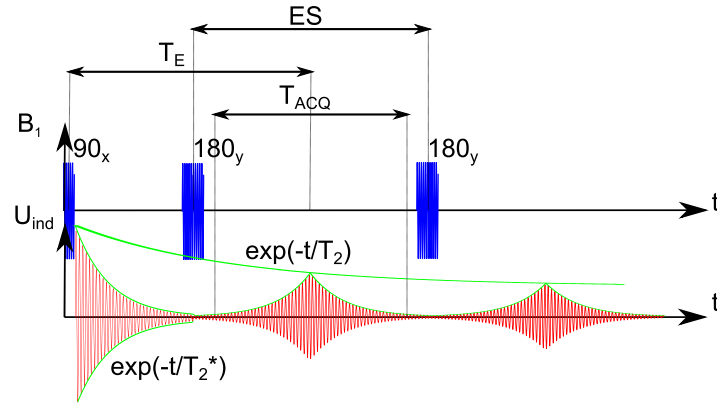


Figure 2.9: Two SEs in a multipulse experiment

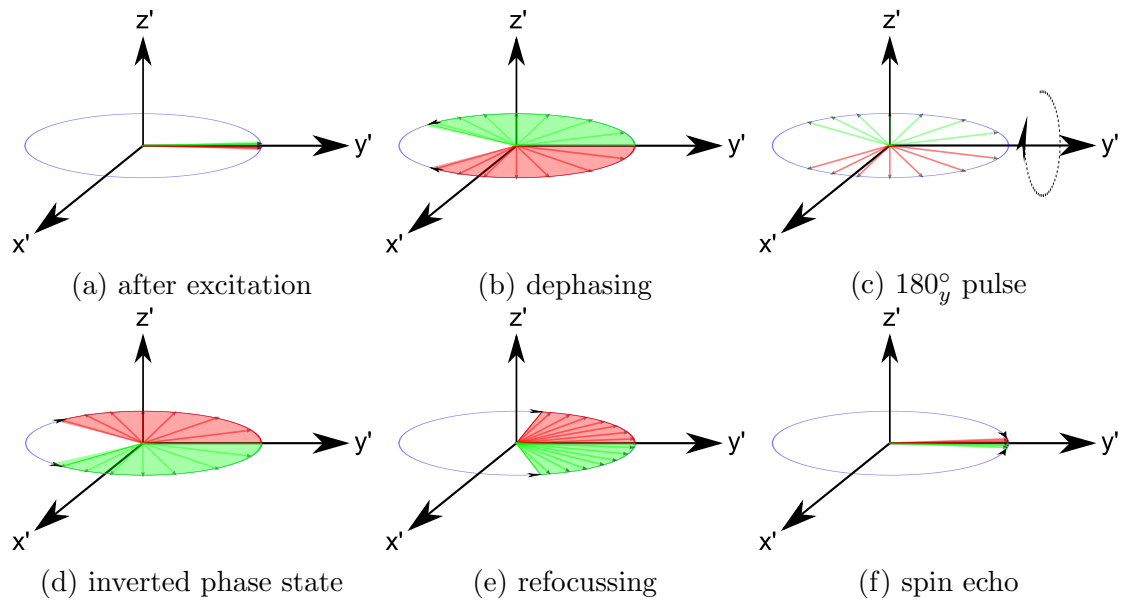


Figure 2.10: Refocussing of dephasing elementary magnetizations from excitation to SE-generation

- spectrally widely uniform flip angle $\alpha(f)$, rotating each spectral component in the same manner and phase
- relaxation effects during the pulse duration τ_p are negligible

If the mentioned properties are not met, multi-pulse experiments must be described in more mathematical detail (e.g., the rotation matrices in Section 2.2.4). For the sake of clarity, the fundamental SE sequences are treated assuming ideal, hard pulsing.

The first 90° pulse in Figures 2.9 and 2.10a is applied along the x -axis, rotating the magnetization from its equilibrium state onto the y -axis. A pictorial description is given in

Figure 2.10a, assuming *hard pulsing* and figuring the vector B_1 on the x -axis of a coordinate system rotating with a certain center frequency. Recalling the incoherent precession frequencies in the sample, the T_2^* -relaxation acts on the overall signal. Regarding solely the T_2' -relaxation components due to B_0 inhomogeneities and considering the B_0 variations to be static over time yields an additional (relative to reference frequency f_{Ref}) phase accumulation to the y -axis of

$$\Delta\varphi(x, y, \tau) = \gamma\Delta B_0(x, y)\tau = \Delta\omega(x, y)\tau \quad (2.45)$$

with τ being the elapsed time after the 90° pulse and $\Delta\omega(x, y)$ being the angular speed difference due to the static field inhomogeneity (Figure 2.10b). After some time, a certain amount of phase has been modulated onto an elementary magnetization vector and the overall signal decayed according to T_2^* . At the time of the first 180° pulse (Figure 2.10c) this phase accumulation is, according to the hard pulse-assumption mirrored around the axis of the 180° pulse, i.e. inverting the sign of the phase relative to the y -axis. However, although the phase is inverted, the angular speed stays the same (relative to the rotating frame (x', y', z') , see Figure 2.10d). Thus after another, equivalent time interval τ , the elementary magnetization vector will rephase, reversing the effect of B_0 -inhomogeneity-induced relaxation (Figure 2.10f). The point of time, the rephasing is taking place is called *echo time* T_E and equals exactly 2τ .

By refocusing of the inhomogeneity-induced dephasing, the rephased magnetization experiences a decay given by pure T_2 relaxation. Thus, the SE sequence overrides the effect of the T_2' relaxation in Equation (2.43). Moreover, by regarding Figure 2.9 it is also possible to measure the T_2 decay of a specimen by applying multiple 180° refocusing pulses at echo spacing intervals ES and sampling the peak of the single echoes.

For SE experiments, it is crucial to keep up several prerequisites. Firstly, the *hard pulse* regime as described above must be reasonably present. Secondly, both 90° - and 180° -pulse must be sufficiently calibrated in order yield proper *excitation* and *refocusing* behavior. If these requirements are not met, imperfections in the echo response will arise, which are discussed subsequently.

2.4.3 Higher-order echoes

The spin-echo experiment is fundamental in both MRI and, more generally, NMR. However, this popular experiment is amongst the simplest to explain. In the very beginning of NMR it was shown that a combination of two or more 90° also results in SEs.[12] The behavior of magnetization cannot be described in simple geometrical way as for the 90° - $(180^\circ)^n$ pulse sequence. However, a geometric interpretation is surprisingly easily done by Hennig [13], additionally discussing a more general way of describing multi-pulse experiments. The latter is summarized in the following:

Regarding an ensemble of *dephased* magnetization in the transverse plane, a state F_1 is defined, which describes the dephased spin ensemble as a whole. It can now be shown, that by applying a B_1 -pulse of any amplitude and thus an on-resonance flip angle α , the newly defined ensemble of the transverse magnetization is propagated to two population states F_1^+ , F_{-1}^+ , discriminated by solely the *reversed phase relation* compared to each other. Both F_1^+ and F_{-1}^+ experience the same phase accumulation (e.g. by B_0 inhomogeneities denoted as ΔB_0 or superimposed gradients, denoted as G) and will either dephase further or will be rephased to a *refocused state*, a SE.

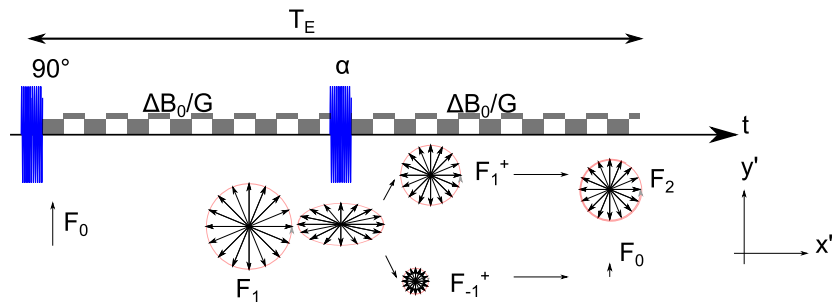


Figure 2.11: Schematics about pulsing with arbitrary angles and setting of magnetization states F . Adopted from [14]

Figure 2.11 schematically depicts the discussed magnetization states: Assuming a 90° excitation pulse (along x), flipping the magnetization onto the y - axis, the in-phase magnetization ensemble with state F_0 dephases over time, yielding the new state F_1 . The period starting with the α -pulse is different to the echo-spacing interval in Figure 2.9 discussing the 90° - $(180^\circ)^n$ pulse sequence: The *imperfect refocusing pulse* with angle α turns the dephased 'magnetization wheel' with state F_1 , partly into a plane tilted about α from the transverse plane with x' being the rotation axis. In state-space, the transverse magnetization can now be decomposed into two successive states: F_1^+ , exhibiting the same dephasing direction as F_1 and the magnetization state F_{-1}^+ with opposite phase

which when composed linearly, add up to the elliptic distribution shown under the α -pulse in Figure 2.11.

During the second half of T_E , the state with opposite phasing is now experiencing ΔB_0 and G in the same way as before. Thus, after each of the magnetizations in the ensemble has accumulated the same phase it was shifted in the first $T_E/2$, they converge on the x -axis, producing a SE. The other magnetization state, however, continues its dephasing and contributes no net signal. It is of utter importance that the approach treated here relies on a sufficient dephasing, which can be assumed in MRI equipment, exhibiting fairly high B_0 inhomogeneity and superimposed spatial coding gradients G [13]. Obviously, regarding Figure 2.11, a (perfect) 90° - 180° combination has the optimal F_{-1}^+ -yield: all dephased magnetization is rephased completely, ending up with a pure F_0 state after the second phasing period. In this case, the population of the state F_0 is easily calculated and is just the initial magnetization M_0 after the 90° pulse reduced about the transverse relaxation rate T_2 . A feature of the experiment in Figure 2.11 is that a part of *pure* longitudinal magnetization which was able to rise in the first $T_E/2$ interval, will be flipped down to the transverse plane yielding a 'fresh' state F_0 decreasing with T_2^* yielding an FID and evolving to its F_1 successor.

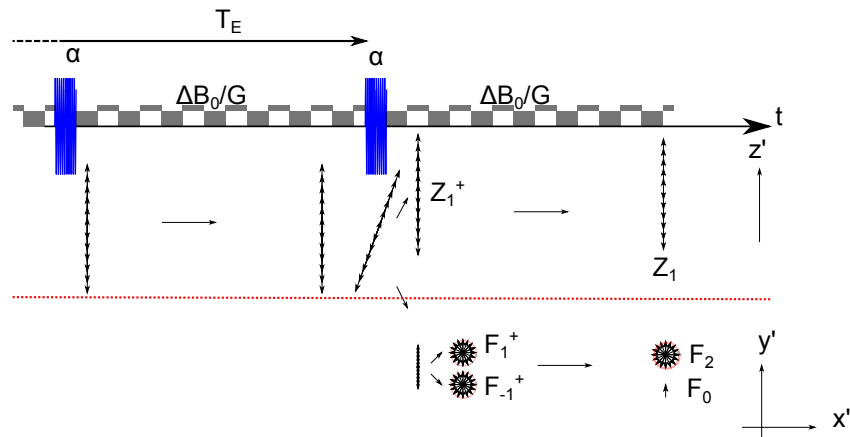


Figure 2.12: Introduction of a third RF-pulse: The main focus is put on the evolution of longitudinal phase state after the second pulse. The section on top of the red separator shows the behavior of longitudinal phase-states, the bottom the transverse phase states. Transverse phase states until T_E are regarded in Figure 2.11. Adopted from [14]

However, utilizing non- 180° refocusing pulses, also yields a state of dephased longitudinal magnetization which is zero in sum. The elliptic distribution after the third pulse in Figure 2.12 is composed of a net-zero ensemble of longitudinal magnetization, sinusoidally distributed over z *plus* a state governing the transverse magnetization in the first T_E ,

which was discussed before and by Figure 2.11.

The longitudinal magnetization state *created* by the first α pulse has great implications on the third evolution phase after the third pulse, i.e. the second α pulse. By flipping the longitudinal distribution, the transverse state gets populated, not in an F_0 - (FID)-manner but splits into two equivalently populated transverse states F_1^+ and F_{-1}^+ , one of which (F_{-1}^+) converging after a period of rephasing.

Moreover, setting up inverted dephasing situations (i.e. inverted gradient G), the equally populated F_1^+ -state rephases and yields an echo of the same amplitude but opposite phase.

This mode of an echo is no SE because of its *intermediate* character of longitudinal magnetization. Due to its nature it is called *stimulated echo*. Most importantly, the longitudinal z -state is not affected by the dephasing in the interval between the two α -pulses. The phase state is retained in this evolution phase.

2.4.4 Extended phase graphs

Magnetization states as described in Section 2.4.3 are a practical tool for depicting the influence of pulse timing, spacing and intensity in a multi-pulse sequence. Furthermore, using transition matrices and according iterative algorithms in [13, 14], each of the *refocussing paths* can be traced and added up to a quantity including all the phase states in order to calculate the magnitude of an echo response.

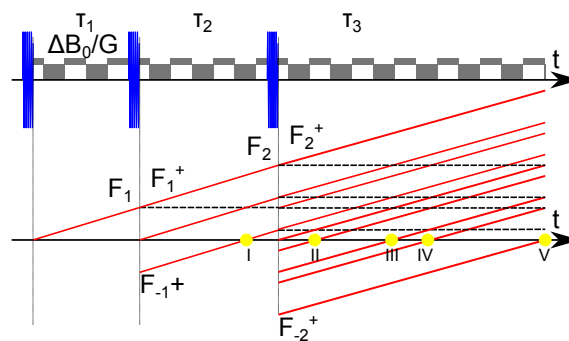
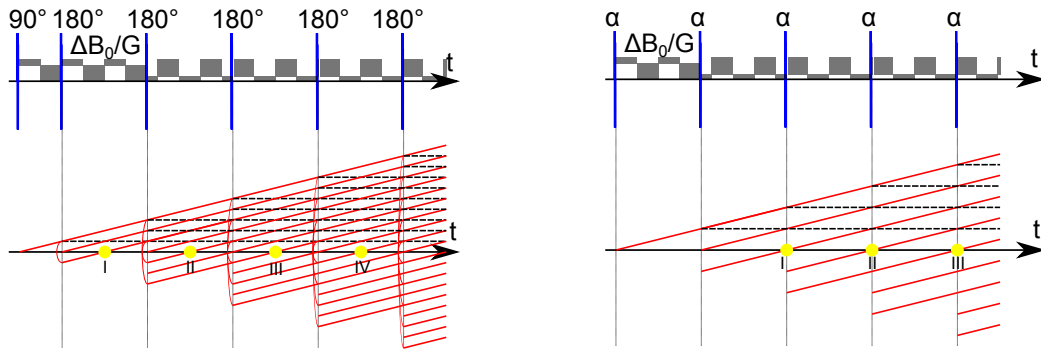


Figure 2.13: Phase graph of a *stimulated echo*-producing pulse sequence: red lines denote transverse phase-paths, black-dashed lines are stored phase-states, yellow dots indicate refocused phase-states, i.e. echoes (denoted with roman numbers I-V).

A more depictive, although qualitative, method for regarding echo formations is the *phase graph* in Figure 2.13. Using the phase graph, echo timings can be determined by regarding

the refocusing paths. A common application for the situation depicted in Figure 2.13 is Stimulated Echo Acquisition Mode (STEAM), a Single Voxel Spectroscopy (SVS) method. Very interestingly, after two preparation pulses (mostly 90°), the mixing time τ_2 is used to tailor the single phase states in order to yield an optimal signal in the acquisition interval τ_3 . By the use of unequal inter-pulse-intervals, four echoes arise in the acquisition period τ_3 , of which *three* (*II, IV* and *V*) are due to refocussed phase-states from the former mixing period τ_2 , and *one* (*III*) is the stimulated echo from a phase-state saved in τ_2 , refocussed by the third pulse. By applying additional dephasing, e.g. in form of an added gradient in the mixing time τ_2 , dephasing of the transverse magnetization can be dramatically accelerated, avoiding early SE in the acquisition phase τ_3 . The saved (*Z*-) phase-state will not be affected by the additional dephasing and will refocus at a time τ_1 after the third pulse as a *stimulated echo*. [15]



(a) 90° - 180° CPMG pulse sequence. Adopted from [13] (b) General multipulse sequence. Adopted from [14]

Figure 2.14: Phase graphs of a common sequences in NMR and MRI

In Figure 2.14 two popular types of imaging sequences are shown: Figure 2.14a is the phase graph of the SE-sequence introduced in Section 2.4.2. The actual schematic, however, takes pulse imperfections into account, i.e. the imperfect state conversion from F to F_{-n}^+ , but with contributions to the longitudinal state and F_n^+ . If the state conversion is not done perfectly, contributions from the longitudinal state (stimulated echoes) *and* echoes from higher-order phase states will be involved at echo time, indicated by the yellow dots. Especially in the first echoes, the variation of the amplitude by the multi-state contributions can vary heavily, whereas a *steady state* is approached in later echoes down the train [13]. The latter has great implications on the CSI sequence discussed hereinafter.

In Figure 2.14b, the phase graph of an equidistant pulse-train is shown. The difference to Figure 2.14a, the CPMG, is apparent: The echo is not any more set in the center of two consecutive refocusing pulses but to the end of one inter-pulse period. The total

rephased transverse magnetization (F_0) is thus the sum of refocused F_{-n} states of several pulse-generations *and* FID-contributions. After several generations, however, as for the CPMG, a steady state is reached in both contributions [14].

2.5 MRI spatial encoding

When measuring the overall NMR response of an inhomogenous object such as the human body, the result will be a summation of the responses of magnetizations with locally varying properties, i.e. relaxation, spin density and offset-frequencies. However, by superimposing magnetic fields which spatially vary the precession frequency of each constituent, the location of the single MR signals can be resolved. To accomplish this, a fundamental relationship, i.e Equation (2.7), can be used.

For convenience, uni-resonant species with a single γ will be considered. As discussed later, the spatial encoding of MRSI sequences can be set-up on this basis to a very high extent.

Using additional, superimposed gradient fields on Equation (2.7), allows to vary the frequency and thus phase of a magnetization depending on its location. Consequently, over the whole volume, spatial base functions $B(\vec{x}) = \exp(i2\pi\phi(\vec{x}))$ modulate the local MR signals. Ideally, the detector *uniformly* senses the complex magnetization $\underline{\mathbf{m}}(\vec{x})$ in the domain Ω . The signal will be proportional

$$s \propto \int_{\vec{x} \in \Omega} \underline{\mathbf{m}}(\vec{x}) e^{i2\pi\phi(\vec{x})} d\vec{x} \quad (2.46)$$

In general, the gradients \vec{G} are applied in a linear manner along each principal axis with a zero-crossing in the central part of the B_0 -field, the *isocenter*. Turned on for a certain amount of time τ_G the phase change (referring to the γB_0 rotating frame) states

$$\phi(\vec{x}, \vec{G}\tau_G) = 2\pi\gamma \vec{x} \cdot \vec{G}\tau_G \quad (2.47)$$

The signal will have different phases ϕ , depending on the spatial localization. Inserting Equation (2.47) in Equation (2.46) therefore yields

⁵It should be noted, that the phase results from an integral when using non-constant gradients $\vec{G} = \vec{G}(t)$ instead

$$s(\vec{G}\tau_G) \propto \int_{\vec{x} \in \Omega} \underline{\mathbf{m}}(\vec{x}) e^{i2\pi\gamma \vec{x} \cdot \vec{G}\tau_G} d\vec{x} \quad (2.48)$$

Substituting $\vec{k} = \gamma \cdot \vec{G}\tau_G$ yields the well-known multi-dimensional *Fourier* integral

$$s(\vec{k}) \propto \int_{\vec{x} \in \Omega} \underline{\mathbf{m}}(\vec{x}) e^{i2\pi\vec{x} \cdot \vec{k}} d\vec{x} \quad (2.49)$$

with the gradient-set spatial frequency \vec{k} . The prepared (e.g. by excitation or refocussing) magnetization $\underline{\mathbf{m}}(\vec{x})$ is accordingly sampled in \vec{k} -space by applying \vec{x} -dependent phase terms $\vec{G}\tau_G$. MRI- k -encoding happens in discrete steps. By sampling theory, the discretization in k -space affects the properties of the spatial domain accordingly. The lowest sampling range in k -space according to the *Nyquist* theorem is double the occurring spatial frequency. Thus, the outer borders of k -space are a measure of resolution of the image, whereas the discretization steps define the Field of View (FOV). The *Nyquist* limit for the sampling in k -space is stated as [2]

$$\Delta k = \frac{1}{FOV} \quad (2.50)$$

Accordingly, for fixed gradient application times τ_G , the sampling interval is achieved by gradient steps of

$$\Delta G = \frac{1}{\gamma\tau_G FOV} \quad (2.51)$$

In order to sample a discrete (1D) *Fourier* domain with N complex elements, N base functions have to be applied covering the range up to the highest spatial frequency, i.e. voxel size. Figure 2.15 shows a set of phases of base functions used to encode a 9×9 pixel domain. The outermost frequency $k = -4$ shows the highest frequency, i.e. phase derivative. The frequency gets lower with lower quantities of k with being $k = 0$ at the DC part.

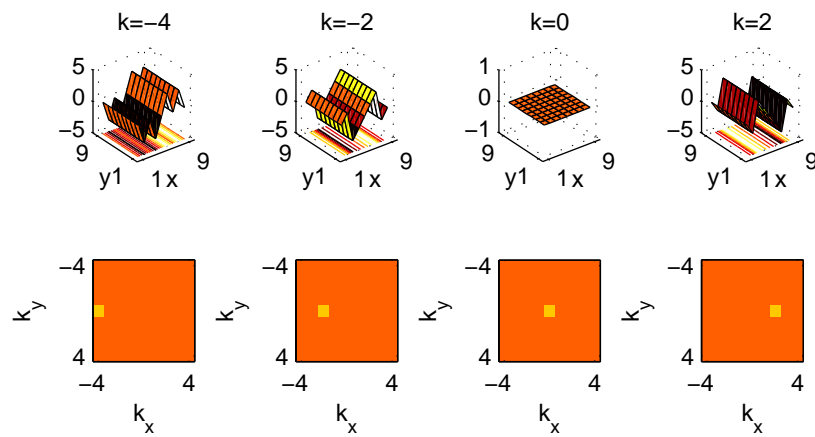


Figure 2.15: Phases of 1-dimensional base functions encoding one dimension of a 9×9 domain. Below, the addressed k -coordinates are depicted.

3 Methods and Material

Subsequently, the used analytical foundation and sequence simulations will be described. Furthermore, aspects of the tested sequences such as timing and field amplitudes are highlighted. Additionally, the experimental settings are listed and the used phantoms are described in both content and geometry.

3.1 Magnetization throughout multiple pulses

Although, echo amplitudes can be calculated by using the phase graph algorithm [13], the magnitude of a single magnetization is of interest. Whereas the first method regards ensembles of magnetization and requiring their total dephasing, single magnetizations can be described according to the *Bloch* equations in Section 2.1.2. In order to trace the orientation of magnetizations exhibiting certain frequency and relaxation features two ways can be pursued. Primarily, but in most cases computationally extremely costly is to numerically integrate the *Bloch* equations. Employing e.g. Runge-Kutta solvers, requires the integration in small increments approaching a final time of interest, for example echo time T_E [16].

On the other hand, a single magnetization exposed to an RF irradiation can be appropriately described by transition matrices. The latter approach has already been used in Section 2.2.3 where the initial equilibrium magnetization state was deflected by the application of an RF irradiation. This process was described by Equation (2.32). Special solutions of the *Bloch* equations yield transition matrices for either

- signal evolution or simply *rotation*,
- relaxation,
- and, most importantly, pulsing.

Solving the equations without the influence of the B_1 terms is straight-forward, solving a linear system of differential equations with constant coefficients[16]. However, an analytical solution of the system involving RF-pulses is demanding and only obtained for certain cases, such as the *block* pulses: When assuming *block* pulses, i.e. a single RF-frequency turned on for a certain amount of time τ_p , a solution of the system to any initial condition can be derived as shown in Section 2.2.4. Albeit neglecting relaxation effects during the time of RF-pulsing the emerging matrices make an appropriate transformation of magnetization state which is provided by the fact that, even when pulsing with comparatively low amplitudes B_1 , τ_p will be about magnitudes smaller than the relaxation time constants T_1 and T_2 . On the other hand, especially when going towards NMR spectroscopy and when using comparatively high B_1 amplitudes, i.e. $\Delta\omega \ll \gamma B_1$, *off-resonance* effects through pulsing are widely neglected. The rotation is then just modelled by a single rotation operator with one argument, the flip angle (c.f. [17]).

3.1.1 Magnetization evolution

Regarding *pure evolution*, the *Bloch* equation in the rotating frame of reference and including relaxation terms denoted by the relaxation matrix \mathbf{R} reads (cf. Equation (2.20))

$$\begin{aligned} \frac{d\vec{M}'}{dt} &= \vec{M}' \times (\gamma\vec{B} + \Omega) + \mathbf{R} = \vec{M}' \times \begin{Bmatrix} 0 \\ 0 \\ \Delta\omega \end{Bmatrix} \\ &= \begin{bmatrix} -1/T_2 & \Delta\omega & 0 \\ -\Delta\omega & -1/T_2 & 0 \\ 0 & 0 & -1/T_1 \end{bmatrix} \begin{Bmatrix} M'_x \\ M'_y \\ M'_z \end{Bmatrix} + \begin{Bmatrix} 0 \\ 0 \\ M_0/T_1 \end{Bmatrix} \end{aligned} \quad (3.1)$$

This linear, inhomogenous set of differential equations with constant coefficients can be easily solved analytically (using the notation of Hargreaves et al. [18]), yielding

$$\begin{Bmatrix} M'_x(t) \\ M'_y(t) \\ M'_z(t) \end{Bmatrix} = \begin{Bmatrix} e^{-t/T_2} (M'_x(0)\cos(\Delta\omega t) + M'_y(0)\sin(\Delta\omega t)) \\ e^{-t/T_2} (-M'_x(0)\sin(\Delta\omega t) + M'_y(0)\cos(\Delta\omega t)) \\ M_0 (1 - e^{-t/T_1}) + M'_z(0)e^{-t/T_1} \end{Bmatrix} \quad (3.2)$$

Further decomposition of the matrix in Equation (3.2) yields

$$\begin{pmatrix} M'_x(t) \\ M'_y(t) \\ M'_z(t) \end{pmatrix} = \mathbf{P}(t)\mathbf{C}(t)\vec{M}'(0) + (\mathbf{I} - \mathbf{C}(t)) \begin{pmatrix} 0 \\ 0 \\ M_0 \end{pmatrix} \quad (3.3)$$

with

$$\mathbf{P}(t) = \begin{bmatrix} \cos(\Delta\omega t) & \sin(\Delta\omega t) & 0 \\ -\sin(\Delta\omega t) & \cos(\Delta\omega t) & 0 \\ 0 & 0 & 1 \end{bmatrix} \text{ and} \quad (3.4)$$

$$\mathbf{C}(t) = \begin{bmatrix} e^{-t/T_2} & 0 & 0 \\ 0 & e^{-t/T_2} & 0 \\ 0 & 0 & e^{-t/T_1} \end{bmatrix}$$

3.1.2 Block-pulse response

In Section 2.2.3 the matrix formulation for an excitation case was already discussed. However, in the derivation of the nominal and effective angle of excitation, relaxation was omitted. Including inhomogeneity in the form of relaxation parameters in addition to B_1 perturbation yields a system lacking an analytical solution.

However, considering the ratio between relaxation time constants T_1 , T_2 and pulse time t_p , it is feasible to omit relaxation for the time of pulsing. This yields the formerly derived four-parameter in Section 2.2.4.

Referring to Section 2.2.4, there are scenarios of very short pulse durations, where even rotation throughout the pulse can be neglected. These scenarios requiring high- B_1 amplitudes which typically apply in NMR spectroscopy, in contrast to MRI, where limited B_1 is available for both patient safety and instrumentation reasons. Described for SE in Section 2.4.2 the so-called *hard-pulse* approaches demand only a single parameter in the rotation operator, the flip angle α , i.e. the rotation matrix in Equation (3.4).

$$\vec{M}'(t) = \begin{bmatrix} 1 & 0 & 0 \\ 0 & \cos(\alpha) & \sin(\alpha) \\ 0 & -\sin(\alpha) & \cos(\alpha) \end{bmatrix} \vec{M}'(0) = \mathbf{R}(\alpha)\vec{M}'(0) \quad (3.5)$$

for a B_1 -application along the x-axis. Rotations about other axis positions in the transverse plane can be modelled accordingly.

3.1.3 Sequential magnetization propagation

For cases other than a simple spin-echo sequence with perfect pulses described in Section 2.4.2, geometrical interpretation of magnetization is rather tedious. Besides the extended phase graphs, sequentially applying the previously defined transition matrices yields the outcome of an experiment *for one isochromat*. This is very useful when coping with *off-resonance* pulsing, since either temporal and, even more importantly, *spectral* characteristics can be derived.

Using this approach, Bain, Kumar Anand, and Nie [19] derived the backgrounds of oscillating CPMG responses using an *Eigen decomposition* of combined transition matrices down the echo train. Hürlimann and Griffin [20] investigated the *steady-state* behaviour of CPMG pulse sequences with a similar approach, although from a rotation-axis point of view. Both, however, state oscillatory behaviour in the CPMG echo train involving off-resonance effects. The transition matrix treatment is fundamentally different to the extended phase graph algorithms in Section 2.4.4 which regard imperfect but *hard* pulses. Both approaches predict variable echo responses of the echo train - accordingly, pulsing off-resonance can be regarded as type of pulse-imperfections.

3.2 Chemical Shift Imaging (CSI) sequences

MRI-sequences are manifold. Typically, in MRSI, an existing MRI sequence is altered in order to fit the requirements of the MRSI sequence. In imaging, continuous gradients are used in order to encode whole trajectories in k -space in one *readout* attempt. Mathematically this equals a repeatedly applied phase gradient. However, in imaging, magnetization is prepared just once and then temporarily sampled under an ongoing gradient. This ongoing gradient is typically referred to as *readout gradient*, yielding a *frequency encoded signal*. The typical acquisition time in a simply repeated experiment is

$$T_{acq} = T_R \prod_{i=0}^{N-1} N_i \quad (3.6)$$

for N spatial dimensions with N_i pixels each. T_R specifies the repetition time of the pulsing, highly dependent on the relaxation parameters of the specimen under investigation

In MRSI sequences the time-axis during sampling is used differently: Instead of spatial encoding with frequency encoding profiles, the evolution of the magnetization with time is sampled, thus retaining spectral information after *Fourier* transformation. Although being key for fast sampling, *frequency encoding* corrupts quality when dealing with multi-spectral responses. In proton imaging this is known as *water-fat shift*, where off-resonance fat contributions are shifted about the corresponding *pixel bandwidth* in readout direction, with respect to the (intended) water resonance.

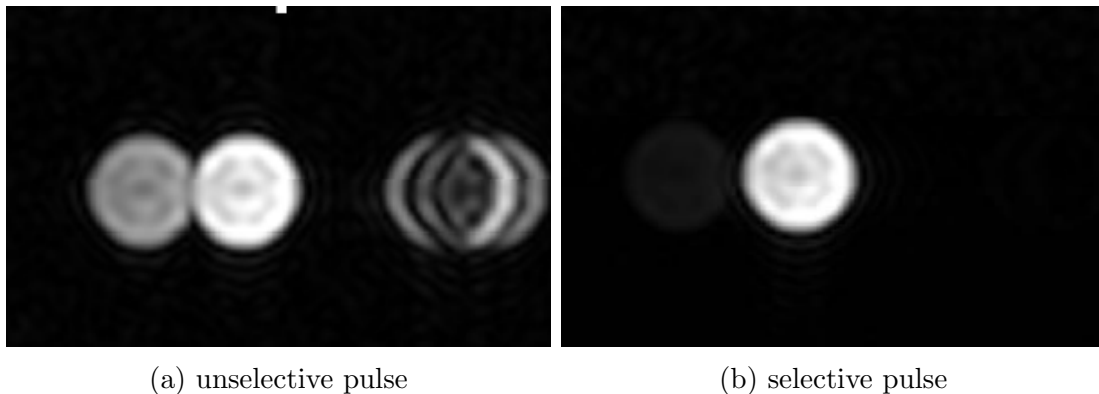


Figure 3.1: ^{19}F gradient-echo acquisitions featuring comparable geometry but different pulse bandwidths. The acquisition solely differs in the excitation of the multi-spectral specimen (PFOB). Clearly visible is the induced shift of the different resonance complexes. From Yildirim et al. [21]

Figure 3.1a shows the *water-fat equivalent* shift for the three resonance complexes of PFOB using broadband, non-selective pulses. Restricting the bandwidth of the pulses yields selective imaging of the central resonance complex, whereas signal of the side-complexes disappear almost completely (Figure 3.1b). However, with attenuating the side lobes by selective pulsing, spectral information and, moreover, signal energy contributed by the offset complexes is lost. In order to *preserve* the spectral information and the accompanying signal energy, MRSI is introduced. Mathematically, the CSI coding integral states

$$s(\vec{k}, t) \propto \int_{-\infty}^{+\infty} \int_{\vec{x} \in \Omega} \underline{\mathbf{m}}(\vec{x}, t, \Delta f) e^{i2\pi(\vec{x} \cdot \vec{k} + \Delta f t)} d\vec{x} d\Delta f \quad (3.7)$$

The MRI-coding integral is thus extended by another integration over all off-center frequencies Δf . The *frequency encoding* profile is exchanged by a *spectral* profile - the spatial encoding is solely accomplished by incrementally applied phase encoding gradients.

Again, in a discrete sampling system, according to the rules of Discrete Fourier Transformation (DFT), the sampling time T_S of the acquired signal determines the spectral resolution, whereas the (discrete) sampling interval sets the bandwidth, of which more later in the description of the sequences. This modus is called *ND-spatial 1D-spectral method* [2].

It is crucial to mention that, when introducing offset-frequencies, the spatial encoding done by the phase encoding gradients is, by regarding Equations (2.44) and (2.47), altered. Of course, this has implications on the mapping of the magnetization in k -space. However, when dealing with *chemical shifts* (cf. Section 2.3.3) which are in the order of several *ppm*, it is valid to neglect this additional phase accumulation in the complex exponential [22].

3.2.1 Classical Chemical Shift Imaging

Originally, CSI sequences e.g. for determining ^1H -, ^{13}C - or ^{31}P -containing metabolites in the brain were implemented rather simple. They consist of either a phase encoded *pulse collect* experiment or, due to sampling difficulties of the former, in an *echo collect* approach, sampling after one combination of 90° - 180° [2]. These can be considered as basic, phase-encoded NMR experiments (see Figures 2.8a and 2.9). Applying these CSI methods on specimen with higher relaxation time constants, they tend to be very time consuming. After each acquisition, the magnetization is supposed to be equilibrium in order to provide the same integrand of the encoding integral in each encoding step. Considering a repetition time T_R for each phase encoding step and an *ND*-spatial resolution yields an acquisition time T_{acq} of [2]

$$T_{acq} = T_R \prod_{i=0}^N N_i \quad (3.8)$$

Even when taking optimal excitation into account⁶, T_R can be in the order of seconds for many species due to long relaxation time constants. The time necessary to spatially

⁶The analytical description of the T_R/T_1 -optimal *Ernst* angle is done later in Section 3.2.3

encode a certain volume can thus be extensive.

3.2.2 Fluorine ultrafast Turbo Spectroscopic Imaging

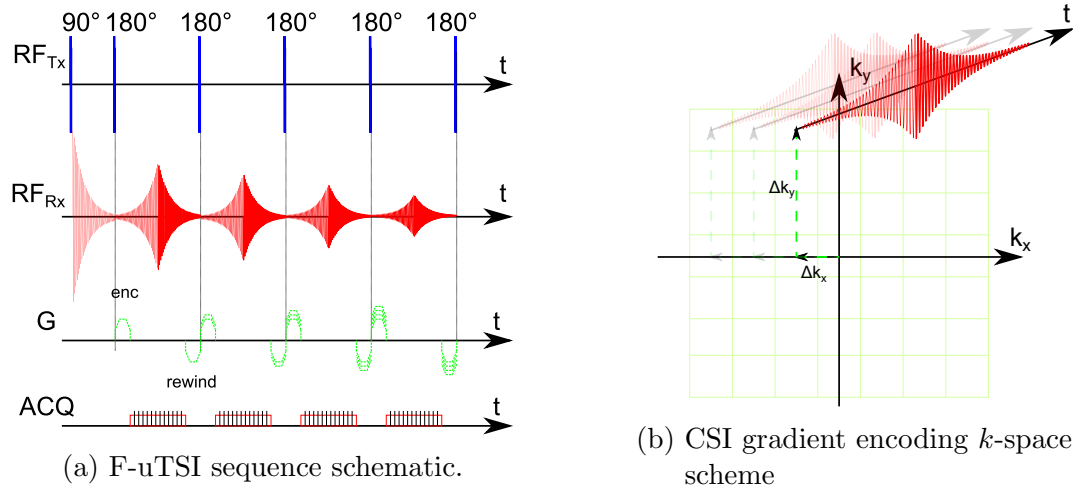


Figure 3.2: a: From top to bottom the elements RF transmission RF_{Tx}, RF reception RF_{Rx}, gradients G and acquisition ACQ is illustrated. b: *cartesian* sampling scheme in a phase-encoded CSI sequence

Considering the amount of time necessary for a classic CSI acquisition, an acceleration method is desirable. As in Section 2.4.2, the SE can be employed to reverse dephasing effects to a certain extent and consequently enables multiple sampling per excitation. The principal method stems from Turbo Spin Echo (TSE) imaging of MRI. The idea is to repeatedly refocus magnetization up to a feasible limit set by the T_2 decay (see Figure 2.9). Each of the echo responses is phase encoded in N dimensions and the SE containing the multiple spectral responses of the specimen is sampled. After the acquisition of the phase encoded response, superimposed phases are *rewound* in order to avoid newly generated phase states and accompanying echoes in addition to the spin-echo at echo time. This approach has been introduced for ^1H and typically applies 2 to 3 refocussing cycles per excitation[23]. In order to perform fast CSI on highly chemical shift-dispersive fluorine compounds, F-uTSI was developed [21, 24]. Figure 3.2a depicts a basic F-uTSI sequence with several echo generations and according sampling windows, encoded with the outlined gradient pattern. Each of the echo responses fills a k -space coordinate following a geometric pattern, e.g. *cartesian* (see Figure 3.2b and Section 3.6). A data cube of $N + 1$ spatial and temporal dimensions is thus filled successively.

The descriptors for the sequence are basically the same as for a usual SE sequence. However, unlike imaging, the interpulse Echo Spacing (ES) is used for acquiring the echo without the modulation by *readout* gradient fields - the frequency-encoding gradient is simply skipped while signal acquisition is still maintained. The profile is mainly characterized by the duration (ES) and the number of samples inside the sampling window. DFT sets the limits for both spectral range and spectral resolution according to the sampling window.

sampling considerations

Choosing the ES in SE sequences is crucial for reasons of T_2 decay. In SE-CSI, such as F-uTSI, it also determines the spectral resolution. Accordingly, a trade-off has to be found between yielding the optimal signal intensity in the beginning of the T_2 -decay and obtaining an appropriate spectral resolution Δf . A further spectral measure is the bandwidth BW or *spectral range*, which is inversely proportional to the sampling interval or *dwell time* T_d . The spectral bandwidth is needed to cover the entire spectral response of a PFC. Setting the dwell time too long leads to undersampling of the signal and to spectral aliases, undermining the ability to identify a PFC by means of its spectrum.

On the other hand, the spectral resolution determines the discriminability in the spectral domain, e.g. to resolve the different chemical species. If the spectral resolution is chosen too coarse, resonances which are in near spectral vicinity are integrated under the broad sampling kernel and appears unified in one point of the DFT.

PFCs naturally exhibit large chemical shift dispersions, and the individual spectral responses are sufficiently separated. Accordingly, the minimum of the ES determines the desired minimal spectral resolution. It is set to a suitable value to cover the spectral responses of all species being imaged, avoiding undersampling.

Naturally, hardware limitations are present in an MRI system in terms of sampling frequency f_s of the Analog-to-Digital Converter (ADC). Therefore, following *Shannon's* sampling theorem, the spectral bandwidth is limited according to $f_{s,max}/2$. Furthermore the gradient strength is crucial for the length of the sampling window which is inversely proportional to the spectral resolution. The length T_s of the sampling window can be derived from the sequence timing parameters as

$$T_s = ES - \tau_p - 2\tau_G, \quad (3.9)$$

with τ_p being the pulse duration, τ_G the gradient application/encoding time, and the echo spacing ES .

echo response

Assuming high B_1 -amplitudes of the used *Block* excitations, low B_0 -inhomogeneity and perfectly tuned instrumentation yielding exact 90° - 180° combinations in both phase and amplitude, a pure SE repetition can be achieved.

Another factor when phase-encoding gradients are used, is the necessity to roll back the phase accumulation to the zeroth or, when regarding geometrically dynamic process such as flow, also to higher orders [25] in order to avoid additional and unwanted phase coherences. This *phase-rewinding* is depicted in Figure 3.2a.

Regarding again Equation (2.49) it is crucial to provide the same integrand $\underline{m}(\vec{x})$ in each SE acquisition. If not, the inverse DFT may be modulated with a non-compact Point Spread Function (PSF) lacking spatial locality. Quite clearly, many parameters influence the response of a CPMG sequence. Using a matrix approach from Section 2.2.4 or one derived by Casanova, Perlo, and Blümich [26] the response of a CPMG can be simulated. The parameter-field consists of

- Echo Spacing ES ,
- B_1 amplitude and correlated pulse duration t_p (cf. Equation (2.27)),
- offset frequency and
- relaxation time constants T_1, T_2 .

Due to this high-dimensional parameter set, simulations are carried out using the F-uTSI standard settings published in [24]. The spectral range is restricted to $5000Hz < \Delta f < 5000Hz$ in order to retain assessability. A value $T_R = 1s$ has proved to be optimal for F-uTSI acquisitions and will thus be the basis for the simulations.[21]

Regarding previous studies, the echo-response of imperfectly pulsed CPMG sequences vary greatly (cf. [3, 13, 20, 27]). However, over the echo train, oscillations of the CPMG response converge into a *pseudo-dynamic steady state* over time[28]. Analytically, using pulse-phase cycled acquisitions, the steady state magnitude can be derived using an *Eigenvector* analysis of the echo train [20]. This steady state condition can be used to

acquire F-uTSI responses containing neither spectral oscillations nor the accompanying modulation of the PSF.

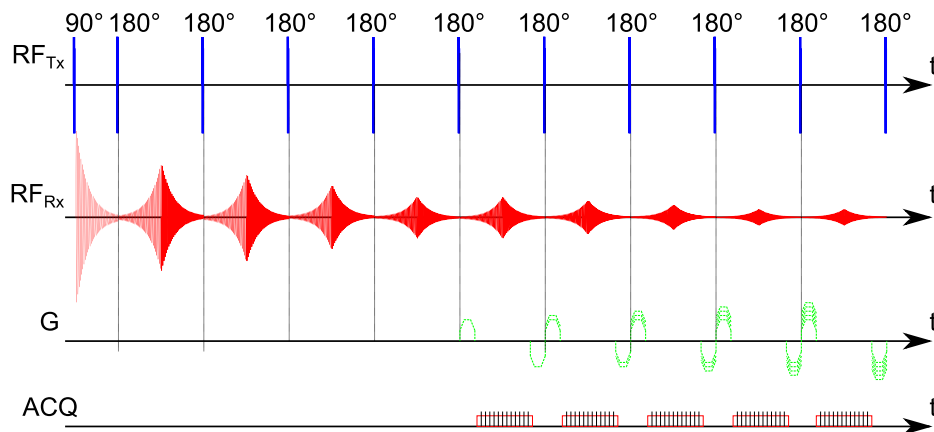


Figure 3.3: Depiction of applied *echo skipping*: 4 echoes in beginning of the echo train are skipped, i.e. left unencoded and unsampled. Encoding gradients are applied solely for sampled echoes.

Experiments were carried out comparing the difference of using early echoes and later echoes approaching the dynamic steady states. Early echoes were then simply left unencoded and unacquired, while gradients and acquisition were turned on for the later echoes. This implementation is called *echo skipping* and is illustrated in Figure 3.3.

Additionally, simulations using the derived matrix approaches for magnetization propagation were performed with parameterizations modelling the F-uTSI set-up.

3.2.3 Steady State Free Precession-Chemical Shift Imaging

In addition to CPMG approaches, steady state techniques are used for fast MRI and thus for variants of MRSI. Generally, steady-state approaches are favorable for their high Signal-to-Noise ratio over time (SNR_t) and fast acquisition time T_{ACQ} [29]. However, compared to CPMG, where the ideal response is characterized by spin density and T_2 decay only, the output to ideal SSFP pulsing is a function depending on the pulses' flip angle α , relaxation time constants T_1 , T_2 and repetition time T_R . The basic schematic is depicted in Figure 3.4.

In MRI, due to a strong off-resonance dependency, fast SSFP sequences are very susceptible to B_0 -inhomogeneity, which results in so-called *banding-artifacts*, shadows in off-resonant parts of the imaged region. Relating to spectroscopy, the banding-artifact corresponds to periodical dips in the spectral response. Unlike CPMG pulse sequences,

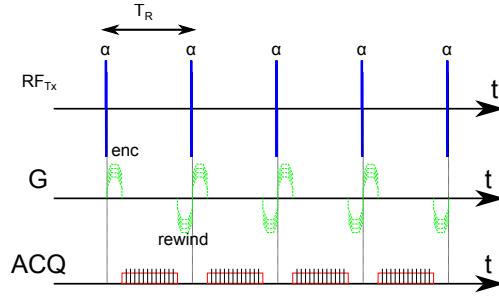


Figure 3.4: SSFP pulse sequence with CSI phase encoding gradients

however, these dips are shown to be very predicatable and, more importantly, appear uniformly within consecutive sampling intervals. The latter provides a stable integrand in Equation (2.49), which is the prerequisite to obtain a spatially compact PSF function and unmodulated spectra.

Different SSFP sequences were implemented and their performance was compared to the F-uTSI sequence in terms of image quality, spectral quality and Signal-to-Noise ratio (SNR).

pulse response

After sufficient preparation pulses the signal reaches steady state and is described by a comparatively simple analytical solution. In a regime where the pulse repetition time T_R is large compared to the transverse relaxation time, the FID contribution (cf. Section 2.4.4) is given by the steady state formulation [2, 14]

$$s_{FID}(\alpha, T_1, T_R) = M_0 \sin(\alpha) \frac{1 - e^{-T_R/T_1}}{1 - e^{-T_R/T_1} \cos(\alpha)} \quad (3.10)$$

with α being the flip angle. The optimal flip angle α_{opt} is given by the *Ernst* angle, analytically defining the maximal steady state-magnitude

$$\alpha_{opt}(T_R, T_1) = \arccos(e^{-T_R/T_1}) \quad (3.11)$$

in the $T_R \gg T_2$ -regime.

Thus, the flip angle can be tuned optimally to yield maximum signal amplitude for a defined specimen [2, 30]. It has to be mentioned that these considerations are for near-resonant cases.

The need for speeding up acquisition naturally means a speedup in pulsing frequency and thus a shortened T_R , consequently entering a regime where the assumption of complete transverse relaxation cannot be assumed for SSFP. SSFP sequences have been carefully analyzed in MRI. Because of their sensitivity to B_0 inhomogeneities the short T_R leads to the *banding artifacts* mentioned before.

Hargreaves et al. [18] uses a rotation matrix approach, already described for the simulation of spectral magnetization response in the F-uTSI pulse sequence. However, other than calculating the magnetization contributions for each sampling interval, the signal is assumed to be in steady state. The transition between two consecutive sampling period is described by

$$\vec{M}_{k+1} = \mathbf{A}\vec{M}_k + \vec{B} \quad (3.12)$$

where \mathbf{A} and \vec{B} are constructed of rotation-, pulse- and relaxation matrices (cf. Sections 3.1.1 and 3.1.2). However, assuming a steady state, $\vec{M}_{k+1} = M_k = M_{SS}$ and thus

$$\vec{M}_{SS} = \mathbf{A}\vec{M}_{SS} + \vec{B} \rightarrow \vec{M}_{SS} = (\mathbf{I} - \mathbf{A})^{-1} \vec{B} \quad (3.13)$$

The resultant expression for the transverse magnetization of \vec{M}_{SS} contains fairly complicated terms, being dependent of α , T_R , T_1 and T_2 . While Hargreaves et al. [18] did not regard for limited-power pulses, the implication of the latter suggests an additional dependence of the γB_1 and the correlated pulse-duration τ_p . Simulations were thus carried out, regarding limited power RF-pulses, investigating both the small-band and the broadband behaviour of those γB_1 -dependent SSFP pulse sequences.

3.3 Linear Combination Steady State Free Precession-Chemical Shift Imaging

Investigations of SSFP pulse sequences in MRI are extensive. Mostly, methods for the alleviation of the mentioned off-resonance banding artifacts are being treated [29, 31, 32].

Most interestingly, it is possible to shift the SSFP response frequency-wise by applying pulses of consecutively incremented phase. As shown in [31, 33], multiple acquisition SSFPs can be used to tailor the frequency response of the steady-states dependent on their phase increments. Vasanawala, Pauly, and Nishimura [31] thus introduced *two-phase* and *four-phase* imaging, stating the elimination of the typical suppression bands by incrementing pulse phases about 180° (*two-phase*) or 90° (*four-phase*). While the method of phase-cycled SSFP can be used for chemically selective separation of constituents in MRI, the method can also be exploited for broad-band CSI, as shown by [34, 35].

After acquisition, the single responses, i.e. n data sets from n -*phase* imaging, are subsequently summed using e.g. componentwise or quadratic summation. Dependent on the chosen summation, the overall spectral response varies. Bangerter et al. [33] states a low amplitude variation behaviour for componentwise, i.e. *linearly combined* SSFP responses - Linear Combination Steady State Free Precession (LCSSFP). Other methods such as quadratic summation, on the other hand, outperforms previous method in terms of SNR, by weighting the amplitude according to the frequency response according to the square.

Simulations of spectral responses were carried out (as for the ordinary SSFP) using parameters for optimally sampling the broad spectrum of e.g. PFOB. Accordingly, a 10kHz frequency range was chosen in order to investigate the broadband behaviour of the emerging spectral response. Lower ranges are simulated to appropriately determine near-resonance behaviour and banding characteristics of the SSFP responses.

The response of highly dispersive PFOB was investigated in experiments using low-power pulses. Both the spectral responses to single phase increments and the overall, linearly combined response were measured. It should be noted that the acquisition phase is cycled in the same manner as the pulse phase, both in simulations and acquisitions.

At *Philips Research* the aim is to detect early stage colorectal cancer by ^{19}F MR. The *PFOB* is encapsulated in a *PGLA* shell as shown in Figure 3.5c. The shell can now be functionalized with antibodies for specific targeted binding. The mean particle size is $\approx 1.5\mu\text{m}$ and the emulsion are usually 10% (w/v)

3.5 PFC samples

For characterizing the sequences, different phantoms were in use. In order to show the imaging capabilities of the pulse sequence and reconstruction, flasks containing pure samples of Perfluoro-Crown Ether (PFCE), PFOB and Perfluorooctane (PFO), respectively, were used. The samples were submersed into a larger flask containing (tap-) water in order to provide a more fluent susceptibility passage to the PFC volume. This preparations ensures minimized line broadening and anistropy effects and reduces the geometrical influence of both CSI and normal spectroscopy.

Furthermore, diluted PFOB emulsions of 1%, 5%,10% were prepared in Eppendorf tubes (*Eppendorf*, Hamburg, Germany) in order to study the small-signal response of the MRSI sequences.

In order to visualize the signal of a multi-resonant specimen, spectra were integrated over the major resonance complexes of the specimen in order to obtain *integral*, color-coded CSI images. Employing integration specifically to the resonance complexes is beneficial for avoiding noise in spectral regions without resonances.

3.6 k -sampling patterns

CSI methods make use of various sampling patterns. For SE-CSI, radial sampling schemes are common (e.g. [43]). Radial sampling tends to be less prone to image artifacts caused by an unsteady magnetization integrand in Equation (2.49). Many spatial modulations can be avoided in this way. The F-uTSI sampling pattern is of a *radial* kind. Each trajectory through the k -space samples N nearest (cartesian) k -space coordinates. Thus the term *pseudo-radial sampling*.

SSFP methods naturally feature constant magnetization and thus no modulation of the spatial coding integral. Artifacts can be thus regarded as non-sampling dependent and the sampling pattern can be chosen arbitrarily.

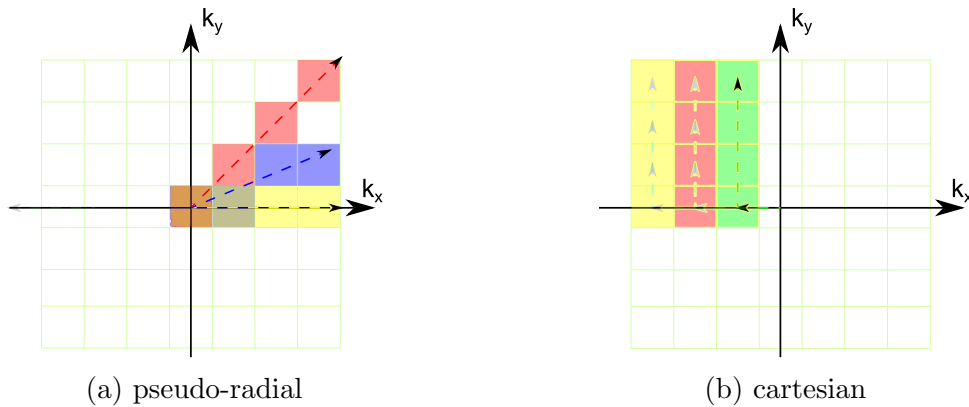


Figure 3.6: Illustration about the first three trajectories in the used sampling patterns.

3.7 Magnetic Resonance Imaging setup

3.7.1 Hardware

All MRI and CSI experiments were carried out on a *Philips Achieva Dual-Quasar*, 3T clinical MRI system (*Philips Medical Systems*, Best, The Netherlands). For detection of both ^{19}F and ^1H a dual tuned volume resonator (*RAPID Biomedical*, Rimpar, Germany) with a linearly polarized B_1 , an inner diameter of $d = 52\text{mm}$ and a resonator length of $l = 80\text{mm}$. While the standard transverse field is set to $B_1 = 50\mu\text{T}$, the maximally applicable is $B_1 = 580\mu\text{T}$. To test the applicability of surface coils, the B_1 -field was purposely set to small values, e.g. $B_1 = 20\mu\text{T}$. The separately tuned and matched channels both have transmit and receive capability.

3.7.2 Software

The used host software of the MRI system was release *3.2.1.0*. As in any clinical environment, the MRI-UI offers alteration of the major parameters of a pulse sequence. For convenience, the user GUI is held comparatively simple.

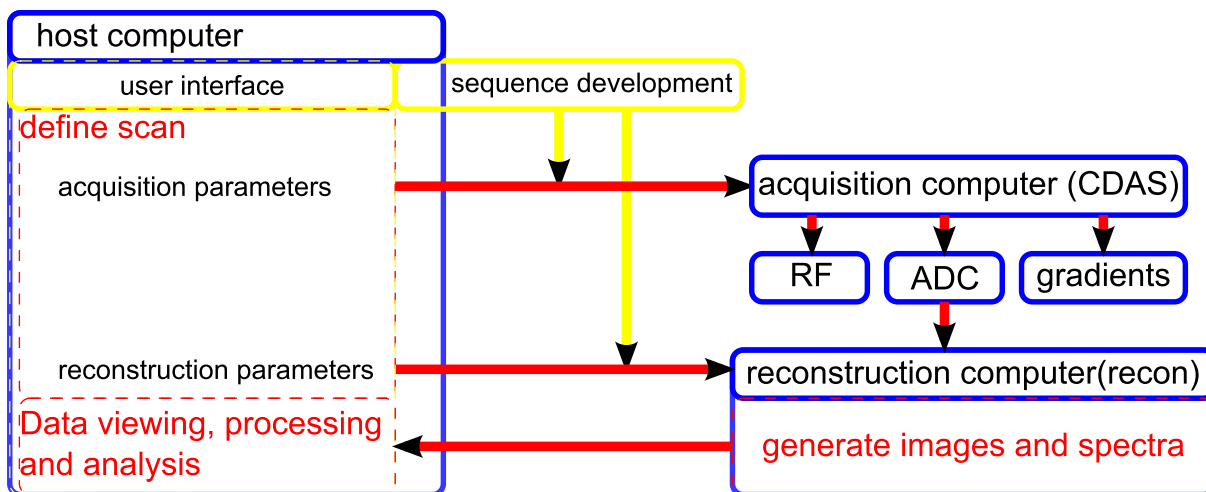


Figure 3.7: Flowchart with components comprising the MRI system

Figure 3.7 shows a pictorial description of the major elements of the used MRI system. The user interface is provided by default sending acquisition and reconstruction parameters to the respective terminals.

Although a fairly large amount of the actually available parameters can be changed in the user interface, the accessible settings proved to be too limited for the actual purposes. In order to enable thorough control of the experiment, *sequence development mode* is provided for the host application of research institutions. In the *sequence development mode*, sequence parameters and objects can be changed before transmission to the Data Acquisition System (DAS), where the sequence is translated into a runtime procedure.

As an example, the modification of an SSFP acquisition is described.

Parameterizing SSFP

The initial sequence settings are done via user interface, depicted in Figure 3.8. These settings are intended for established sequences with an intentionally limited set of variable parameters such as

- Scan geometry (*red* in Figure 3.8),
- basic pulse parameters (T_R , T_E , *purple*)
- sampling properties (*green*),
- coil selection (*yellow*) and

initial	geometry	contrast	motion	dyn/ang	p
Nucleus		F19			
Attenuator 19F		0			
Excitation Bandwidth (...)		0			
H1/F19 B1 ratio		1			
Read RF Shape		no			
Offset Frequency (Hz)		13621			
Coil selection		MC-Rapid-BM-MN			
FOV	FH (mm)	20			
	RL (mm)	20			
Voxel size	FH (mm)	2.5			
	RL (mm)	2.5			
RFOV direction		RL			
TE		user defined			
(ms)		5			
TR		shortest			
NSA		1			

(a) Initial settings

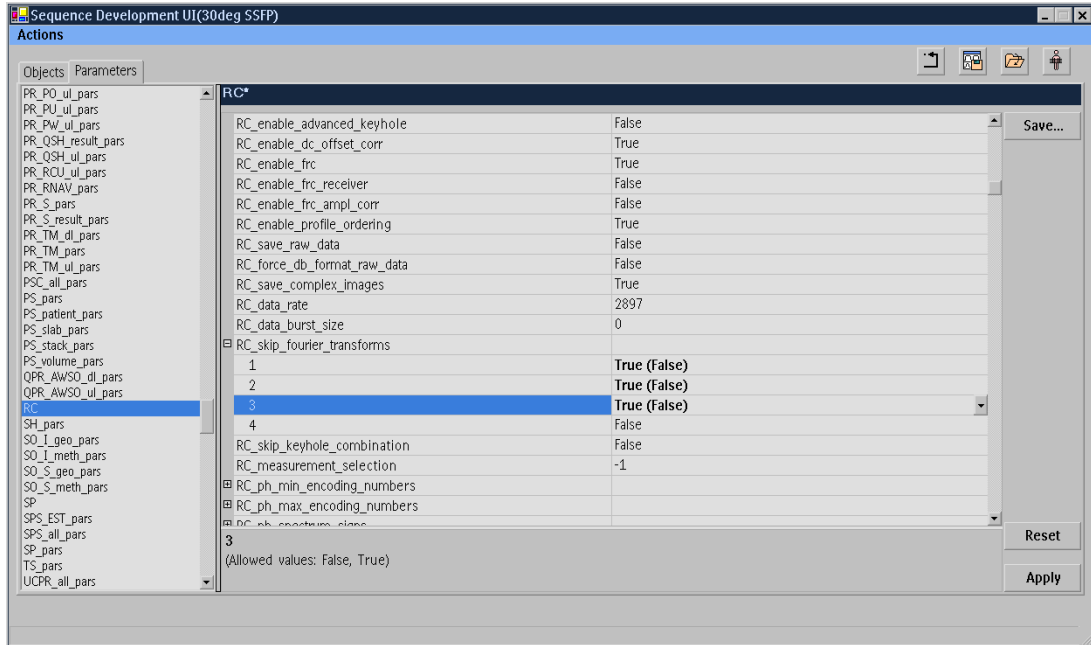
Nucleus	F19
Attenuator 19F	0
Excitation Bandwidth...	0
H1/F19 B1 ratio	1
Read RF Shape	no
Offset Frequency (Hz)	13621
Coil selection	MC-Rapid-BM-MN
Dual coil	no
Preparation coil	MC-Rapid-BM-1H
CLEAR	no
FOV	FH (mm) 20
	RL (mm) 20
Voxel size	FH (mm) 2.5
	RL (mm) 2.5
Recon voxel size (mm)	2.5
Samples	64
Spectral BW (Hz)	32000

(b) Geometric settings

Figure 3.8: Basic parameter settings in the user GUI. (a) lists the available *initial settings*, such as FOV, center frequency and major sequence timings. (b) depicts the *geometric settings*, in which also temporal sampling is parameterized.

- central frequency of pulsing and demodulation (*blue*).

As described above, LCSSFP-CSI require different phase-increment schemes. Both acquisition and pulse phase are to be changed in the same manner as depicted in Figures 3.9b and 3.9c. Since the user GUI does not support direct alteration, the changes are to be done in the *sequence development mode*. Additionally, *Fourier* transformation (Figure 3.9a) and spectral-spatial filtering (Figure 3.9e) are to be altered for various experiments. Furthermore, analysis of the SSFP responses require turned-off gradient modulation (Figure 3.9d). In order to modify the applied RF-power, the coil's maximum B_1 was constrained in the *System tuning* menu of the UI. Accordingly, this affects the pulse application time parameter. In low- B_1 regimes the pulse time occupies a significant time of the repetition time, which has to be modified accordingly, in order to accommodate the pulse.



(a) Overview sequence development mode. Case: DFT toggling

UMP_uTSI_ssf_rphase	
1	0
2	180 (0)
3	0
4	180 (0)

(b) RF phase

UMP_uTSI_ssf_aqphase	
1	0
2	180 (0)
3	0
4	180 (0)

(c) ACQ phase

gr_lenc1_factor_min	0
gr_lenc2_factor_max	0
gr_str_step	0.0000 (1.8375)
SQ_base : start_time -0.504 ms, end_time 6.5883 ms	
SY.trig_scope : start_time -0.497 ms	
RF.ex : start_time -0.0127 ms, dur.	
RF.echo : start_time 2.4776 ms, dur.	
GR.py : start_time 2.5129 ms, dur.	
GR.px : start_time 2.5129 ms, dur.	

(d) Disable gradient

RC_filter_types	
1	MGG_RC_FILTER_TYPE_NO_FILTER
2	MGG_RC_FILTER_TYPE_NO_FILTER
3	MGG_RC_FILTER_TYPE_COSINE1
4	MGG_RC_FILTER_TYPE_NO_FILTER

(e) Change filters

Figure 3.9: Parameterization of sequence objects in sequence development mode. (a-e) are scenarios sequence parameters alterations. These settings are not available in the common user UI.

3.8 CSI evaluation

Evaluations were performed using *MATLAB* (*The MathWorks*, Inc., Natick, MA., USA). After image acquisition, the CSI sets in *SPAR/SREC* format were exported from the MR database. Machine data was converted into *MATLAB* data-matrices using the datatype converter *freadVAXD()* (*The MathWorks*, Inc., Natick, MA., USA).

Scan parameters could be read out to a certain limit by parsing the *SPAR* parameter files using the *MATLAB*-function *readPhillipsSPAR()* (*Michael Kelm*, Heidelberg, Germany). The parameter set stored in these files is defined by the reconstructor module and comprises major sequence features such as timing, geometry and patient data.

3.8.1 SNR quantification

In order to quantify the SNR and SNR_t capability of the sequences, diluted PFOB-emulsions in concentrations of 1%, 5% and 10% in small amounts of $V \approx 0.2\text{ml}$ were prepared from a freeze-dried stock (see Section 3.5).

Acquisitions of small samples was performed using geometry parameters

- FOV: $40 \times 40\text{mm}$
- *matrix size*: 32×32
- *coronal projection* integrating over the length of the tubes

This geometry settings were reasonably set in order to stick to the requirements of a SE sequence to keep the echo train as short as possible due to the transverse signal loss. Finer resolutions require higher phase accumulations and thus a longer echo spacing with fixed gradient strengths. In order to quantify SNR, a measure which accounts for partial volume signal variation is needed since the phantom diameter ranges in pixel dimension. Contrarily, the background occupies a high ratio of the overall integral image. The provided SNR measure is thus SNR_{max}

$$\text{SNR}_{max} = \frac{S_{max}}{\sigma_{BG}} \quad (3.14)$$

where S_{max} is the maximal signal in an acquired image and σ_{BG} is the approximated standard deviation of the background, extracted from a section of air. Since *Rayleigh*-distributed absolute values are regarded, the *Gaussian* standard-deviation σ_{BG} has to be extracted from the variation of the background as[2]

$$\sigma_{BG} = \frac{\sqrt{Var(\|BG\|)}}{0.655} \quad (3.15)$$

with $Var(\|BG\|)$ being the estimated variance of the magnitude background. In order to avoid inclusion of spectral noise components not containing any signal, specimen were integrated in spectral sections according to the position of the specimens resonance complexes.

In order to evaluate the time-dependent SNR enhancement with multiple Number of Signals Averaged (NSA), a time frame of *20min* was set. Subsequently, the time-base was optimally filled with experiments of either LCSSFP and F-uTSI. The resulting SNR_{max} is an estimator of the sequence's ability to turn available measurement time into SNR, i.e. SNR_t .

3.8.2 Reconstruction

LCSSFP acquisitions were converted into a *MATLAB* data matrix. The recorded (\vec{k}, t) -spaces for each phase increment scheme (cf. Section 3.3) were then *linearly* combined and transformed to (\vec{x}, f) -space using *MATLAB*'s *nD-DFT* `fftn()`.

Digital filtering was turned off for all acquisitions in both spatial and temporal direction in order to rate the imaging performance in all dimensions.

3.8.3 k -space sampling

The used k -sampling patterns were described in Section 3.6. In order to compare the performance of the imaging aspect, sampling patterns were kept equal in both LCSSFP and F-uTSI. When unencoded and untransformed samples were evaluated, the respectively preferred sampling patterns for each sequences were used, i.e. *pseudo-radial* for F-uTSI and *cartesian* for SSFP.

3.8.4 spectral uniformity measures

In order to qualitatively rate the spatial distribution of the signal, the acquired high-concentration phantoms are magnified and pixelwisely overlaid with their spectral responses. Performance ratings were both based on

- spatial compactness and
- spectral uniqueness,

both facilitated by the magnified clip. Clipping and CSI overlay was performed using the proprietary *MATLAB* function *analyzeCSI()*.

3.8.5 Parameter dependency evaluation

To show the strong parameter dependency of SE-CSI methods, both the influence of echo spacing, offset pulsing and RF power was evaluated. Considering the expectedly relatively large parameter field, experiments were carried out in combinations of maximally two changing parameters. Generally, three main classes of experiments were carried out, i.e.

- NMR *spectroscopy*, using simple pulsing and consequent acquisition for the analysis of the principal spectral response
- NMR *spectroscopy*, comprising an additional refocussing pulse and sampling of the arising echo for investigations regarding pulse timing and offset frequency pulsing
- *Fast CSI*, using the described methods for the analysis of spatial features, artifacts and intensity dependent on offset frequency and RF power.

3.9 in-vivo acquisition and animal preparation

A single *in-vivo* acquisition was performed. The distribution of an ^{19}F -agent in a mouse (C57BL/6, $m = 20.7\text{g}$) was analyzed. The mouse was injected with $V = 0.25\text{ml}$ of a 30% PFOB-emulsion in egg-yolk phospholipids (particle diameter of 205nm). 24h before the image acquisition the agent was applied in the tail vein of the mouse, after and before an injection of $\approx 25\mu\text{l}$ physiologic saline solution (0.9% NaCl).

Anesthesia was induced with 3% and maintained with 1–2% isoflurane in medical air (flow $F = 0.4l/min$). During acquisition, the animal was supported by a heated animal bed. The local institutional animal care committee of the University of Maastricht approved all experimental procedures.

Due to the expectedly high noise floor and artifact level in the animal study, *windowing* was employed. The entire dynamic range was thus restricted to a certain lower limit. The remaining upper portion of the dynamic was scaled to the full range of the integrated CSI signal. The lower cut-off threshold was selected individually for the acquisitions in order to suppress apparent artifacts. Spurious signal was thus neglected as far as practicable.

3.10 Proprietary scripts and data

All used MRI data and *MATLAB* scripts for evaluation and simulation of the following results are provided on the attached *CD*.

4 Results

4.1 High resolution spectroscopy on multi-resonant PFOB and PFO

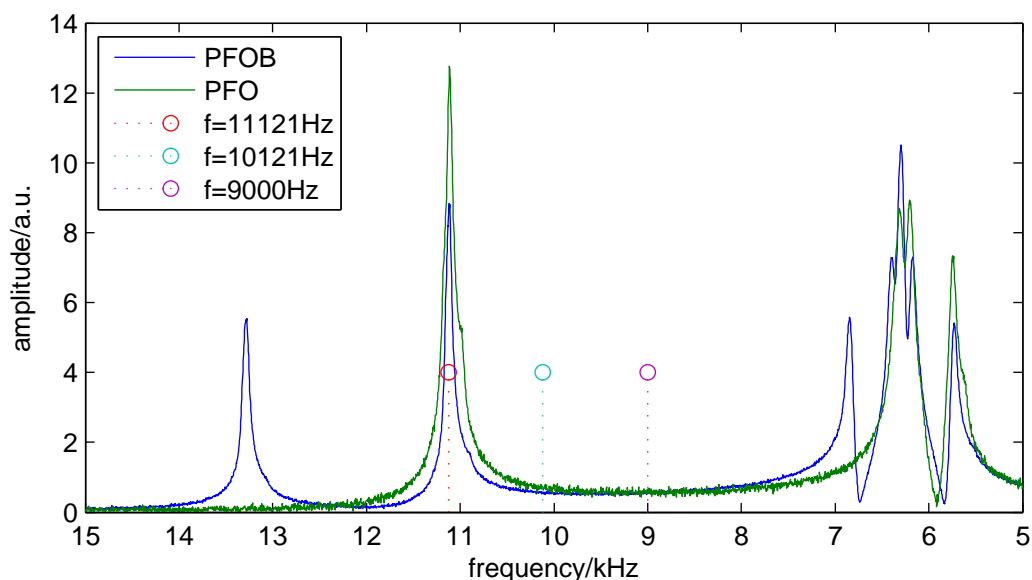


Figure 4.1: Clipped high-resolution NMR spectroscopy of PFOB and PFO at $3T$. Characteristic central frequencies are included as stem plots.

Pulse parameters: $\alpha = 22.5^\circ$ $f_c = 11121Hz$, $B_1 = 580\mu T$

Sampling parameters: $f_S = 32kHz$, $N_S = 8192$

Figure 4.1 depicts a high-resolution ($\Delta f = 4Hz$) NMR spectrum of PFOB and PFO. The main resonance complexes as discussed in the methodology are visible. The assignment of the resonance complexes in PFOB (CF_2^- , CF_3^- and CF_2Br -complexes) is confirmed by the PFO (CF_2^- and CF_3^- -complexes).

Additionally, the typical central frequencies of ^{19}F -CSI are indicated, with $f_c = 9000Hz$ in the center between CF_2 and CF_3 , $f_c = 10121Hz$ as PFCE's resonance line (not acquired here), and $f_c = 11121Hz$ as the CF_3 resonance of PFOB.

The spectrum was cut to show the relevant part of the 16kHz -wide spectrum, between 5kHz and 15kHz from the reference.

4.2 Parameter dependency of echo sequences

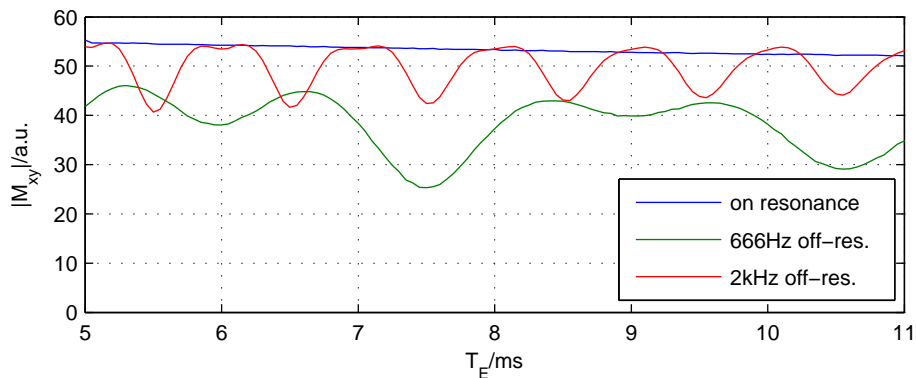


Figure 4.2: Response to a T_E parameter series for *uni-resonant* PFCE.

Pulse parameters: $B_1 = 50\mu\text{T}$, $T_E = 5, 5.05, \dots, 11\text{ms}$, $T_R = 4000\text{ms}$

Sampling parameters: $f_S = 32\text{kHz}$, $N_S = 64$

In order to show the dependency on the SE-interpulse delay, a series of differently spaced SE (90° - 180°) pulses are evaluated in Figure 4.2. The modulation with varying echo-time proportional to the offset frequency is to be noticed. The impact of the echo-time dependency on SE-imaging experiments is shown in the next paragraphs.

4.3 F-uTSI

Previous results and multi-echo simulations point to a very strong parameter dependency of a SE response to off-resonance pulsing. The effects of different parameters on both spatial and spectral response are pointed out subsequently.

4.3.1 Spatial modulations in off-resonance pulsing

Figure 4.3 depicts the spatial response of the F-uTSI sequence for different echo-times. The orthogonal *ghosts* and modulation around the central phantom signal over the spectrally integrated response of PFCE (off-resonance) are very pronounced in the acquisitions in

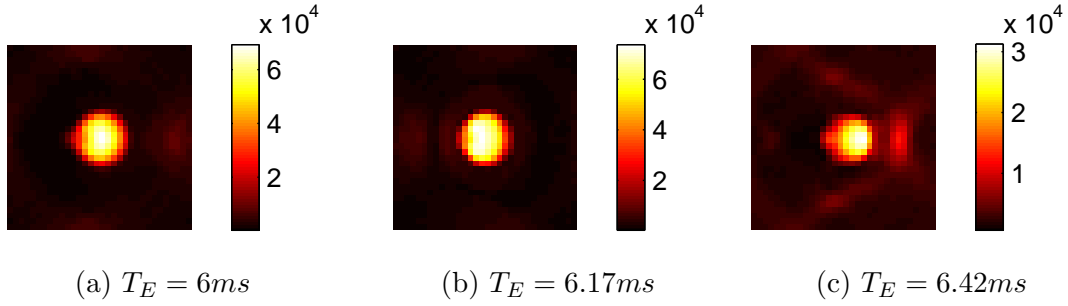


Figure 4.3: Spectrally integrated PFCE spatial responses for different echo times T_E of the F-uTSI sequence.

Pulse parameters: $B_1 = 50\mu T$, $ES = T_E$, $T_R = 2000ms$, $\Delta f = 2000Hz$

Sampling parameters: $f_S = 32kHz$, $N_S = 64$

Geometry: coronal projection $32x32$ in $40x40mm$, pseudo-radial sampling

Figure 4.3c. In Figures 4.3a and 4.3b the effect appears less. The artifacts differ greatly in amplitude and distance from phantom origin, depending on echo-time.

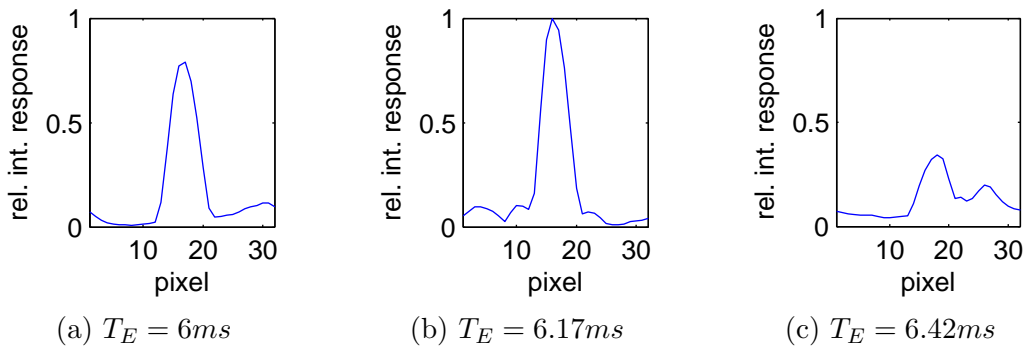


Figure 4.4: Horizontal profiles through the acquired integral image in Figure 4.3.

Pulse parameters: $B_1 = 50\mu T$, $ES = T_E$, $T_R = 2000ms$, $\Delta f = 2000Hz$

Sampling parameters: $f_S = 32kHz$, $N_S = 64$

Geometry: coronal projection $32x32$ in $40x40mm$, pseudo-radial sampling

Figure 4.4 shows horizontal profile of the images in Figure 4.3. The generated image artifacts in spatial domain and their dependency on echo time are clearly visible. The signal is normalized to the maximal signal i.e., $T_E = 6.17ms$ in Figure 4.4b. At $T_E = 6.42ms$, the artifact's magnitude reaches 50% of the phantom signal.

4.3.2 k -space modulations in off-resonance

Figure 4.5 shows the corresponding phase-encoded responses. In the same pattern as in Figure 4.3, modulations are present. However, in k -space, the modulations arise as

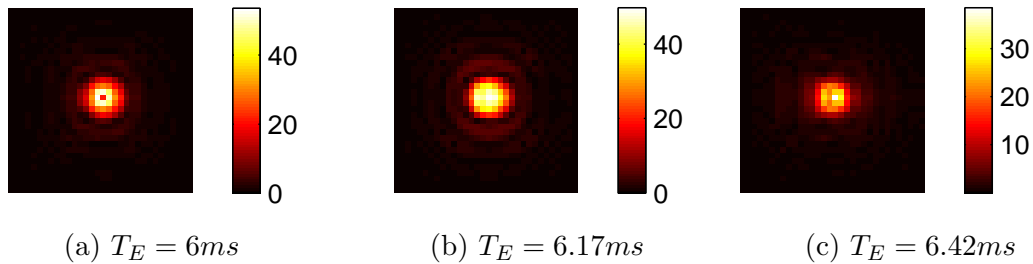


Figure 4.5: Integral PFCE response in encoded k -spaces of Figure 4.3

Pulse parameters: $B_1 = 50\mu T$, $T_E = ES = 6.42ms$, $T_R = 2s$, $\Delta f = 2000Hz$

Sampling parameters: $f_S = 32kHz$, $N_S = 64$

Geometry: coronal projection 32×32 in $40 \times 40mm$, *pseudo-radial* sampling

symmetric amplitude modulations. The radially oscillating modulations are visible best in Figures 4.5a and 4.5b.

4.3.3 k -space modulations without encoding gradients

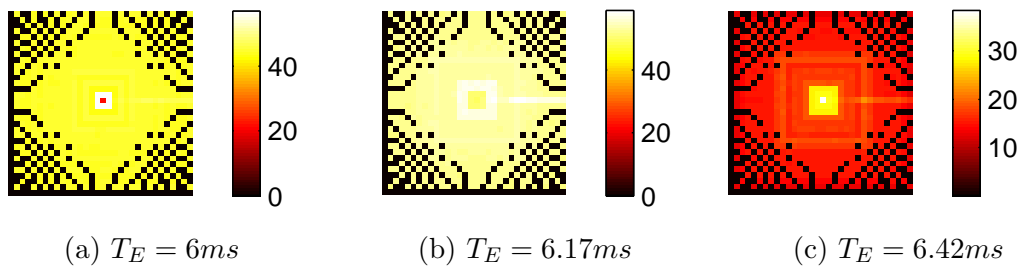


Figure 4.6: Integral PFCE response in *unmodulated* k -spaces of Figure 4.3

Pulse parameters: $B_1 = 50\mu T$, $T_E = ES = 6.42ms$, $T_R = 2000ms$, $\Delta f = 2000Hz$

Sampling parameters: $f_S = 32kHz$, $N_S = 64$

Geometry: coronal projection 32×32 in $40 \times 40mm$, *pseudo-radial* sampling

The acquired k -space responses of PFCE *without* spatial encoding is shown in Figure 4.6. For different echo times T_E , the response differs greatly, again showing previously observed oscillations and amplitude variations. Figure 4.6c exhibits a modulation far off-DC, while Figures 4.6a and 4.6b vary mostly around the k -space origin.

Clearly visible are the unfilled k -coordinates near the margin of the k -space. This is due to the limited amount of trajectories of the *pseudo-radial* sampling pattern. The trajectories have lower sampling densities in the outer regions which manifests itself in sparse corners of k -space, while the center of k -space is oversampled.

4.3.4 Simulated CPMG response

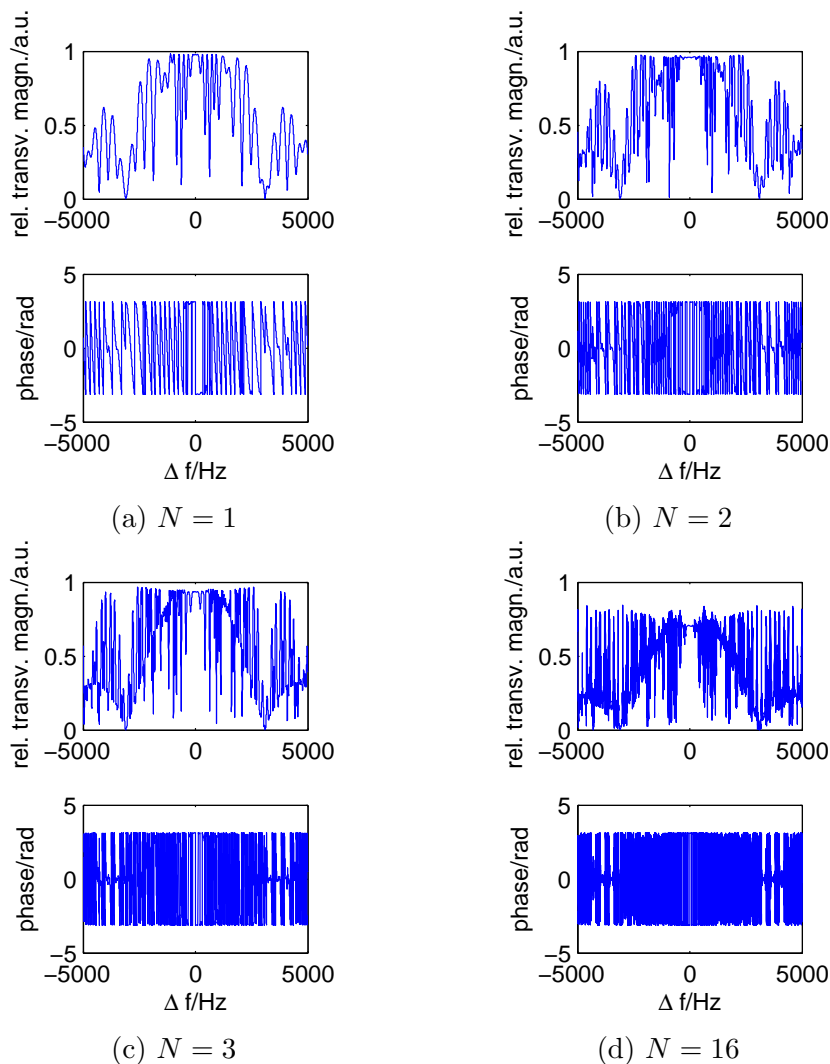


Figure 4.7: Simulated amplitude and phase responses to a F-uTSI echo train. The relative spectral magnetizations after the refocusing in acquisition periods 1,2,3 and 16. Sequence parameters $ES = 5ms$, $B_1 = 20\mu T$, $\gamma = 40.055MHz/T$, $B_0 = 3T$, $T_1 = 1s$, $T_2 = 0.2s$

As can be seen in Figure 4.7, the CPMG pulse sequence in a simulated scenario shows strong spectral variation. In a small area around $\Delta f = 0$, a fully refocused magnetization can be expected, solely dependent on relaxation. At larger off-resonance frequencies, responses vary strongly from echo to echo, both in *amplitude* and *phase*. Additionally, the first-minimum caused by the excitation pulse (derived in Equation (2.38)) at around $\Delta f = 3kHz$ is preserved.

Despite the strong frequency-dependency of the CPMG, theory suggests the approach of

a general steady state of the amplitude with $1/T_R$ -periodicity. Accordingly, *echo-skipped* F-uTSI acquisitions were performed, which are shown in the following.

4.3.5 Echo skipping on uni-resonant PFCE

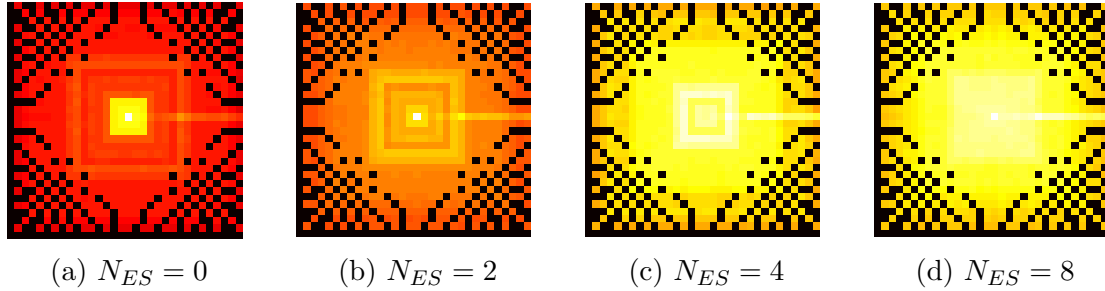


Figure 4.8: off-resonance (uncoded) k -spaces with different amount of skipped echoes N_{ES} . Colormap referenced to (a).

Pulse parameters: $B_1 = 50\mu T$, $T_E = ES = 6.42ms$, $T_R = 2s$, $\Delta f = 2000Hz$

Sampling parameters: $f_S = 32kHz$, $N_S = 64$

Geometry: coronal projection 32×32 in $40 \times 40mm$, *pseudo-radial* sampling

Figure 4.8 shows non-gradient encoded k -spaces for an off-resonance PFCE response. The sequence depicted in Figure 3.3 was used. Modulations of the k -response show oscillations, depending on the amount of *skipped echoes* N_{ES} at the beginning of each echo train. The colormap is referenced to the acquisition without any skipped echoes since it yields the highest maximum. k -space variations within the echo train are attenuated with increasing number of omitted echoes. At the same time, the overall signal amplitude decreases.

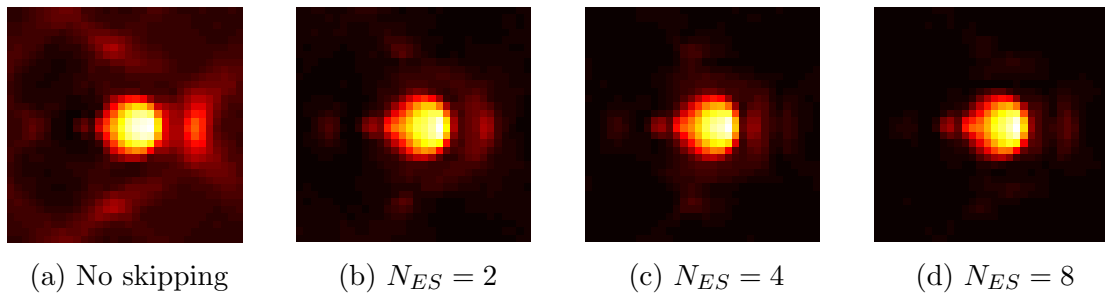


Figure 4.9: off-resonance spatial responses with different echo-skipping N_{ES} .

Pulse parameters: $B_1 = 50\mu T$, $T_E = ES = 6.42ms$, $T_R = 2s$, $\Delta f = 2000Hz$

Sampling parameters: $f_S = 32kHz$, $N_S = 64$

Geometry: coronal projection 32×32 in $40 \times 40mm$, *pseudo-radial* sampling

Figure 4.9 depicts the correspondent spatial transformations of the k -space data from Figure 4.8. The results of k -space modulation is visible very well in a, where orthogonal

ghosting appears. Colormaps are calculated for each acquisition *individually*. The signals are thus to be rated *qualitatively*. Increasing numbers of skipped echoes N_{ES} reduces the relative amount of spurious signal in k -space, but also the signal itself.

Again taking horizontal profiles from the phantom acquisitions, the modulated ghost images appear in a significant amplitude range as can be seen from Figure 4.10. All profiles are referenced to the maximal spatial amplitude yield without echo skipping (Figure 4.10).

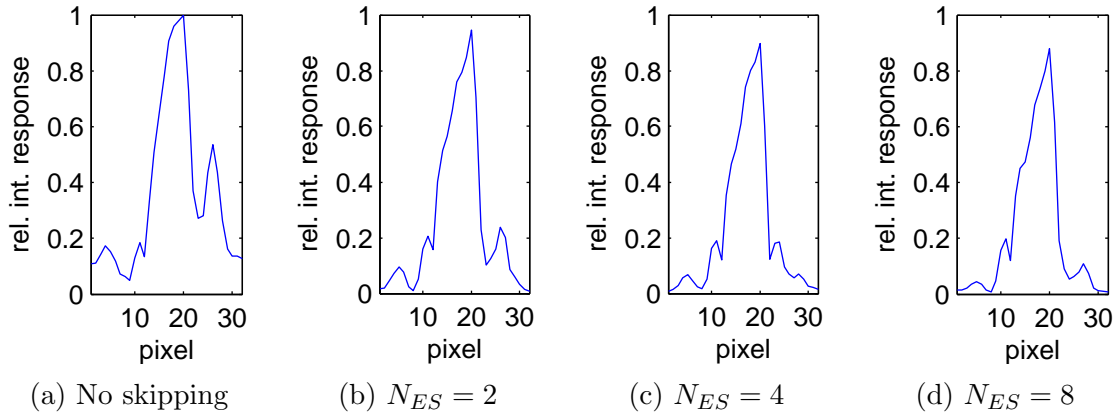


Figure 4.10: off-resonance spatial response profiles for different echo-skipping N_{ES} .

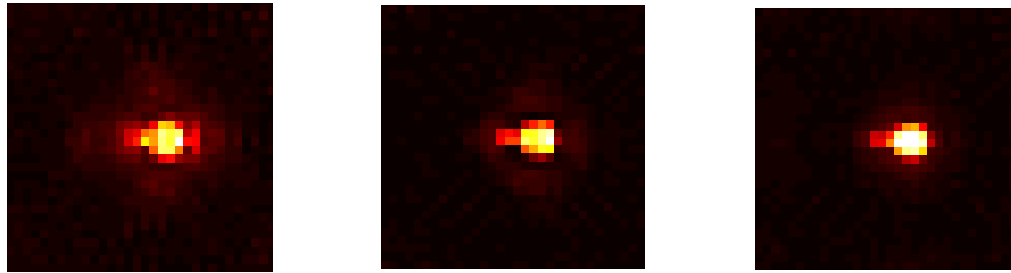
Pulse parameters: $B_1 = 50\mu T$, $T_E = ES = 6.42ms$, $T_R = 2s$, $\Delta f = 2000Hz$

Sampling parameters: $f_S = 32kHz$, $N_S = 64$

Geometry: coronal projection 32×32 in $40 \times 40mm$, *pseudo-radial* sampling

The ghosting signal represents up to 50% of the signal of the proper phantom response. Whereas the right ghost appears at a position of around $25px$, the left (symetric) ghost is hidden under a spatially weaker phantom signal. As the amount of skipped echoes increases the spurious signals again decrease significantly. The actual signal intensity is affected less.

4.3.6 Echo skipping on multi-resonant PFOB



(a) CF_2Br : $-6000 < f < -3000$ (b) CF_3 : $-2500 < f < 500$ (c) $6 \times \text{CF}_2$: $1500 < f < 5000$

Figure 4.11: Separated PFOB-responses at $f \approx -4500\text{Hz}$ (CF_2Br), $f \approx -1700\text{Hz}$ (CF_3) and $f \approx 2500\text{Hz}$ (CF_2) without skipping echoes.

Pulse parameters: $B_1 = 50\mu\text{T}$, $T_E = ES = 5\text{ms}$, $T_R = 1000\text{ms}$, $f_c = 9000\text{Hz}$

Sampling parameters: $f_S = 32\text{kHz}$, $N_S = 64$

Geometry: coronal projection 32×32 in $80 \times 80\text{mm}$, pseudo-radial sampling

In Figure 4.11 the F-uTSI response to a multi-resonant species (PFOB) is shown. The responses are integrated ranges over the single resonances for the CF_2Br and the CF_3 , the 6 CF_2 groups are integrated into one range. The ghost images occur irregularly, depending on the frequency of the regarded resonance with respect to the center frequency.

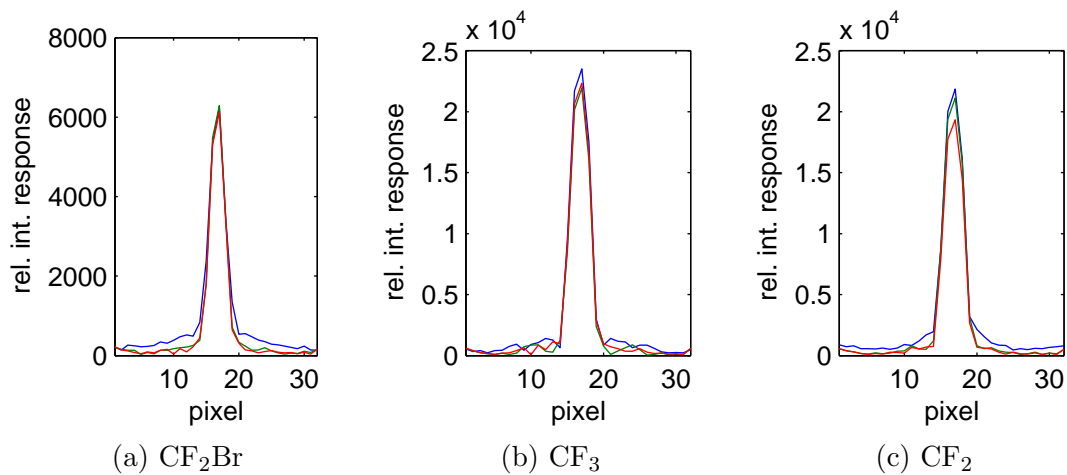


Figure 4.12: Spatial profiles of PFOB-responses (CF_2Br , CF_3 , CF_2). Skipped echo parameters: *blue:* $N_{ES} = 0$, *green:* $N_{ES} = 4$, *red:* $N_{ES} = 8$

Pulse parameters: $B_1 = 50\mu\text{T}$, $T_E = ES = 5\text{ms}$, $T_R = 1000\text{ms}$, $f_c = 9000\text{Hz}$

Sampling parameters: $f_S = 32\text{kHz}$, $N_S = 64$

Geometry: coronal projection 32×32 in $80 \times 80\text{mm}$, pseudo-radial sampling

In Figure 4.12 vertical profiles were again extracted. The oscillations are differently pro-

nounced for the selected resonance complexes. Also the effect of skipped echoes varied: While the signal maxima in Figures 4.12a and 4.12b are comparable in the different parameter settings, Figure 4.12c shows a significant decrease in signal when setting $N_{ES} = 8$. The PSF appeared more compact in all cases of echo skipping.

4.3.7 Cartesian sampling on multi-resonant PFOB

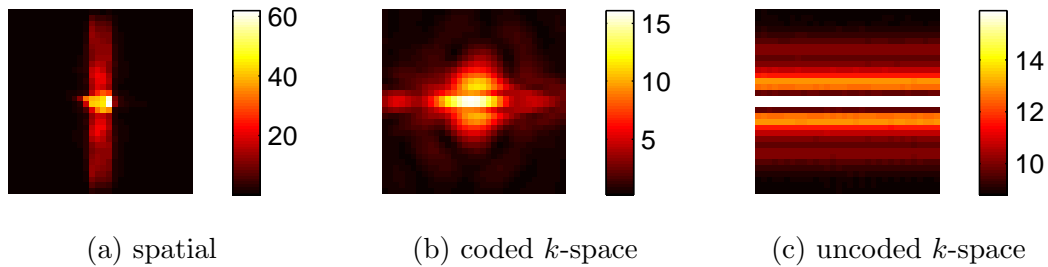


Figure 4.13: PFOB response with F-uTSI sequence employing cartesian sampling in spatial domain (a), encoded (b) and uncoded (c) k -space. All resonances integrated in one image.

Pulse parameters: $B_1 = 50\mu T$, $T_E = ES = 5ms$, $T_R = 1500ms$, $f_c = 10121$

Sampling parameters: $f_S = 32kHz$, $N_S = 64$

Geometry: coronal projection 32×32 in $80 \times 80mm$, cartesian sampling

Cartesian sampling with the F-uTSI pulse sequence is depicted in Figure 4.13. In spatial domain, the spectrally integrated image shows striking artifacts in one preferred direction along the principal y -axis, as shown in Figure 4.13a, spreading from the original phantom position.

Figure 4.13b shows the corresponding k -space. The horizontal slice with high intensity in k -space transforms to the spatially vertical smearing in Figure 4.13. Even more clearly, the background of spatial ghosting can be seen in the uncoded k -space, Figure 4.13c. The signal proves to be symmetric along the horizontal center line, but highly oscillating, particularly in the beginning of the echo train.

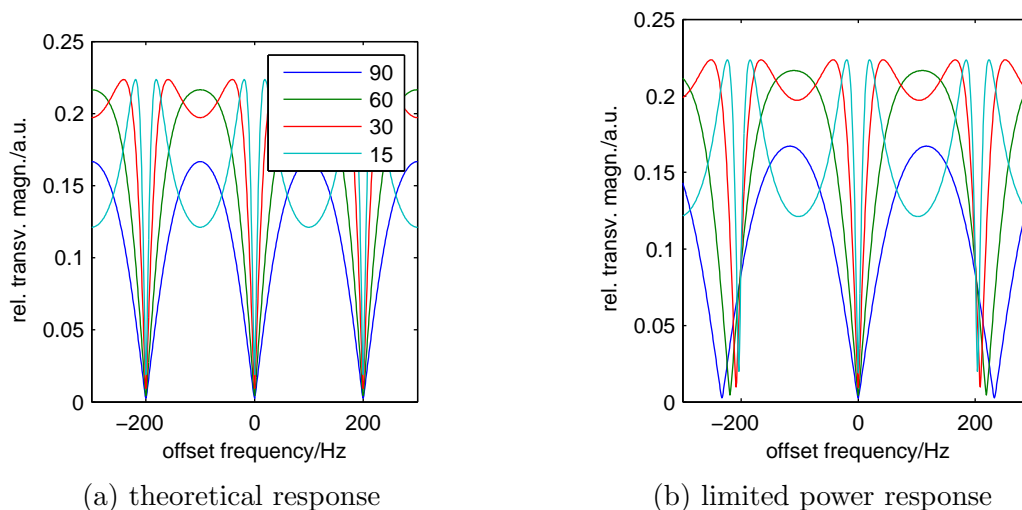


Figure 4.14: Simulated steady state spectral response $M_{SS}(f)$ for an ideal pulsing experiment (a) and non-ideal $B_1 = 20\mu T$ pulses (b). Simulated flip angles of $\alpha = 90^\circ, 60^\circ, 30^\circ$ and 15° (see legend)

Simulation parameters: $T_R = 5ms$, $\gamma = 40.055MHz/T$, $B_0 = 3T$, $T_1 = 1s$, $T_2 = 0.2s$

4.4 Simulated SSFP response

4.4.1 Small-band results

Figure 4.14 shows the spectral response of an SSFP sequence. The theoretical response depicted in Figure 4.14a is well known and describes the dip causing the banding artifacts in MRI. Figure 4.14b, on the other hand reveals the behaviour of limited power pulses. While the principal shape stays comparable, the dips are slightly shifted.

Accordingly, the passband-repetition in real pulsing is solely determined by the inverse of the actual precession interval. Keeping the interpulse-delay T_R , high- α pulses occupy comparatively more time of the T_R period, restricting the period of free precession. Thus, passbands of high- α SSFP pulse sequences are broader and repeated less frequent in the spectrum. Similarly the stop bands get broadened by the same effect.

4.4.2 Broadband response

The theoretical SSFP response continues its periodic variations with band-spacings of approximately $1/T_R$ in a wide-band simulation. However, as expected, non-ideal pulsing

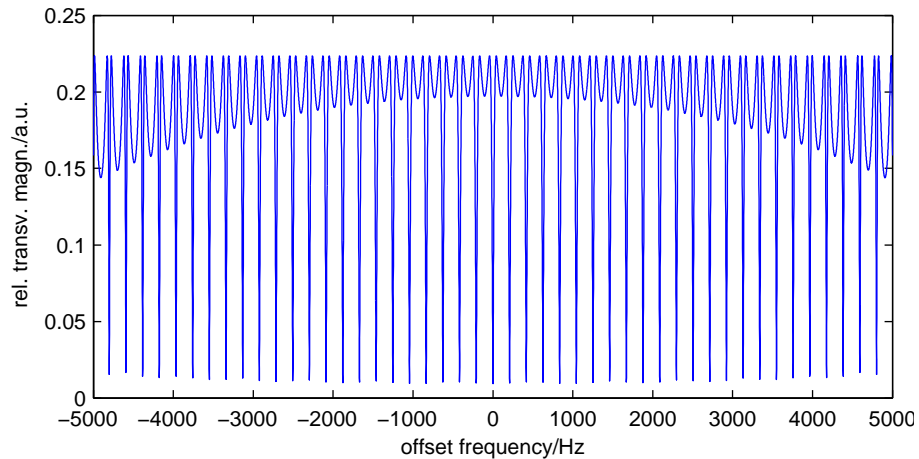


Figure 4.15: Simulated broadband SSFP response $M_{SS}(f)$ for non-ideal $B_1 = 20\mu T$ pulses. A flip angles of $\alpha = 30^\circ$ was simulated.

Simulation parameters: $T_R = 5ms$, $\gamma = 40.055MHz/T$, $B_0 = 3T$, $T_1 = 1s$, $T_2 = 0.2s$

shows further off-resonance effects which are shown in Figure 4.15. An additional modulation over frequency is shown very clearly in form of an increasing dip in the middle of the passband. The envelope of the lower dip mimics the first passband for a 30° excitation pulse.

4.5 LCSSFP-CSI

According to simulations, SSFP methods are less prone to off-resonance modulations than SE methods (e.g. F-uTSI). The LCSSFP performance is herein evaluated.

4.5.1 Simulated responses for phase-incremented pulses

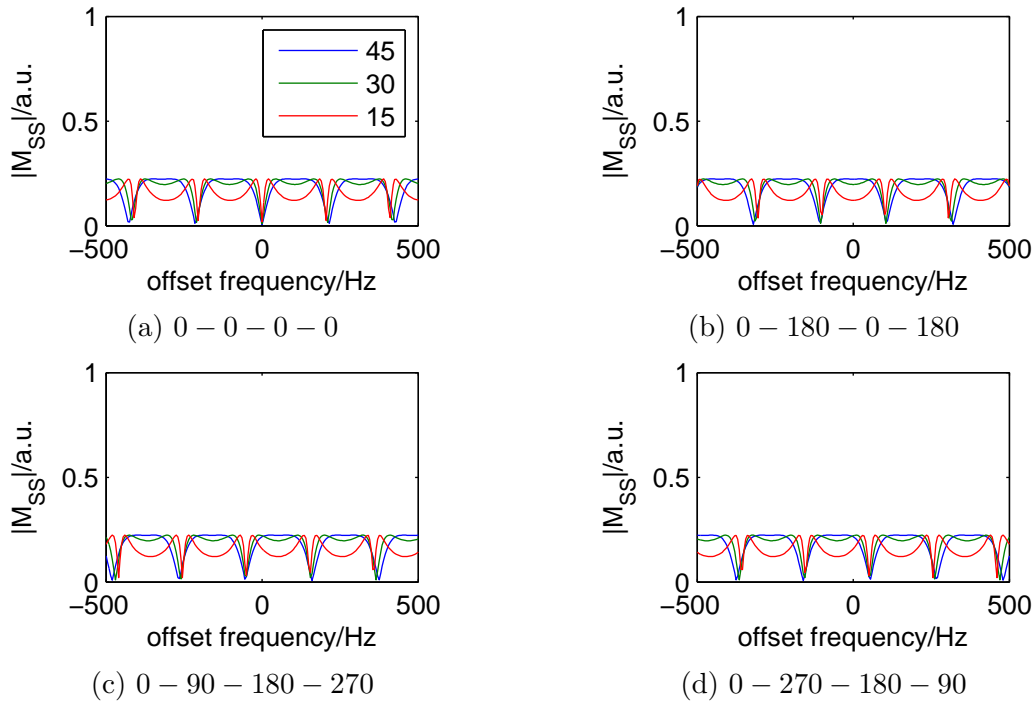


Figure 4.16: Steady state spectral response $M_{SS}(f)$ for different phase cycle schemes. Flip angles of $\alpha = 45^\circ$, 30° and 15° (see legend) were simulated.

Simulation parameters: $T_R = 5ms$, $\gamma = 40.055MHz/T$, $B_0 = 3T$, $T_1 = 1s$, $T_2 = 0.2s$, $B_1 = 20\mu T$

The spectral responses of SSFP pulse sequences with different phase cycle schemes are depicted in Figure 4.16. Clearly, the spectral response is shifted, along with the phase cycling. Simulated phase increments of $0^\circ, 180^\circ, 90^\circ$ and 270° are shown in Figure 4.16a, b, c and d, respectively. Along with the phase increment of πk , the spectral response is shifted in frequencies about $k/2T_R$.

4.5.2 Linearly combined simulations responses

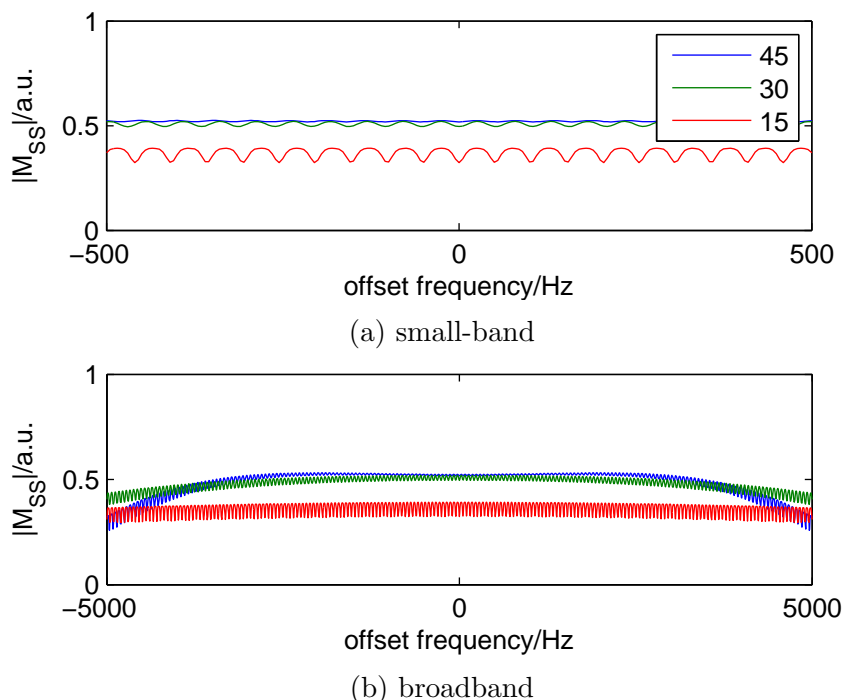


Figure 4.17: Simulated, linearly combined phase-cycled steady state spectral responses $M_{SS}(f)$ in near resonance (a) and for broader bands (b). Flip angles of $\alpha = 45^\circ$, 30° and 15° (see legend) were simulated.

$$T_R = 5ms, \gamma = 40.055MHz/T, B_0 = 3T, \mathbf{T}_1 = 1s, \mathbf{T}_2 = 0.2s, B_1 = 20\mu T$$

By linear combination of the responses from different phase-cycling schemes, a resultant response exhibiting minor modulations over frequency can be obtained which is depicted in Figure 4.17, for both near-center and broadband. While the envelope of the spectral response is determined by the bandwidth of the used pulse, the oscillations superimposed on the envelope is a function of T_1 and T_2 (for a set flip angle/ T_R -combination).

From a simulations point of view the amplitude of long- T_1 specimen (such as PFC) in the rapid pulsing experiment is mainly T_2 dependent which is underpinned in Figure 4.18, showing a scaled response in comparison to Figure 4.17.

The difference in spectral response compared to a *common* SSFP using solely one phase increment is apparent: instead of exhibiting highly variable pass- to stop-band transitions, the frequency components are fairly constant within a certain range dependent of the relaxation characteristics of the specimen.

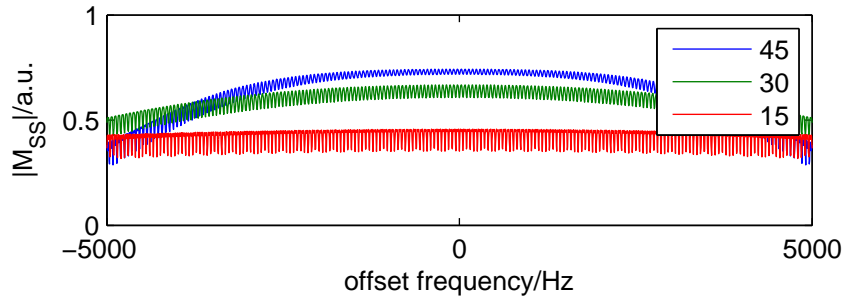


Figure 4.18: Simulated LCSSFP response for different pulse durations. Flip angles: see legend. $T_R = 5ms$, $\gamma = 40.055MHz/T$, $B_0 = 3T$, $T_1 = 1.3s$, $T_2 = 0.5s$, $B_1 = 20\mu T$

4.5.3 k -space response on multi-resonant PFOB

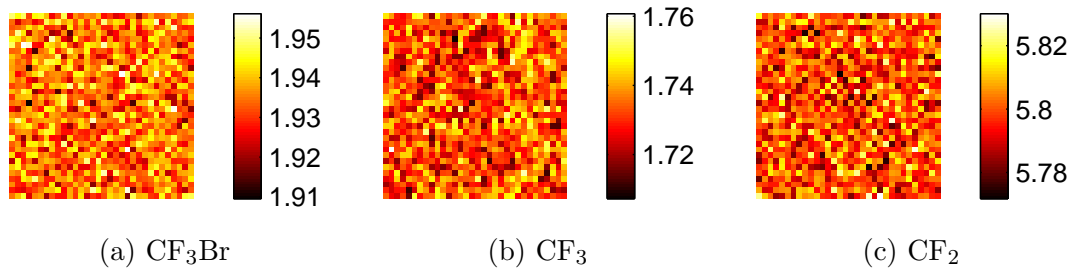


Figure 4.19: uncoded k -spaces for a 0° increment SSFP.

Pulse parameters: $B_1 = 50\mu T$, $T_E = T_R = 5ms$, $\alpha = 30^\circ$, $f_0 = 9000Hz$

Sampling parameters: $f_S = 32kHz$, $N_S = 64$

Geometry: coronal projection 32×32 in $80 \times 80mm$, cartesian sampling

Figure 4.19 shows the k -space response to an unencoded SSFP on multi-resonant PFOB. The spectral responses are separately integrated. The used center frequency was set between CF_2 and CF_3 . The integrated response over every resonance complex is stable without any signs of interference, also a homogenous noise level is observed. Unlike F-uTSI, the SSFP methods can thus make use of cartesian sampling for CSI (cf. Section 3.6). As can be seen by comparison of Figure 4.19 and Figure 4.6, k -space is completely filled, without sparse regions. Artifacts as in the cartesian-sampled F-uTSI are thus not present.

4.5.4 spectral response on multi-resonant PFOB

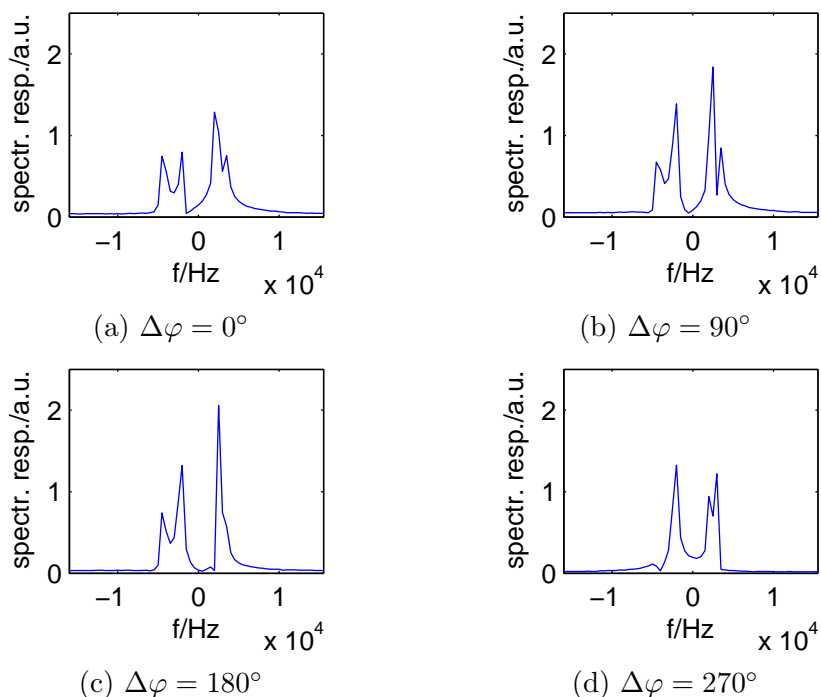


Figure 4.20: Spectral responses for differently phase incremented SSFP pulse sequences on PFOB, extracted from an unencoded k -space, e.g. Figure 4.19.

Pulse parameters: $B_1 = 50\mu T$, $T_E = T_R = 5ms$, $\alpha = 30^\circ$, $f_0 = 9000Hz$

Sampling parameters: $f_S = 32kHz$, $N_S = 64$

Geometry: coronal projection 32×32 in $80 \times 80mm$, cartesian sampling

Figure 4.20 depicts the spectral responses of PFOB to SSFP sequences with different phase increments. The k -space-extracted amplitude spectra show significant changes in each response, anticipated by the preceding simulation outcomes.

4.5.5 Linear combination of SSFP responses

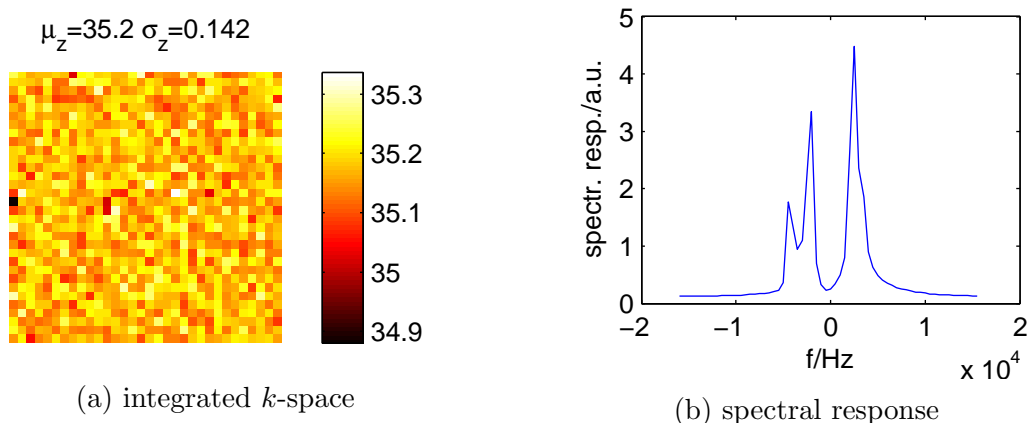


Figure 4.21: Linearly combined (non-encoded) SSFP responses in integrated k -space (a) and spectrum (b).

Pulse parameters: $B_1 = 50\mu T$, $T_E = T_R = 5ms$, $\alpha = 30^\circ$, $f_0 = 9000Hz$

Sampling parameters: $f_S = 32kHz$, $N_S = 64$

Geometry: coronal projection 32×32 in $80 \times 80mm$, cartesian sampling

Complex summation of the single SSFP responses obtained from the different pulse phase increments (Figure 4.20) yields a new (non-gradient encoded) k -space shown in Figure 4.21a. Each k -element of this uncoded k -space appears as Figure 4.21b.

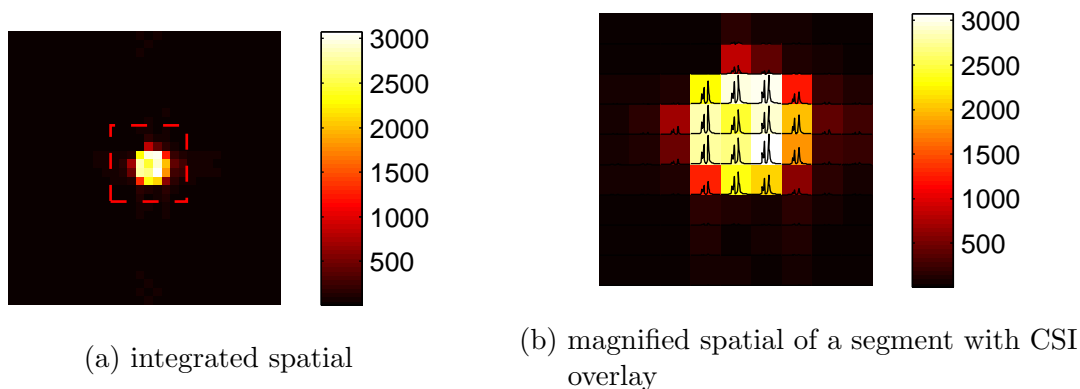


Figure 4.22: Integrated spatial LCSSFP response of PFOB (a) and its magnified view (b).

Pulse parameters: $B_1 = 50\mu T$, $T_E = T_R = 5ms$, $\alpha = 30^\circ$, $f_0 = 9000Hz$

Sampling parameters: $f_S = 32kHz$, $N_S = 64$

Geometry: coronal projection 32×32 in $80 \times 80mm$, cartesian sampling

Figure 4.22 shows the linearly combined response to differently phase-incremented SSFP pulse sequences. Image artifacts are not visible in the LCSSFP, the same is true for the single SSFP acquisitions (not shown).

4.6 Benchmarking F-uTSI and LCSSFP

Previous work has already shown that the SNR of the F-uTSI sequence strongly depends on the T_R [21]. Subsequently, the two sequences are compared, showing results for their performance in terms of SNR, SNR_t , spatial response and stability.

4.6.1 Detectability of a PFOB dilution series

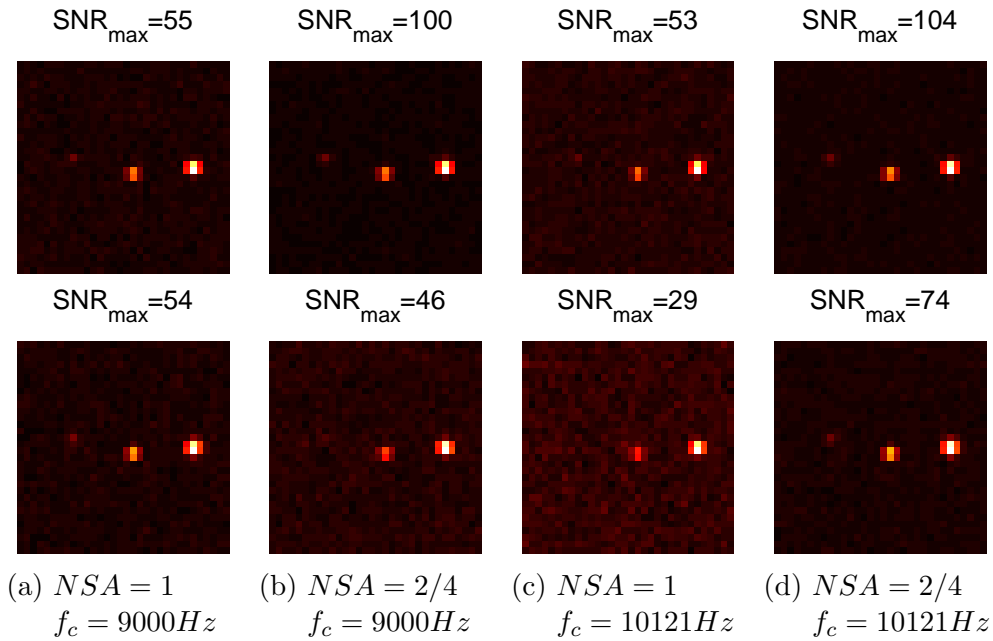


Figure 4.23: CSI sequence comparison in a dilution series of 1%, 5% and 10%. Top row: LCSSFP, bottom row: F-uTSI. Averaging using $NSA = 2$ for F-uTSI and $NSA = 4$ for LCSSFP, acquisition time for LCSSFP and F-uTSI are comparable.

Pulse parameters: $B_1 = 50\mu T$, $T_E = T_{R,SSFP} = 6ms$, $T_{R,FuTSI} = 1s$,

Sampling parameters: $f_S = 32kHz$, $N_S = 64$, $\alpha_{SSFP} = 22.5^\circ$,

Geometry: coronal projection 32×32 in $40 \times 40mm$

Figure 4.23 compares the detectability of PFOB in comparable F-uTSI and LCSSFP experiments, using the same scan time of 2 minutes for each measurement. An emulsion dilution series containing 10%, 5% and 1% was evaluated. While in LCSSFP acquisitions, every sample of the dilution series is identifiable, F-uTSI fails to significantly show the 1% sample. While averaging in LCSSFP brings noise reduction and signal enhancement, respectively, the F-uTSI response does not show a clear enhancement at $f_c = 9000Hz$. The signal of the 1% sample vanishes in the noise floor. LCSSFP shows a consistent

averaging performance, yielding double SNR_{max} for $NSA = 4$ independent of the center frequency.

4.6.2 SNR_t

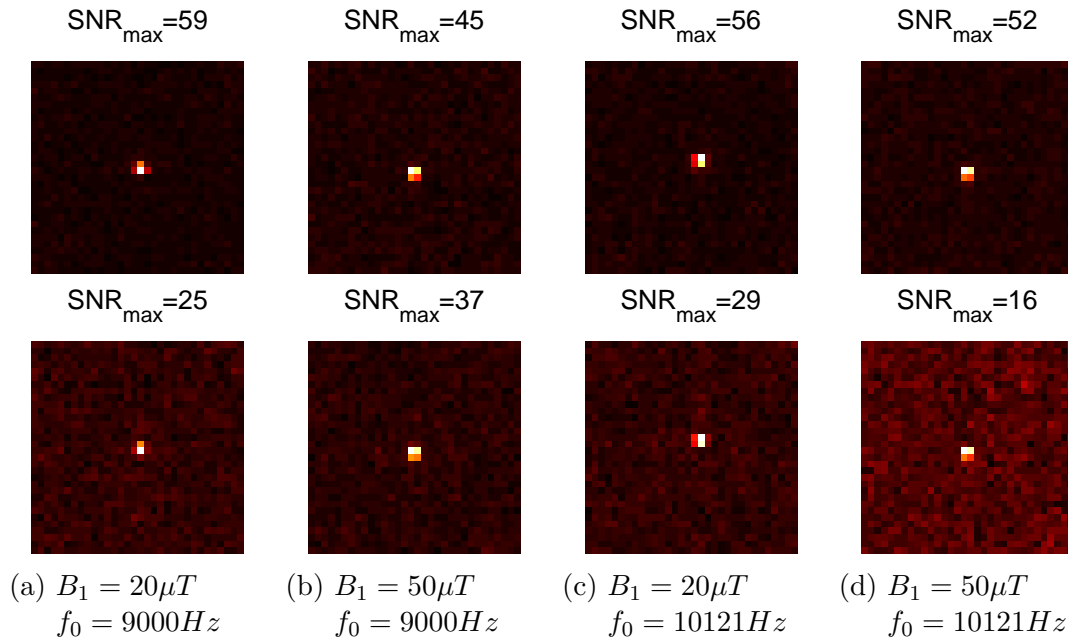


Figure 4.24: High-average 20min-acquisition for LCSSFP (top row, $NSA = 50$) and F-uTSI (bottom row, $NSA = 13$) for different B_1 fields and center frequencies f_0 on a PFOB sample.

Pulse parameters: $T_E = T_{R,SSFP} = 6ms@B_1 = 50\mu T/6.11ms@B_1 = 20\mu T$,

$T_{R,FuTSI} = 1.5s$,

Sampling parameters: $f_S = 32kHz$, $N_S = 64$, $\alpha_{SSFP} = 45^\circ$,

Geometry: coronal projection $32x32$ in $40x40mm$

The behaviour of the two sequences in a high-NSA regime, based on a comparable acquisition time is shown in Figure 4.24. Variations over center-frequency show the response's f_0 -dependency. In terms of SNR_t , LCSSFP yields comparable behaviour. The noise floor in F-uTSI acquisitions is generally higher in a comparable acquisition time.

4.6.3 Spectral uniformity

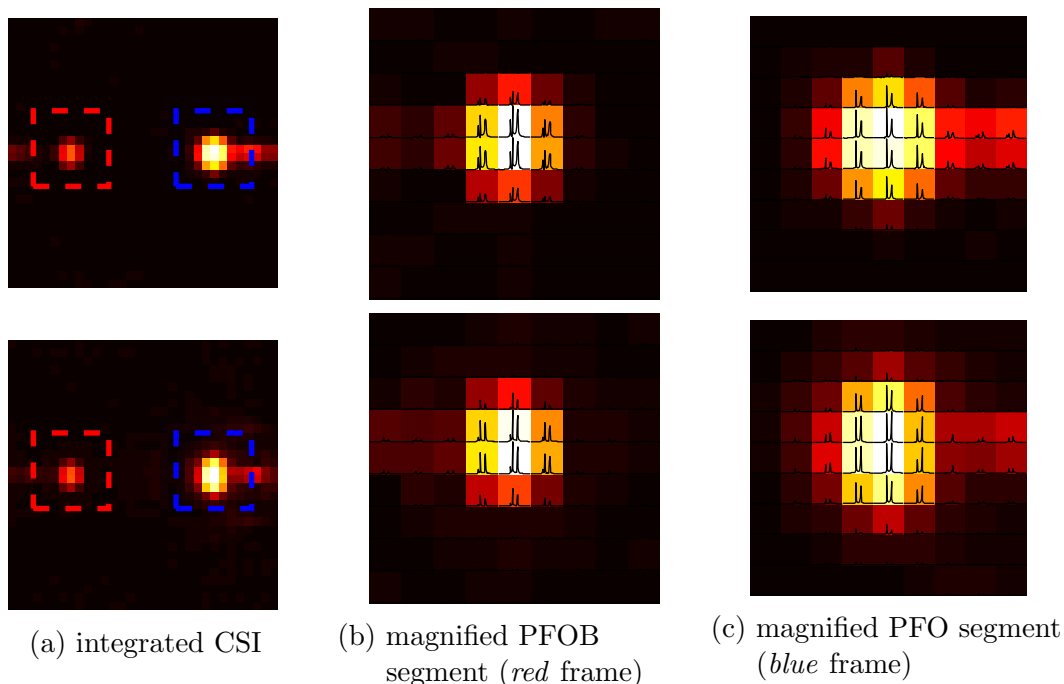


Figure 4.25: Comparison of both PFOB (red frame) and PFO (blue frame) F-uTSI (bottom) and LCSSFP (top)

Pulse parameters: $B_1 = 50\mu T$, $T_E = T_{R,SSFP} = 5ms$, $T_{R,FuTSI} = 1.5s$, $f_c = 9000Hz$

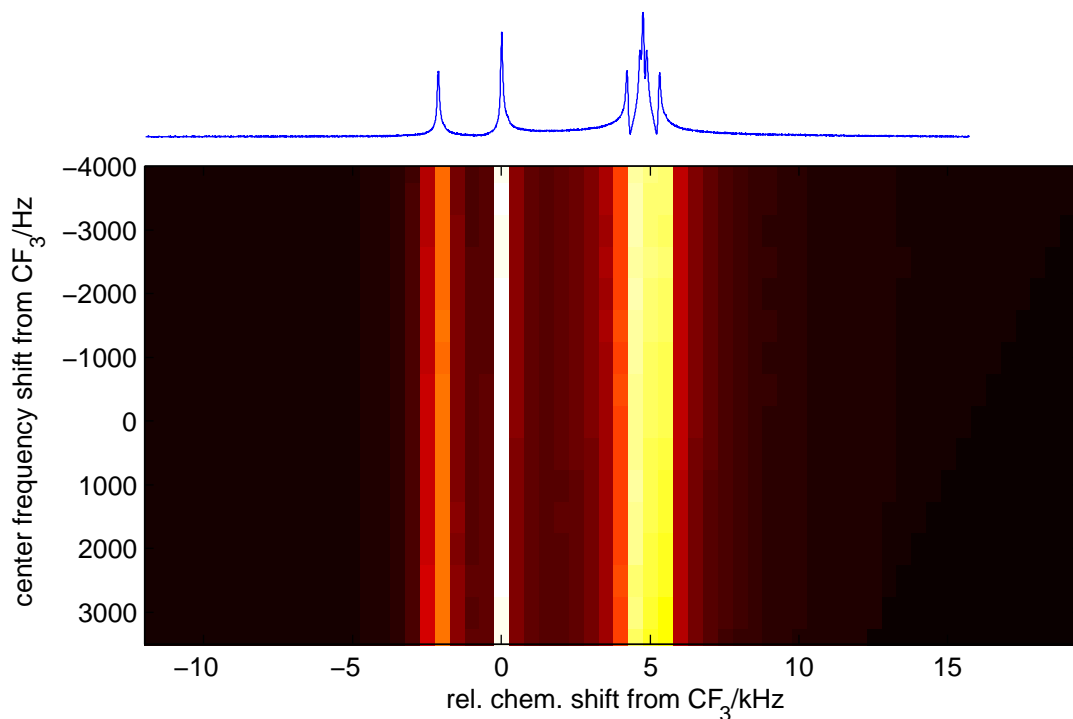
Sampling parameters: $f_S = 32kHz$, $N_S = 64$, $\alpha_{SSFP} = 15^\circ$,

Geometry: coronal projection 32×32 in $80 \times 80mm$

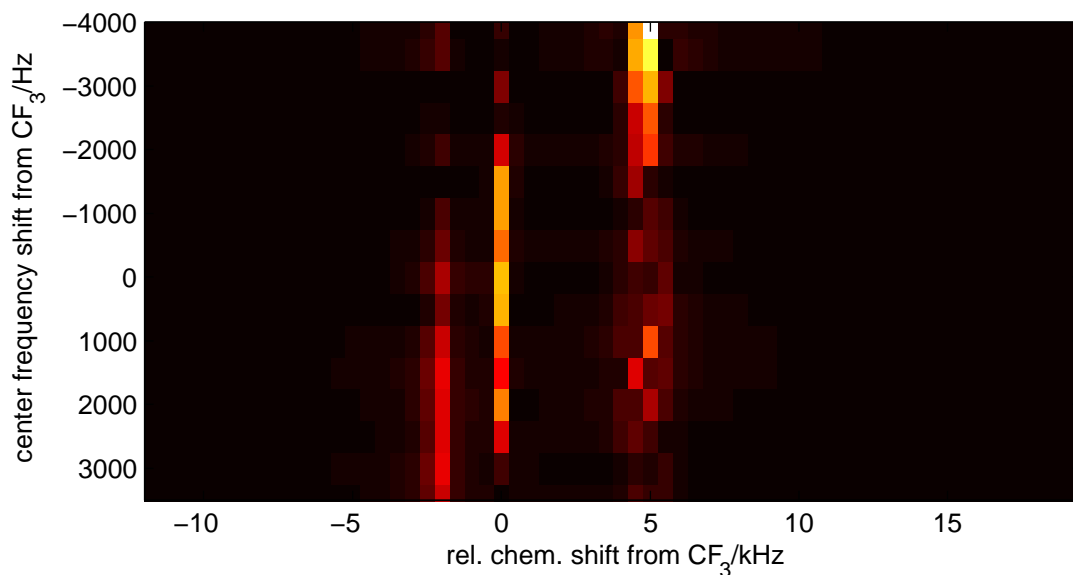
The spectral consistency of different specimen is shown in Figure 4.25. The spectral responses to the differently filled tubes differ between F-uTSI (bottom row) and LCSSFP (top row). The F-uTSI data in Figure 4.25c reveals ambiguous responses of the resonance lines of PFO. These differences are less pronounced in the LCSSFP acquisition, retaining the *spectral signature* of the agent. Additionally, F-uTSI develops visible artifacts around the PFO and a widened PSF.

4.6.4 Broadband response

The response of F-uTSI to PFOB with variable center frequencies is shown in Figure 4.26. Clearly, the response varies greatly and non-uniformly in reaction to a shifted center frequency. However, once the center frequency approaches a resonance complex the according



(a) LCSSFP



(b) F-uTSI

Figure 4.26: PFOB spectral response as a function of center frequencies, extracted from CSI data (center of a PFOB phantom).

For orientation, the PFOB-pulse collect experiment from Figure 4.1 is depicted on top.

Pulse parameters: $B_1 = 50\mu T$, $T_E = ES = 5ms$, $T_R = 1.5s$, $f_{c,init} = 11121Hz$

Sampling parameters: $f_S = 32kHz$, $N_S = 64$

Geometry: coronal projection 32×32 in $80 \times 80mm$

signal is amplified. The LCSSFP sequence shows a uniform spectral response, regardless of the chosen offset frequency (Figure 4.26a).

4.7 in-vivo experiments

In the following, the outcome of an *in-vivo* experiment is shown. The two sequence-candidates are executed, using the same total acquisition time.

4.7.1 Individual phase-incremented SSFP responses

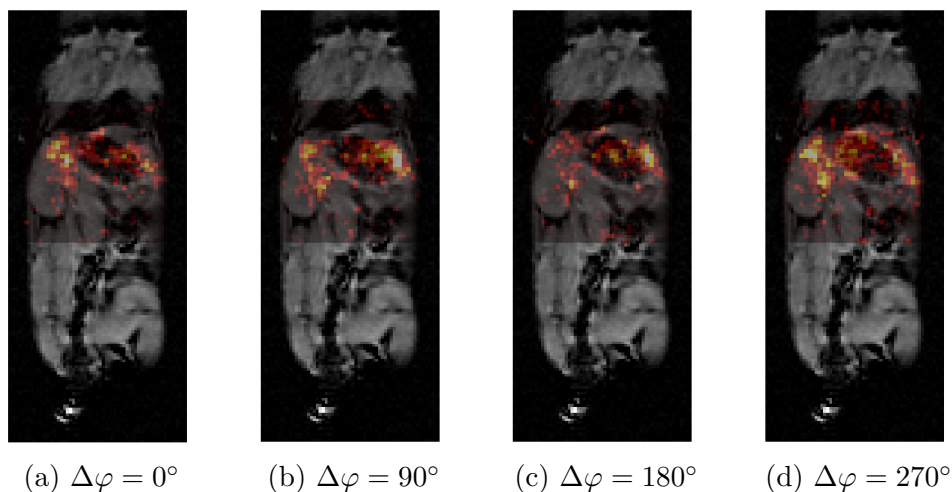


Figure 4.27: Single increment SSFP-CSI with high-NSA ($NSA = 20$) on a high-resolution coronal FFE-slice at the height of the stomach.

Pulse parameters: $B_1 = 50\mu T$, $T_R = 7.5ms$, $f_c = 10121Hz$

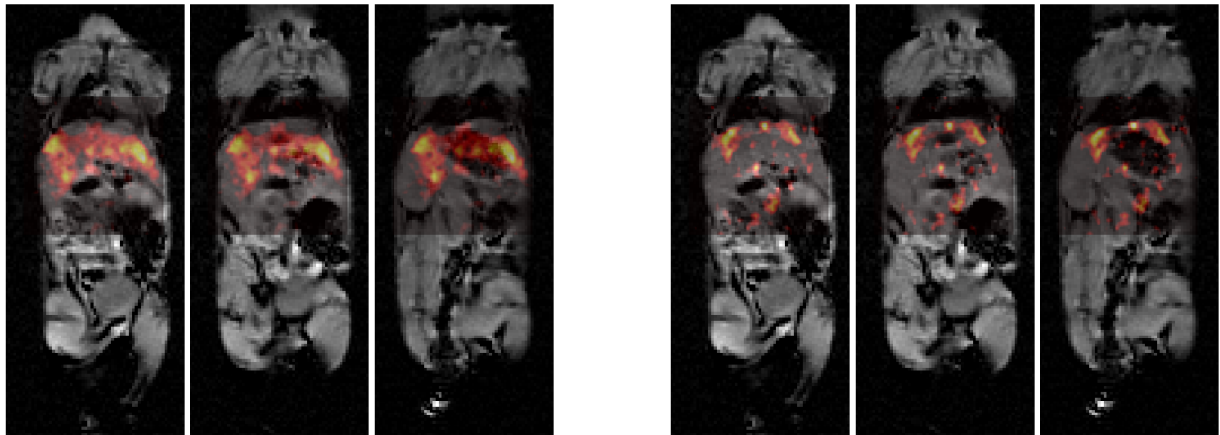
Sampling parameters: $f_S = 32kHz$, $N_S = 64$

Geometry: coronal projection 32×32 in $24 \times 24mm$, , *pseudo-radial* sampling

CSI-windowing: 60% dynamic range (*max - min*)

Figure 4.27 shows the results of the single phase incremented SSFPs. Clearly, over the integrated CSI sets, the spatial PFOB-distribution varies to a high degree: However, the coronal projections show a good confinement with the position of the liver. The upper 60% were chosen in order to yield as signal candidates as possible, excluding clear artifacts. To account for the expected averaging effect, the windowed dynamic range level will be increased in the combination of the four individual phase incremented SSFPs.

4.7.2 LCSSFP and F-uTSI responses



(a) LCSSFP

(b) F-uTSI

Figure 4.28: *in-vivo* comparison between LCSSFP and F-uTSI. Three FFE-slices each (left to right, anterior to posterior)

Pulse parameters: $B_1 = 50\mu T$, $T_{R,SSFP} = 7.5ms$, $T_E = 6ms$, $T_{R,F-uTSI} = 2000ms$, $NSA_{LCSSFP} = 20$, $NSA_{F-uTSI} = 6$, $f_c = 10121Hz$

Sampling parameters: $f_S = 32kHz$, $N_S = 64$

Geometry: coronal projection 32×32 in $24 \times 24mm$, , *pseudo-radial* sampling

CSI-windowing: LCSSFP: 80%, F-uTSI: 45% dynamic range

CSI-upsampling: $4x$ (bicubic interpolation)

Figure 4.28 presents the CSI-overlay of the combined LCSSFP and the F-uTSI-sequences. The LCSSFP in Figure 4.28a covers a large area of the kidney, outlined by the most anterior FFE-image, shown left in the triplet. The F-uTSI-response, on the other hand, shows PFOB-signal in the outer rims of the liver. Additionally signal is indicated in the lower part of the CSI overlay, near the *cecum*.

The displayed window was decreased to 45% in F-uTSI in order to blank out clearly spurious signal, e.g. signal outside the anatomy at the borders of the CSI-FOV. Signal appears attenuated in regions around the stomach, located horizontally central in the upper half of the CSI set.

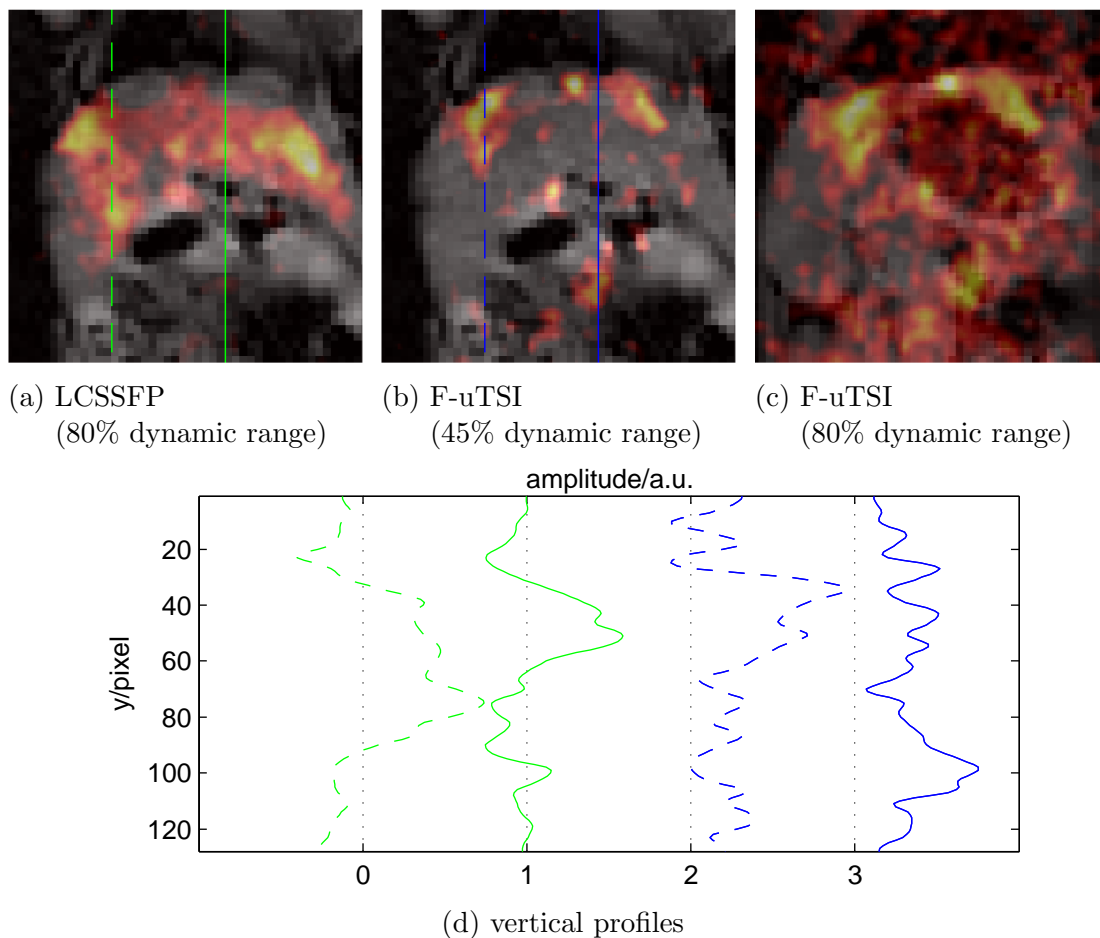


Figure 4.29: Magnified view of the acquisitions in Figure 4.28. Green (a: LCSSFP) and blue (c: F-uTSI).

The range between the rounded off and the rounded up integers represents the *displayed* dynamic range of the respective image and thus of the displayed profile.

CSI-windowing: LCSSFP: 80%, F-uTSI: 45% dynamic range

CSI-upsampling: $4x$ (bicubic interpolation)

The profiles in Figure 4.29 further investigate the additional signal in the F-uTSI acquisition. With the chosen restricted dynamic range, the F-uTSI yields a significant raise in regions outside the liver, but lacks signal in the anticipated regions (blue). The sparsity of the ^{19}F response using F-uTSI is again notable. In contrast to that, LCSSFP yields a more smooth signal, homogenously distributed inside the liver.

5 Discussion

Rapidly pulsed ^{19}F CSI needs to cover wide bandwidths. Typical ^{19}F substances, such as PFOB and PFO feature chemical shift dispersions in a range of 10kHz (Figure 4.1). In this regime, Spin Echo (SE) sequences are particularly dependent on the experimental setting. In clinically relevant settings, the B_1 amplitude is limited by Specific Absorption Rate (SAR) considerations as well as technical aspects. Therefore, the amplitudes of both excitation and refocussing pulses of Spin Echo sequences are small compared to the requirements set by the spectral widths of the ^{19}F species.

Investigations of k -space responses of multi-echo acquisitions revealed the background of previously observed imaging artifacts: The echo trains covering k -space trajectories exhibit significant modulations in the individual echo amplitudes. For the F-uTSI sequence, significant spatial differences were observed earlier, depending on the use and reconstruction of either *cartesian* or *pseudo-radial* sampling.

These image artifacts have been further investigated and found to be correlated with the modulated echo train, taking repeatedly applied imperfect pulsing with limited B_1 into account. Limited B_1 was shown to be the initial cause for the parameter dependency of the applied pulses resulting in the amplitude modulations in the echo train. In Section 4.2, already the first SE showed to be strongly compromised by selected combinations of *echo-time* and *offset frequency*. Consequently SE-CSI data presented in Sections 4.3.1 to 4.3.3 showed corresponding spurious images, again depending on the mentioned parameters. The measured variations along the CPMG echo-train was also shown by Hürlimann and Griffin [20] and is the primary cause for the artifacts in the F-uTSI acquisitions. This modulation is most prominent when the first echo is sampled with an echo time of $T_E = 6.42\text{ms}$ at $\Delta f = 2000\text{Hz}$ (Figure 4.6c): This condition of *minimal first echo* apparently yields the most pronounced variation in echo amplitude leading to the comparatively highest artifact levels.

It is shown that, depending on the pulse parameters, image artifacts comprise considerable amounts of signal energy. Figure 4.4c shows that the artifacts can obtain signal

amplitudes of nearly half of the actual signal. Simulations of the spectral pulse response along a CPMG pulse train using derived matrix approaches yielded highly variable frequency responses throughout the CPMG pulse train: the variability of the pulse responses in Section 4.3.4 suggests that these (simulated) variations are consistent with the measurements. Although the unsteady spectral magnetization components cause artifacts in the spatial domain, simulations and previous studies suggest that the multi-echo train still runs into a steady-state condition after several pulses.

Employing solely late echoes for imaging by skipping the initial, unstable responses, artifact levels could be reduced significantly (Section 4.3.5). Using *echo skipping*, observation of the echo-response in unencoded k -spaces proved to provide an additional indicator for the artifact level. It can be stated that the artifact level is suppressed to a fairly good amount using a higher number of *skipped echoes*, e.g. $N_{ES} = 8$. The data of Figure 4.8 clearly showed, that a *pseudo-dynamic steady state* is approached by employing *echo skipping*, already predicted by Hennig and Scheffler [28] for imaging.

However, it is also shown that *echo skipping* is by no means a general solution to the obviously strong variability of the F-uTSI sequence: Although suppressing artifact levels, depending on offset-frequency and echo time the spectral content can suffer from considerable damping of signal intensity.

Furthermore, regarding solely *spectral* quality, simulation results (4.3.4) indicated a strongly selective and variable spectral response in the F-uTSI, hampering predictions about the amplitude of resonances at certain offset-frequencies. Equally, field inhomogeneities are expected to strongly influence the spectral-spatial outcome of a certain resonance.

For multi-resonant agents such as PFOB, artifact levels vary also for the different resonances because of the individual offset-frequencies (Figure 4.11). Again, *echo-skipping* can avoid some of these artifacts.

When using F-uTSI with cartesian sampling, the signal loses most of its location information. It suffers from severe broadening predominantly in the direction of the k -sampling trajectory which is again caused by the echo-train modulations in k -space (Section 4.3.7). In comparison, for *pseudo-radial* sampling, these artifacts are distributed which has the beneficial effect of retained locality and a less apparent artifact level. In general, referring to the *Fourier slice theorem*, the radially acquired k -trajectories are *smear*ed over the image after retransformation in the direction of the k -trajectory. Similarly, the *pseudo-radially* sampled images yield a better localized signal, although tainted with symmetrically distributed artifacts. Furthermore, the *pseudo-radial* sampling pattern causes broadened PSFs when employing limited amounts of *Fourier slices*.

The results obtained with *echo skipping* and the evaluation of *cartesian* and *pseudo-radially* sampled images using F-uTSI triggered the exploitation of real steady-state sequences, i.e. SSFP schemes. Both simulated and measured results for the SSFP sequences show their inherent properties, offering a high stability over the sampling intervals. Figure 4.19 shows the ^{19}F in a well approached steady state, sampled in a *cartesian* manner. Signal amplitude modulations are simply not present in k -space - images are thus free of spatial artifacts, independent of the employed sampling pattern in k -space.

Furthermore, concluding Sections 4.4 and 4.5, depending on the phase increment of the used pulses, the spectral SSFP-responses exhibit their highly frequency selective *banding-pattern* known from MRI. Despite the dependence of the SSFP-response on relaxation properties, the signal evolution is stable and non-oscillating after reaching steady state. Consecutive pulse responses are consistent and, depending on the setting of the phase incrementing scheme, selective for different bands (Sections 4.5.3 and 4.5.4). By linear combination of the single SSFP responses, it was possible to obtain less frequency-selective characteristics. The method is thereby rendered less prone to both ambiguous spectral and spatial responses caused by small frequency changes, e.g. due to the lack of active shimming. Furthermore, the continuously outlined frequency response makes it possible to reproduce the *spectral signature* of PFCs (Section 4.5.5).

Comparisons drawn between F-uTSI and LCSSFP showed a clear advantage of the high averaging performance of the SSFP modus in comparison to the SE approach: the LCSSFP following an \sqrt{NSA} -proportional SNR_{max} , while F-uTSI did not clearly profit from averaging but even suffered from signal cancellation (Section 4.6.1).

A similar picture showed the evaluation of phantoms of small ^{19}F concentrations (Section 4.6.2), yielding similar performances of LCSSFP in high averaging scenarios independent of offset-frequency and interpulse delay. F-uTSI, on the other hand, is influenced by the changed parameters, responding highly variable to different pulse-delay/offset-frequency combinations. In averaging, the SSFP-inherent continuous pulsing and sampling proves its time efficiency, since SE sequences require sufficient relaxation after acquiring a number of echoes, while SSFP maintains continuous pulsing with T_R .

However, it has to be mentioned, that by using a comparatively (relative to the FOV) small phantom in the SNR-studies (Figures 4.23 and 4.24), signal intensities might be corrupted by partial volume effects: the maximal amplitude of the image as the numerator in SNR_{max} might be misestimated and promoted to faulty values SNR_{max} . Though, considering the steady performance of the LCSSFP the latter is unlikely.

Furthermore, as anticipated, LCSSFP-CSI was able to offer a widely uniform *spectral*

signature throughout frequency shifted acquisition or inhomogeneity-afflicted phantom acquisitions (Sections 4.6.3 and 4.6.4). F-uTSI acquisitions, on the other hand, suffered from the formerly described irregular f_c -dependency.

The *in-vivo* experiment confirms the spectral selectivity of the individual phase incremented SSFP acquisitions. The spatially variable ^{19}F -signal distribution among the differently phased SSFPs highlights the dependence on B_0 -inhomogeneity (Figure 4.27). Linearly combining the differently phased responses leads to the expected PFOB signal distribution, covering the outlined volume of the liver. F-uTSI acquisitions showed weaker correlations between the expected ^{19}F -signal and anatomy (Figure 4.28). For instance, ^{19}F signal is observed in the abdominal region outside the liver. However, regarding the application time of the PFOB emulsion 24h prior to the MRI-acquisition, PFOB is solely expected to be in the liver. Due to the comparatively higher noise level in F-uTSI acquisitions (Figure 4.29), signal candidates may potentially be left undetected. Equally spurious signals can be expected in areas without actual ^{19}F distribution due to the complex emergence of artifacts.

An inherent property of steady-state sequences is the rapid pulse repetition rate with low-flip angle pulses. Considering SAR as being approximately proportional to the squared flip-angle, F-uTSI is believed to deposit a higher average energy for a specific time frame compared to SSFP, while SSFP is able to acquire higher *NSA* in the same reference time frame. For obtaining optimal signal for the PFCs, however, the optimal combination of flip angle *and* T_R is yet to be determined by performing adequately precise T_1, T_2 -relaxometry on the substances under investigation. Especially regarding the limited available B_1 -field in the used clinical setup and its implications to echo-behaviour, these measurements are suggested to be carried out on NMR-spectrometers.

Concluding the theoretical thoughts, simulations, phantom and *in-vivo* acquisitions, the F-uTSI can be stated to be sufficiently characterized: the lacking determinability of the echo amplitude modulations implies spurious signals dependent on the parameters and thus corrupted spectral and spatial MRS images. It has to be mentioned that the performed measurements and the were also intended to resolve the spectral capability of the MRSI-sequences. Focussed on a specific resonance, F-uTSI shows proper CPMG behaviour. However, in multi-resonant substances this scenario is not generally achievable, making F-uTSI vulnerable to artefacts and irregular spectral selectivity. In comparison, evaluated SSFP sequences, particularly using combinations of different pulse phase schedules, proofed high stability and robustness in the complicated parameter field, both in spectral and spatial domain.

Bibliography

- [1] M. H. Levitt. *Spin dynamics: basics of nuclear magnetic resonance*. Wiley, 2008.
- [2] E. M. Haacke et al. *Magnetic resonance imaging: physical principles and sequence design*. Vol. 82. Wiley-Liss New York: 1999.
- [3] R. M. Gregory and A. D. Bain. “The effects of finite rectangular pulses in NMR: Phase and intensity distortions for a spin-1/2”. In: *Concept Magnetic Res. Part A* 34.6 (2009), pp. 305–314.
- [4] C. Bauer et al. “Gaussian pulses”. In: *J. Magn. Reson.* 58.3 (1984), pp. 442–457.
- [5] J. Pauly et al. “Parameter relations for the Shinnar-Le Roux selective excitation pulse design algorithm [NMR imaging]”. In: 10.1 (1991), pp. 53–65.
- [6] J. K. Sanders and B. K. Hunter. *Modern NMR spectroscopy: a guide for chemists*. Oxford University Press, New York, NY, 1988.
- [7] J. C. Gore and R. P. Kennan. “Physical and physiological basis of magnetic relaxation”. In: *Magn. Reson. Imaging* 1 (1999), pp. 33–42.
- [8] A. Bjørnerud and L. Johansson. “The utility of superparamagnetic contrast agents in MRI: theoretical consideration and applications in the cardiovascular system”. In: *NMR Biomed.* 17.7 (2004), pp. 465–477.
- [9] J. Ruiz-Cabello et al. “Fluorine (^{19}F) MRS and MRI in biomedicine”. In: *NMR Biomed.* 24.2 (2011), pp. 114–129.
- [10] H. Gunther and R. W. Gleason. *NMR Spectroscopy: An Introduction*. Wiley, 1980.
- [11] B. Fung. “Selective detection of multiplets via double quantum coherence: A ^{19}F NMR study of perfluorodecalin”. In: *Org. Magn. Resonance* 21.6 (1983), pp. 397–398.
- [12] E. L. Hahn. “Spin echoes”. In: *Phys. Rev.* 80.4 (1950), p. 580.

- [13] J. Hennig. “Echoes - how to generate, recognize, use or avoid them in MR-imaging sequences. Part I: Fundamental and not so fundamental properties of spin echoes”. In: *Concept Magnetic Res* 3.3 (1991), pp. 125–143.
- [14] K. Scheffler. “A pictorial description of steady-states in rapid magnetic resonance imaging”. In: *Concept Magnetic Res.* 11.5 (1999), pp. 291–304.
- [15] D. J. Drost, W. R. Riddle, and G. D. Clarke. “Proton magnetic resonance spectroscopy in the brain: report of AAPM MR Task Group# 9”. In: *Med. Phys.* 29 (2002), p. 2177.
- [16] S. Balac and L. Chupin. “Fast approximate solution of Bloch equation for simulation of RF artifacts in Magnetic Resonance Imaging”. In: *Math. Comput. Model* 48.11 (2008), pp. 1901–1913.
- [17] M. H. Levitt and R. Freeman. “Compensation for pulse imperfections in NMR spin-echo experiments”. In: *J. Magn. Reson.* 43.1 (1981), pp. 65–80.
- [18] B. A. Hargreaves et al. “Characterization and reduction of the transient response in steady-state MR imaging”. In: *Magn. Reson. Med.* 46.1 (2001), pp. 149–158.
- [19] A. D. Bain, C. Kumar Anand, and Z. Nie. “Exact solution of the CPMG pulse sequence with phase variation down the echo train: Application to R_2 measurements”. In: *J. Magn. Reson.* 209.2 (2011), pp. 183–194.
- [20] M. Hürlimann and D. Griffin. “Spin Dynamics of Carr–Purcell–Meiboom–Gill-like Sequences in Grossly Inhomogeneous B_0 and B_1 Fields and Application to NMR Well Logging”. In: *J. Magn. Reson.* 143.1 (2000), pp. 120–135.
- [21] M Yildirim et al. “Assessment of SNR and detection sensitivity of F-uTSI”. In: *Proc. Intl. Soc. Mag. Reson. Med.* 16. 2008.
- [22] T. Brown, B. Kincaid, and K Ugurbil. “NMR chemical shift imaging in three dimensions”. In: *P Natl. Acad. Sci. USA* 79.11 (1982), pp. 3523–3526.
- [23] A. Skoch, F. Jiru, and J. Bunke. “Spectroscopic imaging: basic principles”. In: *Eur. J. Radiol.* 67.2 (2008), pp. 230–239.
- [24] R Lamerichs et al. “In-vivo ultra-fast Spectroscopic Imaging of ^{19}F containing contrast agents”. In: *Proceedings of the 17th Annual Meeting of the ISMRM, Honolulu, Hawaii, USA.* 2009, p. 616.
- [25] R. S. Hinks and R. T. Constable. “Gradient moment nulling in fast spin echo”. In: *Magn. Reson. Med.* 32.6 (1994), pp. 698–706.
- [26] F. Casanova, J. Perlo, and B. Blümich. *Single-sided NMR*. Springer, 2011.

- [27] P. L. Roux and R. S. Hinks. “Stabilization of echo amplitudes in FSE sequences”. In: *Magn. Reson. Med.* 30.2 (1993), pp. 183–190.
- [28] J. Hennig and K. Scheffler. “Easy improvement of signal-to-noise in RARE-sequences with low refocusing flip angles”. In: *Magn. Reson. Med.* 44.6 (2000), pp. 983–985.
- [29] D. Mayer and D. Spielman. “Fast 1H Missing-Pulse SSFP Chemical Shift Imaging of the Human Brain at 7 Tesla”. In: *Proc. Intl. Soc. Mag. Reson. Med.* 15. 2007.
- [30] J. Hennig. “Echoes - how to generate, recognize, use or avoid them in MR-imaging sequences. Part II: Echoes in imaging sequences”. In: *Concept Magnetic Res.* 3.4 (1991), pp. 179–192.
- [31] S. S. Vasanaawala, J. M. Pauly, and D. G. Nishimura. “Linear combination steady-state free precession MRI”. In: *Magn. Reson. Med.* 43.1 (2000), pp. 82–90.
- [32] K. S. Nayak et al. “Wideband SSFP: alternating repetition time balanced steady state free precession with increased band spacing”. In: *Magn. Reson. Med.* 58.5 (2007), pp. 931–938.
- [33] N. K. Bangerter et al. “Analysis of multiple-acquisition SSFP”. In: *Magn. Reson. Med.* 51.5 (2004), pp. 1038–1047.
- [34] G. Weise et al. “In vivo imaging of stepwise vessel occlusion in cerebral photothrombosis of mice by ^{19}F MRI”. In: *PLoS one* 6.12 (2011), e28143.
- [35] P. Jakob et al. “Visualization of Abscess Formation in a Murine Thigh Infection Model of Staphylococcus aureus by ^{19}F -Magnetic Resonance Imaging (MRI)”. In: *PLoS ONE* 6 (2013).
- [36] J. G. Riess. “Oxygen Carriers (“Blood Substitutes”) sRaison d’Etre, Chemistry, and Some”. In: *Chem. Rev* 101 (2001), pp. 2797–2919.
- [37] W. Wolf et al. “Fluorine-19 NMR spectroscopic studies of the metabolism of 5-fluorouracil in the liver of patients undergoing chemotherapy”. In: *Magn. Reson. Imaging* 5.3 (1987), pp. 165–169.
- [38] R. P. Mason et al. “Perfluorocarbon imaging in vivo: A ^{19}F MRI study in tumor-bearing mice”. In: *Magn. Reson. Imaging* 7.5 (1989), pp. 475–485.
- [39] D. Freeman et al. “Rapid ^{19}F magnetic resonance imaging of perfluorooctyl bromide in vivo”. In: *Magn. Reson. Imaging* 6.1 (1988), pp. 61–64.
- [40] J. Brown et al. “Perfluorooctylbromide as a gastrointestinal contrast agent for MR imaging: use with and without glucagon.” In: *Radiology* 181.2 (1991), pp. 455–460.

-
- [41] M. Shimizu et al. “Tumor imaging with anti-CEA antibody labeled ^{19}F emulsion”. In: *Magn. Reson. Med.* 5.3 (1987), pp. 290–295.
- [42] S. D. Caruthers et al. “In vitro demonstration using ^{19}F magnetic resonance to augment molecular imaging with paramagnetic perfluorocarbon nanoparticles at 1.5 Tesla”. In: *Investigative radiology* 41.3 (2006), pp. 305–312.
- [43] J. H. Duyn and C. T. Moonen. “Fast proton spectroscopic imaging of human brain using multiple spin-echoes”. In: *Magn. Reson. Med.* 30.4 (1993), pp. 409–414.